Title

Exploring Oxidation State-Dependent Selectivity in Polymerization of Cyclic Esters and Carbonates with Zinc(II) Complexes

Authors

Abubekerov, Mark
Vlček, Vojtěch
Wei, Junnian
et al.

Publication Date

2018-09-01

DOI

10.1016/j.isci.2018.08.020

Peer reviewed

iScience

CellPress

Article

Exploring Oxidation State-Dependent Selectivity in Polymerization of Cyclic Esters and Carbonates with Zinc(II) Complexes

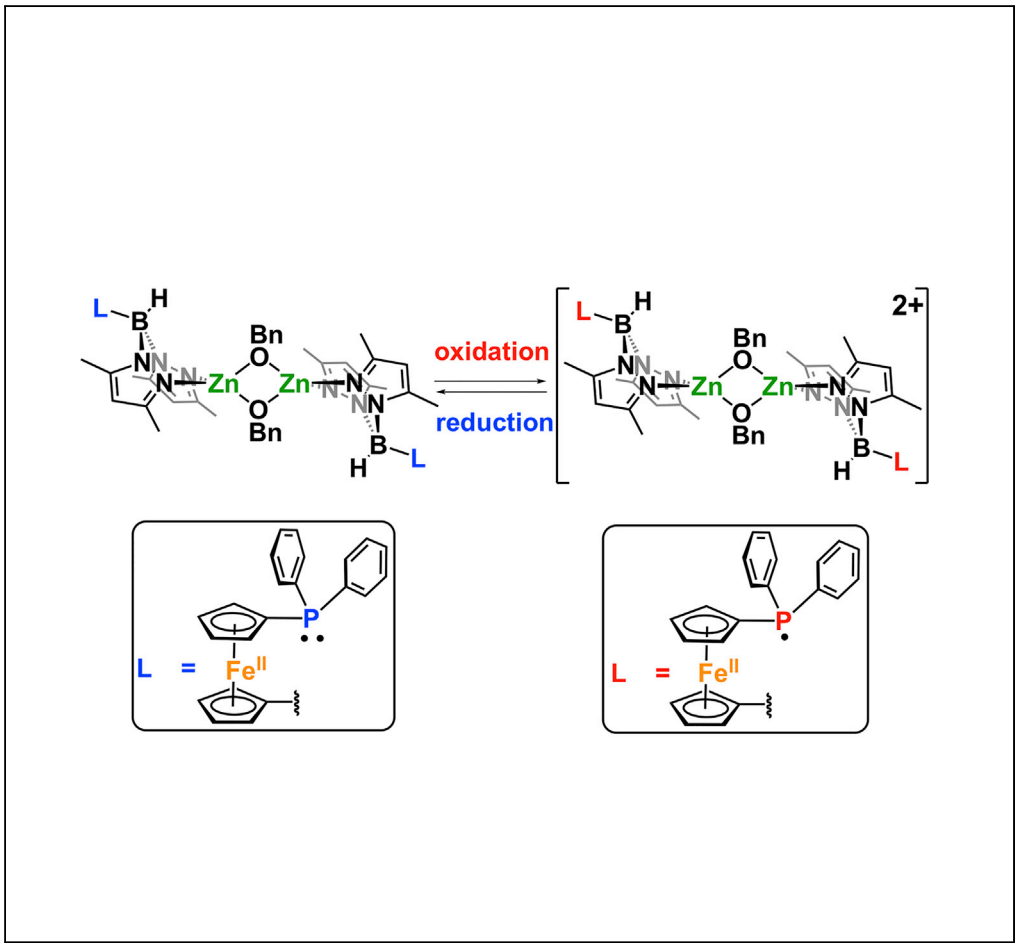

Mark Abubekerov, Vojtěch Vlček, Junnian Wei, ..., Karsten Meyer, Daniel Neuhauser, Paula L. Diaconescu

karsten.meyer@fau.de (K.M.)
dxn@chem.ucla.edu (D.N.)
pld@chem.ucla.edu (P.L.D.)

HIGHLIGHTS

Dimeric and monomeric zinc heteroscorpionate species were prepared

Monomeric zinc complex gives irreversible chemical redox and is inactive toward ROP

Dimeric zinc complex gives reversible chemical redox and is inactive toward ROP

Oxidation of the zinc benzoxide species occurs at the phosphine moiety

Abubekerov et al., iScience 7, 120–131
September 28, 2018
https://doi.org/10.1016/j.isci.2018.08.020

iScience

CellPress

Article

Exploring Oxidation State-Dependent Selectivity in Polymerization of Cyclic Esters and Carbonates with Zinc(II) Complexes

Mark Abubekerov,[1] Vojtěch Vlček,[1,3] Junnian Wei,[1,3,4] Matthias E. Miehlich,[2] Stephanie M. Quan,[1] Karsten Meyer,[2,*] Daniel Neuhauser,[1,*] and Paula L. Diaconescu[1,5,*]

SUMMARY

Neutral zinc alkoxide complexes show high activity toward the ring-opening polymerization of cyclic esters and carbonates, to generate biodegradable plastics applicable in several areas. Herein, we use a ferrocene-chelating heteroscorpionate complex in redox-switchable polymerization reactions, and we show that it is a moderately active catalyst for the ring-opening polymerization of L-lactide, ε-caprolactone, trimethylene carbonate, and δ-valerolactone. Uniquely for this type of catalyst, the oxidized complex has a similar polymerization activity as the corresponding reduced compound, but displays significantly different rates of reaction in the case of trimethylene carbonate and δ-valerolactone. Investigations of the oxidized compound suggest the presence of an organic radical rather than an Fe(III) complex. Electronic structure and density functional theory (DFT) calculations were performed to support the proposed electronic states of the catalytic complex and to help explain the observed reactivity differences. The catalyst was also compared with a monomeric phenoxide complex to show the influence of the phosphine-zinc interaction on catalytic properties.

INTRODUCTION

Aliphatic polyesters and polycarbonates derived from L-lactide (LA), ε-caprolactone (CL), δ-valerolactone (VL), and trimethylene carbonate (TMC) are biodegradable plastics with applications in the biomedical field and food packaging and with other specialty applications (Suriano et al., 2011; Ulery et al., 2011; Tian et al., 2012; Vert, 2005; Nair and Laurencin, 2007; Place et al., 2009; Ruzette and Leibler, 2005; Vroman and Tighzert, 2009; Oerlemans et al., 2010). Utilizing discrete metal complexes for the ring-opening polymerization of these cyclic monomers provides a great degree of control over the microstructure of the resulting polymers. In particular, neutral zinc alkoxide complexes show high activity toward the ring-opening polymerization of cyclic esters and carbonates. Due to the "living" nature of these processes, polymers with high molar mass and low dispersities are typically obtained (Guillaume and Carpentier, 2012; Ajellal et al., 2010; Helou et al., 2010; Helou et al., 2009; Williams et al., 2003; O'Keefe et al., 2001; Dechy-Cabaret et al., 2004; Wu et al., 2006; Platel et al., 2008; Wheaton et al., 2009; Arbaoui and Redshaw, 2010; Huang et al., 2013). In addition, utilizing zinc in polymerizations is advantageous due to the low cost, high abundance, and biocompatibility of the metal, allowing for wide application of the resulting biodegradable plastics.

The prevalent use of zinc in ring-opening polymerizations of cyclic esters and carbonates is matched by the use of hard N/O-based supporting ligands. However, only a few reports use soft donor ligands, such as phosphines, to stabilize the active zinc metal center (Fliedel et al., 2015; D'Auria et al., 2012; Liang et al., 2010). Such interactions can be beneficial due to the hemilabile nature of the zinc-phosphine bond and may result in highly active polymerization systems. The use of redox-active ligands in combination with zinc for ring-opening polymerizations is even less common than the use of soft donor ligands despite the potential benefits (Bakewell et al., 2015). Redox-active ligands provide a means of affecting the reactivity of the metal through changes in the oxidation state of the ligand. For example, in redox-switchable hemilabile ligands, the incorporation of a redox-active group into the ligand framework, in close proximity to a substitutionally labile component, allows to control the strength of the ligand-metal bond, leading to the dissociation of the ligand fragment upon oxidation (Singewald et al., 1995; Sassano and Mirkin, 1995; Higgins and Mirkin, 1995; Slone et al., 1997; Weinberger et al., 2001). In addition, the electronic and steric environment of the transition metal can be controlled without directly affecting its oxidation state (Allgeier and Mirkin, 1998).

[1]Department of Chemistry and Biochemistry, University of California, Los Angeles, CA 90095, USA

[2]Inorganic Chemistry, Department of Chemistry and Pharmacy, Friedrich-Alexander-University Erlangen–Nürnberg (FAU), Erlangen 91058, Germany

[3]These authors contributed equally

[4]Present Address: Department of Radiology & Biomedical Imaging, University of California, San Francisco, CA 94143, USA

[5]Lead Contact

*Correspondence: karsten.meyer@fau.de (K.M.), dxn@chem.ucla.edu (D.N.), pld@chem.ucla.edu (P.L.D.)

https://doi.org/10.1016/j.isci.2018.08.020

We previously reported the influence of a redox switch on the lability of [fc(PPh_2) (BH[(3,5-$Me)_2$pz]$_2$)] (($fc^{P,B}$), fc = 1,1′-ferrocenediyl, pz = pyrazole) in a palladium methyl complex in the presence of norbornene (Abubekerov et al., 2016). Upon the oxidation of the ferrocene backbone, the phosphine moiety displayed hemilabile behavior, resulting in norbornene polymerization. We reasoned that using the same ligand to support a more oxophilic metal, such as zinc(II), may yield a beneficial hemilabile interaction between the phosphine and the metal in the reduced state of the supporting ligand. In this case, the oxidation of the ligand could result in the loss of the zinc-phosphine interaction, similar to redox-switchable hemilabile ligands, and in altering the reactivity of a catalyst. Recently, we described the preparation as well as the characterization of [($fc^{P,B}$)Zn(μ-OCH_2Ph)]$_2$ (Abubekerov et al., 2018). However, in the case of the reduced species, a direct zinc-phosphine interaction was not observed. Despite this finding, and because of our interest in redox-switchable catalytic processes (Abubekerov et al., 2016, 2017; Wang et al., 2014, 2015; Quan and Diaconescu, 2015; Brosmer and Diaconescu, 2015; Abubekerov and Diaconescu, 2015; Upton et al., 2014; Broderick et al., 2011a, 2011b, 2011c; Quan et al., 2016, 2017; Lowe et al., 2017; Shepard and Diaconescu, 2016), we set out to investigate the influence of the redox state of $fc^{P,B}$ on the zinc-mediated ring-opening polymerization of cyclic esters and carbonates. In addition, an investigation into the redox and polymerization activity of a monomeric ferrocene-chelating heteroscorpionate zinc complex, ($fc^{P,B}$)Zn(OPh), is reported.

RESULTS AND DISCUSSION

Synthesis and Characterization of the Oxidized Zinc Benzoxide Complex

We previously described the preparation and investigation of the solution state behavior of [($fc^{P,B}$)Zn(μ-OCH_2Ph)]$_2$ (Abubekerov et al., 2018). Our studies revealed that this compound retains its dimeric state before and during the ring-opening polymerization of LA and TMC. In addition, we determined that the polymerizations proceeded via a living mechanism, yielding polymers with narrow dispersities and well-controlled molar masses. However, the influence of the redox state of the supporting ligand on the activity of this compound was not investigated.

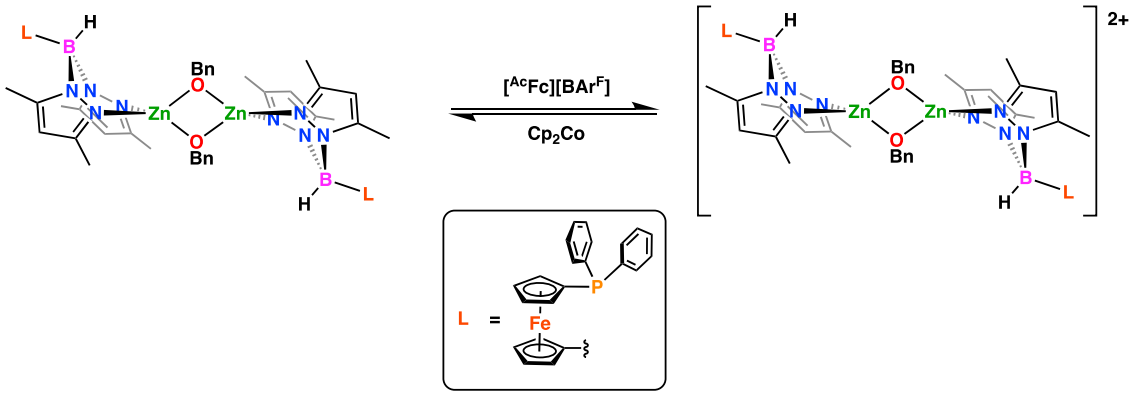

Electrochemical studies performed on [($fc^{P,B}$)Zn(μ-OCH_2Ph)]$_2$ show a reversible curve with a redox potential of −0.024 V versus Fc/Fc^+ (Figure S33), suggesting that ferrocenium salts may be used as chemical oxidants. On nuclear magnetic resonance (NMR) scale oxidation of the dimeric zinc complex with two equivalents of acetyl ferrocenium tetrakis(3,5-bis(trifluoromethyl)phenyl)borate ([^{Ac}Fc][BAr^F]) in C_6D_6 results in the formation of insoluble red solids and acetyl ferrocene, with only the latter being observed by NMR spectroscopy. Reduction with one equivalent of cobaltocene (Cp_2Co) restores the original complex, [($fc^{P,B}$)Zn(μ-OCH_2Ph)]$_2$, with no apparent decomposition or side products (Equation 1, Figures S1 and S2). On a larger scale, the addition of one equivalent of [^{Ac}Fc][BAr^F] to [($fc^{P,B}$)Zn(μ-OCH_2Ph)]$_2$ led to the isolation of red solids. Attempts to characterize the oxidation product by NMR spectroscopy were unsuccessful; the complex is insoluble in hydrocarbon solvents and rapidly reacts with non-hydrocarbon solvents (tetrahydrofuran [THF], chloroform). The reaction product of THF-d_8 with [($fc^{P,B}$)Zn(μ-OCH_2Ph)]$_2$[BAr^F]$_2$ is a paramagnetic complex, which is ^{31}P NMR silent, similar to the previously reported [($fc^{P,B}$)PdMe][BAr^F](Abubekerov et al., 2016). The ^{11}B NMR spectrum (Figure S4) shows a minor shift from δ = −7.2 to −7.8 ppm upon oxidation. The presence of the [BAr^F] counterion was confirmed by the presence of a singlet at δ = −5.9 and −63.5 ppm in the ^{11}B and ^{19}F NMR spectra (Figures S4 and S5), respectively. Attempts to grow

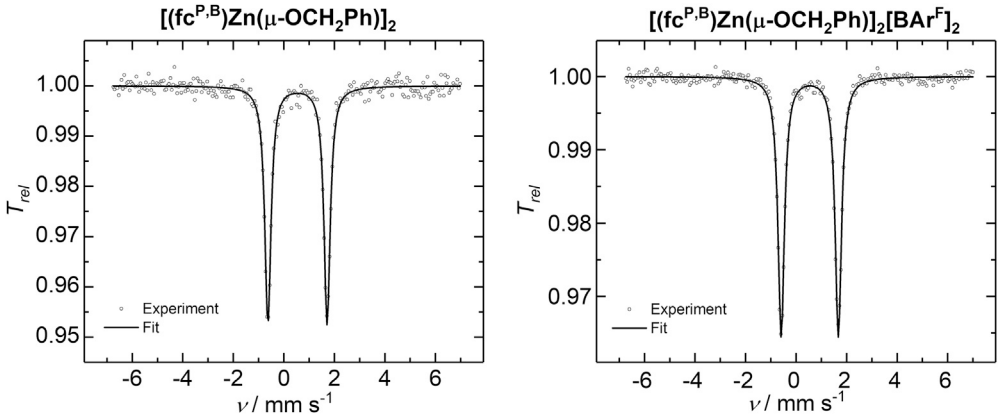

Figure 1. Zero-Field ^{57}Fe Mössbauer Spectra of [(fc^{P,B})Zn(μ-OCH$_2$Ph)]$_2$ and [(fc^{P,B})Zn(μ-OCH$_2$Ph)]$_2$[BAr^F]$_2$, Recorded as Solid Samples at 77 K

The solid lines are fits with Lorentzian doublets to the experimental spectra using the following isomer shifts δ and quadrupole splittings ΔE_Q: δ = 0.54(1) mm/s, ΔE_Q = 2.34 mm/s, Γ_{FWHM} = 0.29(1) mm/s (left) and δ = 0.54(1) mm/s, ΔE_Q = 2.26(1) mm/s, Γ_{FWHM} = 0.31(1) mm/s (right).

X-ray-quality crystals of the oxidized complex from various neat solvents and solvent combinations were unsuccessful, and only dark red oils were obtained. However, elemental analysis agrees with the formulation [(fc^{P,B})Zn(μ-OCH$_2$Ph)]$_2$[BAr^F]$_2$.

The lack of a signal in the ^{31}P NMR spectrum of the oxidized complex prompted further investigation into the electronic state of this compound. A determination of the solution-state magnetic susceptibility using the Evans method (Evans, 1959) of [(fc^{P,B})Zn(μ-OCH$_2$Ph)]$_2$[BAr^F]$_2$ was complicated by its lack of solubility in nonpolar solvents and its reactivity with polar solvents. The addition of 50–150 equivalents of monomer was necessary to solubilize the catalytically active species in deuterated benzene. In particular, we looked at the effective magnetic moment of *in situ*-generated [(fc^{P,B})Zn(μ-OCH$_2$Ph)]$_2$[BAr^F]$_2$ in the presence of monomers that could be ring-opened at ambient temperature, such as TMC, VL, and CL. Due to the rapid rate of TMC and VL polymerization, by the time the samples were prepared and taken to the NMR spectrometer (10 min) the polymerization of each monomer was already complete. In the case of TMC, the initial solution state effective magnetic moment was 1.90 μ_B per dimer, corresponding to a single unpaired electron. Within an hour, the paramagnetic sample decayed to a diamagnetic one (Figure S29). In the presence of VL, the effective initial magnetic moment was determined as 2.60 μ_B, consistent with two unpaired electrons per dimer, but slowly decreased to 1.34 μ_B after 2.5 hr (Figure S30). The reaction with CL is the slowest of the three monomers considered and shows the lowest degree of decay of the effective magnetic moment in solution: 3.06 μ_B after 10 minutes and 1.63 μ_B after 3.5 hr (Figure S31). These findings suggest that [(fc^{P,B})Zn(μ-OCH$_2$Ph)]$_2$[BAr^F]$_2$ is stable in solution only during the polymerization process and are consistent with the polymerization results described below. Attempts to acquire reproducible superconducting quantum interference device (SQUID) results were unsuccessful due to the sensitive nature of the compound.

Due to the difficulty of characterizing the oxidized complex in solution, we turned to ^{57}Fe Mössbauer spectroscopy on solid samples. At 77 K, with no applied magnetic field, [(fc^{P,B})Zn(μ-OCH$_2$Ph)]$_2$ shows a doublet with an isomer shift (δ = 0.54(1) mm/s) and quadrupole splitting (ΔE^Q = 2.34(1) mm/s) consistent with a low-spin iron(II) complex (Figure 1). Surprisingly, under the same conditions, [(fc^{P,B})Zn(μ-OCH$_2$Ph)]$_2$[BAr^F]$_2$ also displays a doublet with an isomer shift (δ = 0.54(1) mm/s) and quadrupole splitting (ΔE^Q = 2.26(1) mm/s) similar to [(fc^{P,B})Zn(μ-OCH$_2$Ph)]$_2$, and thus also consistent with a low-spin iron(II) complex (Figure 1). Attempts to acquire an X-band electron paramagnetic resonance (EPR) spectrum (in perpendicular mode), both in the solid and solution states, at liquid helium (7 K), liquid nitrogen (92 K), and ambient temperature (293 K), under a variety of different conditions, were unsuccessful. Similar Mössbauer and EPR spectroscopy results were reported for oxidized arylphosphinoferrocenes by Durfey et al. (Durfey et al., 2004) and were attributed to oxidation either of the phosphorus lone pair or of the aryl groups. The presence of an unpaired electron in close proximity of the phosphorus atom would be consistent with the lack of a signal in the ^{31}P NMR spectrum of the oxidized complex. Ligand-based oxidations of ferrocenes, as opposed to iron, were

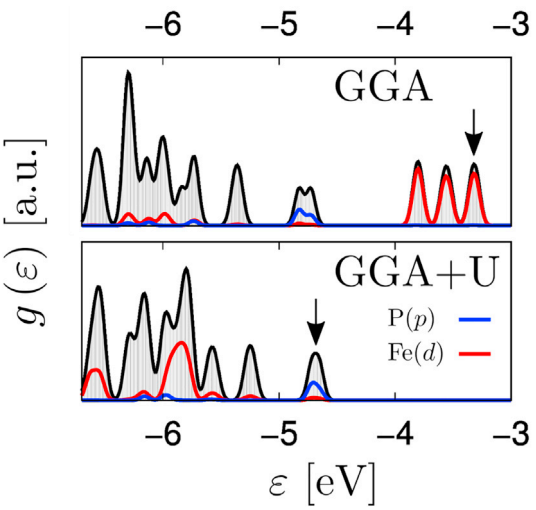

Figure 2. Total Density of States *g*(*e*) for the Top Valence Region

The highest occupied molecular orbital is indicated by a black arrow. Contributions of the atomic-like p and d orbitals of P and Fe are shown by different colors. Note that due to strong hybridization, multiple atomic orbitals contribute to each molecular state.

also reported for various phenylphosphinoferrocenes (Verschoor-Kirss et al., 2016) and ferrocenylpyrrole (Verschoor-Kirss et al., 2009) species; however, the inability to observe an EPR signal for these species remains puzzling. Isolated products of chemical oxidations displayed low-spin iron(II) species, as evidenced by ^{57}Fe Mössbauer spectroscopy in the case of a ferrocenylpyrrole complex, and a mix of low-spin iron(II) and low-spin iron(III) species in the case of phenylphosphinoferrocenes. However, the ^{31}P NMR spectra of the oxidized phenylphosphinoferrocenes typically display broadened, but detectible signals.

Electronic Structure Calculations

To probe further the electronic structure of $[(fc^{P,B})Zn(\mu\text{-}OCH_2Ph)]_2[BAr^F]_2$, we turned to computational studies by investigating the highest occupied valence states from which the electrons are removed for the model of $[(fc^{P,B})Zn(\mu\text{-}OCH_2Ph)]_2^{2+}$ (see section DFT Calculations, for model description). However, common local and semilocal density functionals cannot address this problem due to the improper description of the highly correlated *d* orbitals in Fe. The mean field description, i.e., the *common* exchange-correlation potential in density functional theory (DFT), fails to capture the physics of the localized states due to a self-interaction error (Perdew and Zunger, 1981; Kümmel and Kronik, 2008). This leads to a spurious delocalization of orbitals and an incorrect charge transfer and oxidation energies (Cohen et al., 2008; Kulik, 2015).

We first verified that (semi)local functionals indeed contradict the experimental data. We illustrate this by the density of electronic states obtained with the common generalized gradient approximation (GGA) functional (Perdew et al., 1996) (Figure 2). Projection of the corresponding wave functions onto the atomic orbitals reveals the character of individual states and their mutual hybridization. The top valence region (close to the HOMO at −3.3 eV) is dominated by the localized d orbitals of iron. An Fe d orbital contribution is also found in the lower energy molecular orbitals, but these do not participate energetically in the oxidation process. It is important to note that the phosphorus p orbitals are significantly separated in energy from the top valence region by as much as 0.9 eV. Hence, the GGA results suggest that the Fe atoms are oxidized, in contradiction to the experimental results.

This conundrum was resolved by mitigating the self-interaction error of the localized states. We resorted to the established approach of correcting the DFT picture by using a site- and orbital-specific potential U derived from the Hubbard model Hamiltonian (Himmetoglu et al., 2014). We estimated the potential for the Fe d states from first principles using linear response theory (Cococcioni and de Gironcoli, 2005) and obtained a U value of 7.7 eV. Such a high value leads to significant changes in the density of states (Figure 2). We observed that the Fe d states are pushed down in energy and significantly hybridize with the valence region below −5 eV. The frontier molecular orbitals are at −4.7 eV with a major contribution from phosphorus p states. Indeed, the highest occupied molecular orbital (HOMO) and HOMO-1 isosurfaces are found mostly around the phosphorus atoms (Figure 3).

The ground state geometry of the molecule is different when optimized for the cation or neutral species. This leads to a slight variation of the U parameter by 0.3 eV, but the character of the top valence state is not

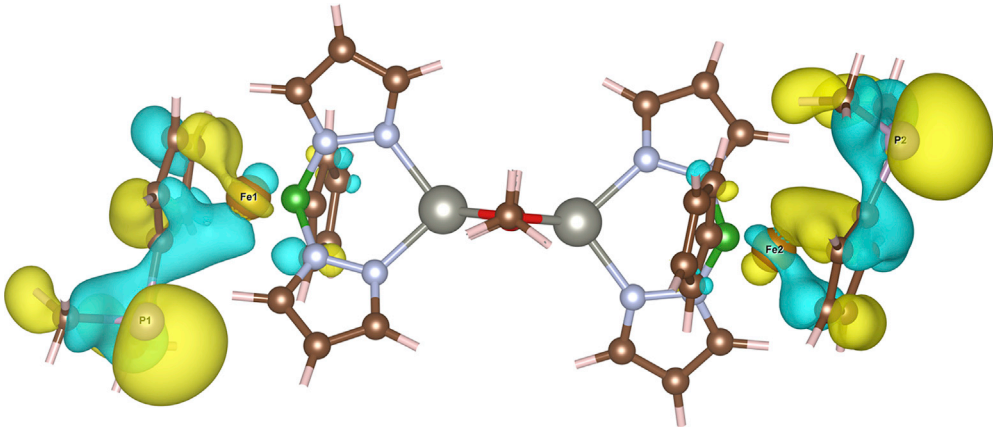

Figure 3. Isosurface for HOMO and HOMO-1 of $[(fc^{P,B})Zn(\mu\text{-}OCH_2Ph)]_2^{2+}$
Yellow and light blue coloring represents the positive and negative real parts of the wave function, respectively. For clarity, the hydrogen atoms were removed from the figure.

affected: for U > 4 eV (i.e., much smaller than the variation due to changes in the geometry), the top valence orbital becomes dominated by phosphorus p states. The GGA + U calculations thus show that Fe remains in its +II oxidation state and the phosphine groups are oxidized.

Polymerization of Cyclic Esters and Carbonates with the Zinc Benzoxide Species

The influence of the ligand oxidation state on the reactivity of the zinc benzoxide complex was examined through the ring-opening polymerization of cyclic esters and carbonates. Due to the difficulty in isolating and manipulating the oxidized complex, it was generated *in situ* just before use through the addition of two equivalents of $[^{Ac}Fc][BAr^F]$ to $[(fc^{P,B})Zn(\mu\text{-}OCH_2Ph)]_2$. The role of the oxidant as a potential polymerization catalyst was ruled out based on control experiments, which showed no activity under polymerization conditions for LA, TMC, and VL (Figures S14, S15, and S17) and only a minor conversion (<6%) for CL (Figure S16). In all cases, the polymerizations are well controlled with the molar masses of the resulting polymers increasing linearly with conversion, whereas the dispersity values remaining narrow (Tables S1–S6, Figures S47–S52).

Polymerizations of ca. 200 equivalents of LA showed a faster conversion for the reduced than the oxidized compound at various temperatures. At ambient temperature, a 60% conversion was obtained after 24 hr for the reduced species, whereas the oxidized complex reached only 17% conversion. Such a low conversion could be attributed to both the poor solubility of LA and, particularly, to the insolubility of the oxidized complex in benzene at ambient temperature. Performing the polymerizations at 70°C resulted in much shorter reaction times for both complexes (Table 1, entries 1 and 2); complete conversion was observed for the reduced complex and there was 91% conversion for the oxidized complex in 3 hr. The molar masses for the isolated polymers obtained from the oxidized and reduced complexes agree well with the corresponding theoretical molar masses. The dispersity values (*Đ*) are within the 1.00–1.15 range, suggesting that the polymerization process is well controlled.

Contrary to the LA case, the oxidation of the ligand had no observable influence on the rates of polymerization of CL (Table 1, entries 3 and 4). Polymerizations of ca. 200 equivalents of CL at ambient temperature reached completion for both the oxidized and the reduced species in 24 hr. On the other hand, carrying out the polymerizations at 70°C resulted in complete consumption of the monomer within 30 min for both compounds. Similar to LA, the molar masses of the polymers, obtained by size exclusion chromatography (SEC), from both the oxidized and reduced species agree well with the theoretical values. However, the dispersity values (*Đ*) are slightly narrower and fall between 1.0 and 1.1.

The most pronounced difference between the oxidized and the reduced compounds was observed for the polymerization of TMC (Table 1, entries 5 and 6) and VL (Table 1, entries 7 and 8). The complete conversion of ca. 200 equivalents of TMC was accomplished in under 15 min at ambient temperature utilizing the oxidized species and in up to 90 min for the reduced complex. Similarly, the conversion of ca. 200 equivalents of VL plateaus at 92% for the oxidized species after 20 min at ambient temperature, whereas the

Entry	Compound	Monomer	Time (min)	Conversion (%)	M_n (NMR)	M_n (SEC)	$Đ$
1	Reduced	LA	180	>99	1.40	1.38	1.14
2	Oxidized	LA	180	91	1.32	1.35	1.02
3	Reduced	CL	30	>99	0.90	0.89	1.09
4	Oxidized	CL	30	>99	1.07	1.06	1.08
5	Reduced	TMC	90	98	1.00	1.00	1.14
6	Oxidized	TMC	15	>99	0.79	0.81	1.02
7	Reduced	VL	60	92	1.02	1.04	1.01
8	Oxidized	VL	20	92	1.01	1.05	1.04

Table 1. Polymerization of Cyclic Esters and Carbonates by [($fc^{P,B}$)Zn(μ-OCH_2Ph)]$_2$ ("Reduced") and the *In Situ*-Generated [($fc^{P,B}$)Zn(μ-OCH_2Ph)]$_2$[BAr^F]$_2$ ("Oxidized")

Conditions: monomer (0.50 mmol), catalyst (0.0025 mmol), oxidant (0.005 mmol), d_6-benzene as a solvent (0.5 mL), and hexamethylbenzene (0.025 mmol) as an internal standard. Entries 1–4 were carried out at 70°C and entries 5–8 were performed at ambient temperature; M_n are reported in 10^4 g/mol; $Đ = M_w/M_n$.

same conversion is obtained for the reduced compound after 60 min. Further conversion of VL cannot be obtained with an increased time or elevated temperatures. All polymers show excellent agreement between NMR spectroscopy and SEC molar masses and display narrow dispersity values.

Literature examples of LA and CL polymerization by zinc complexes are rather common (Chisholm et al., 2000; Honrado et al., 2016; Lian et al., 2007; Alonso-Moreno et al., 2008; Schofield et al., 2009; Mou et al., 2014; Garcés et al., 2010), whereas examples of TMC and VL polymerizations are not as prevalent (Vivas et al., 2003; Gowda and Chakraborty, 2010; Helou et al., 2008). Compared with other heteroscorpionate complexes, tris(pyrazolyl)borate complexes, and ligands with similar tripodal frameworks, both the oxidized and the reduced metal complexes display moderate activity for the polymerization of LA and CL (Chisholm et al., 2000; Honrado et al., 2016; Lian et al., 2007; Alonso-Moreno et al., 2008; Schofield et al., 2009; Mou et al., 2014; Garcés et al., 2010). Similarly, the reduced species shows a moderate activity toward the polymerization of TMC and VL, whereas the oxidized compound shows high activity toward the same monomers (Vivas et al., 2003; Gowda and Chakraborty, 2010; Helou et al., 2008).

Synthesis and Characterization of a Zinc Phenoxide Complex

To investigate the possibility of redox-switchable hemilabile ligand behavior we also prepared a monomeric zinc species containing a phosphorus-zinc interaction. The addition of NaOPh to ($fc^{P,B}$)ZnCl in methylene chloride resulted in the isolation of ($fc^{P,B}$)Zn(OPh) as orange crystals in 79.8% yield (Equation 2). The solid-state molecular structure of ($fc^{P,B}$)Zn(OPh) (Figure 4) in crystals of ($fc^{P,B}$)Zn(OPh)•(Et_2O) was determined using single-crystal X-ray diffraction. The coordination environment around the zinc center has a distorted tetrahedral geometry with a τ value of 0.88 (Yang et al., 2007). Unlike in the case of [($fc^{P,B}$)Zn(μ-OCH_2Ph)]$_2$, the phenoxide ligands do not bridge, resulting in a monomeric species. However, attempts to prepare additional monomeric zinc species containing bulky aryloxide or amide groups (e.g., 2,4-di-*tert*-butylphenoxide, 2,6-dimethylphenoxide, N,N-bis(trimethylsilyl)amide) were not successful.

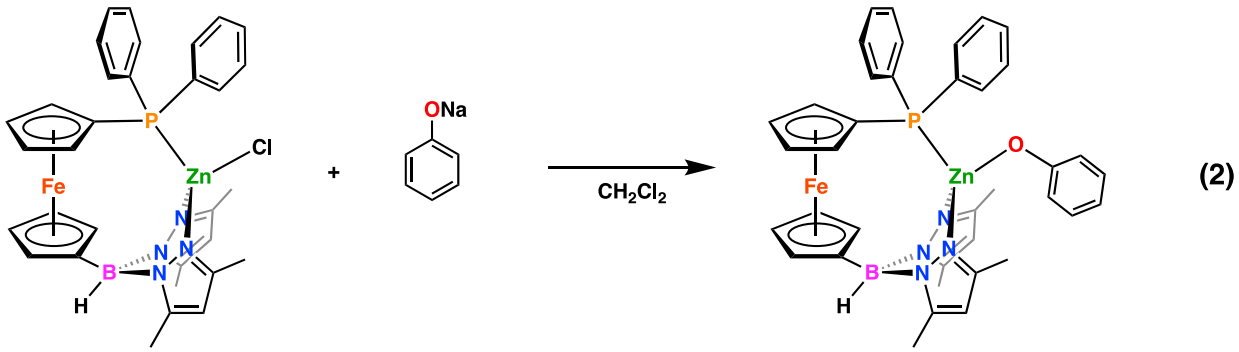

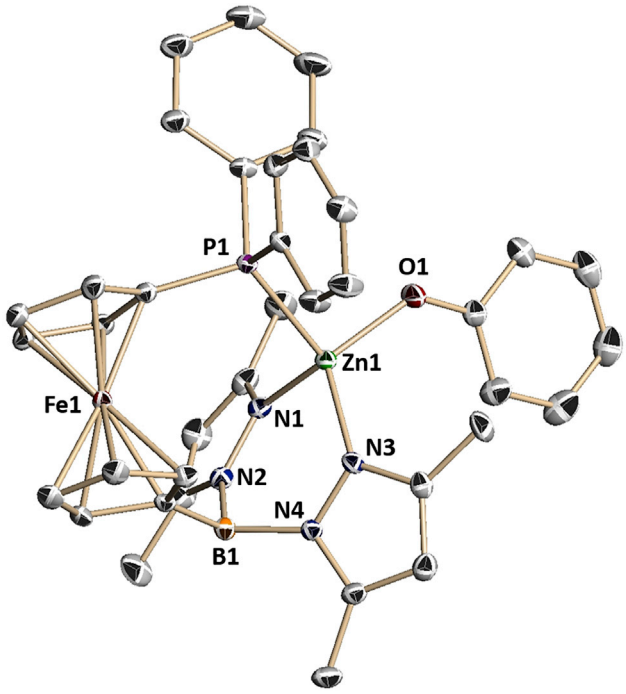

Figure 4. Molecular Structure Drawing of ($fc^{P,B}$)Zn(OPh) from Crystals of ($fc^{P,B}$)Zn(OPh)•(Et_2O) with Thermal Ellipsoids at 50% Probability; Hydrogen Atoms Are Omitted for Clarity

Selected distances (Å) and angles (°): O(1)-Zn(1), 1.9095(15); N(1)-Zn(1), 2.0063(17); N(3)-Zn(1), 1.9921(17); P(1)-Zn(1), 2.3984(5); N(1)-Zn(1)-N(3), 95.55(7); N(1)-Zn(1)-O(1), 115.55(7); N(3)-Zn(1)-O(1), 118.59(7); O(1)-Zn(1)-P(1), 99.79(5); N(1)-Zn(1)-P(1), 120.60(5), P(1)-Zn(1)-N(3), 107.81(5). See also Figure S38.

Electrochemically, ($fc^{P,B}$)Zn(OPh) shows a reversible redox event with a half-potential of −0.065 V versus Fc/Fc^+ (Figure S36). On an NMR scale, the oxidation of ($fc^{P,B}$)Zn(OPh) with 1.1 equivalents of [^{Ac}Fc][BAr^F] in C_6D_6 results in the formation of insoluble red solids, just like in the case of [($fc^{P,B}$)Zn(μ-OCH_2Ph)]$_2$. However, the complete oxidation of the starting material does not occur, and a mixture of ($fc^{P,B}$)Zn(OPh) and ^{Ac}Fc is observed spectroscopically (Figure S22). Similarly, utilizing excess $AgBF_4$ did not result in the complete oxidation of ($fc^{P,B}$)Zn(OPh), which could still be observed as broad peaks in the ^{1}H NMR spectrum due to the presence of solid silver in the sample (Figure S23).

Polymerization of Cyclic Esters and Carbonates with the Zinc Phenoxide Species

Despite the lack of a robust redox-switchable behavior, we looked into the polymerization activity of ($fc^{P,B}$)Zn(OPh). Although ($fc^{P,B}$)Zn(OPh) is a monomeric complex, its propensity to form a dimeric species during the polymerization of cyclic esters and carbonates must be considered. Since [($fc^{P,B}$)Zn(μ-OCH_2Ph)]$_2$ remains a dimeric species during the ring-opening polymerization of cyclic esters and carbonates, it is worth considering that ($fc^{P,B}$)Zn(OPh) might dimerize after a single reaction with a monomer. To test this theory, the polymerization of ca. 10 equivalents of LA in the presence of ($fc^{P,B}$)Zn(OPh) was monitored by NMR spectroscopy (Figure S24). The rate of polymerization is substantially slower compared with that of [($fc^{P,B}$)Zn(μ-OCH_2Ph)]$_2$, reaching only a 65% conversion of the 10 equivalents after 5 hr at 100°C (Figure S25). However, after the reaction onset, the signals corresponding to ($fc^{P,B}$)Zn(OPh) do not shift in the ^{1}H NMR spectra (Figure S24); this finding prompted a further look into the polymerization process by diffusion ordered spectroscopy. We previously used this technique to illustrate that our zinc polymerization systems show the same diffusion rate for the catalyst and the polymer (Abubekerov et al., 2018). However, in the present case, the diffusion rate of polylactide (PLA) was substantially different from that of ($fc^{P,B}$)Zn(OPh), suggesting that ($fc^{P,B}$)Zn(OPh) does not participate in the polymerization process (Figure S26). Similar results were obtained in the case of TMC. Polytrimethylenecarbonate (PTMC) was formed at a slow rate, but no change was observed for ($fc^{P,B}$)Zn(OPh) (Figures S27 and S28), suggesting that an impurity or a decomposition product might be responsible for monomer conversion.

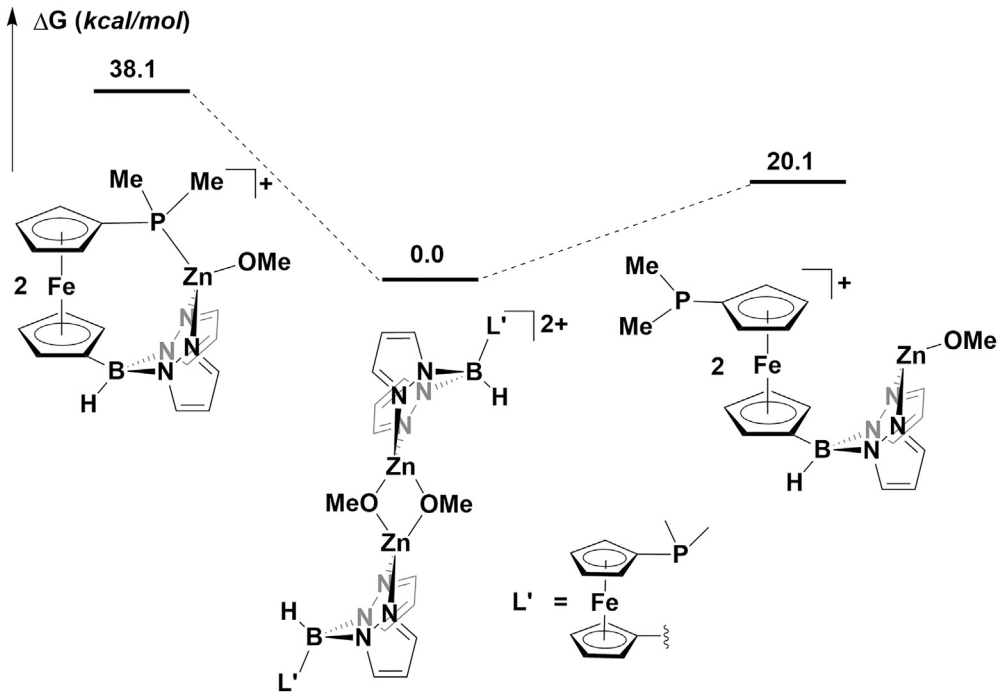

Figure 5. Optimized Structures for Models of $[(fc^{P,B})Zn(\mu\text{-}OCH_2Ph)]_2[BAr^F]_2$

DFT Calculations

To gain a better understanding of the influence of ligand oxidation on the activity of the catalyst, we turned to DFT. All calculations were carried out with the Gaussian09 program package (Frisch, 2010 [see Supplemental Information for the full reference]) on the Extreme Science and Engineering Discovery Environment (Towns et al., 2014). The methyl groups of the pyrazole substituents were replaced by hydrogen atoms and the phenyl groups of PPh_2 were replaced by methyl groups to simplify the calculations (for more details about calculations, see Supplemental Information). Lactide was chosen as the model substrate for the DFT calculations. Although DFT calculations did not describe correctly the electronic structure of $[(fc^{P,B})Zn(\mu\text{-}OCH_2Ph)]_2^{2+}$, the results reported below are still meaningful.

We previously reported a computational study comparing the energies of possible monomeric and dimeric structures of the zinc benzoxide complexes and showed that the dimer $[(fc^{P,B})Zn(\mu\text{-}OCH_2Ph)]_2$ was more stable (by 3.3 kcal/mol) than the corresponding monomer $(fc^{P,B})Zn(OCH_2Ph)$ (Abubekerov et al., 2018). Calculations conducted at the same level of theory showed that, in the oxidized state, the dimeric species $[(fc^{P,B})Zn(\mu\text{-}OCH_2Ph)]_2^{2+}$ was also greatly favored (20.1 kcal/mol) over the corresponding monomer (Figure 5). This preference was maintained even after the insertion of the first lactide, with the dimeric intermediate being 12.7 kcal/mol lower in energy than the monomeric intermediate (Figure 6). These results suggest that the active species in the reactions involving the oxidized complex is a dimer, similarly to what was previously found for the reduced compound (Abubekerov et al., 2018).

A look at the energy surfaces of the reduced (Abubekerov et al., 2018) and the oxidized complexes during TMC polymerization showed a small difference between the two reactions (Figures S53 and 7, respectively). The highest activation barrier for both reactions corresponds to the ring-opening step ($TS_{II\text{-}III}$), with the activation barrier for the reduced complex being lower by 5.3 kcal/mol. Such a small difference between the two compounds is in agreement with the minor rate differences observed for the ring-opening polymerizations catalyzed by the reduced and oxidized species. These results also agree with the electronic structure calculations described above: since the oxidation of the supporting ligand is centered on the phosphine ligand, it has little impact on the rate of ring-opening polymerization due to the lack of a phosphine-zinc interaction in both the reduced and oxidized states.

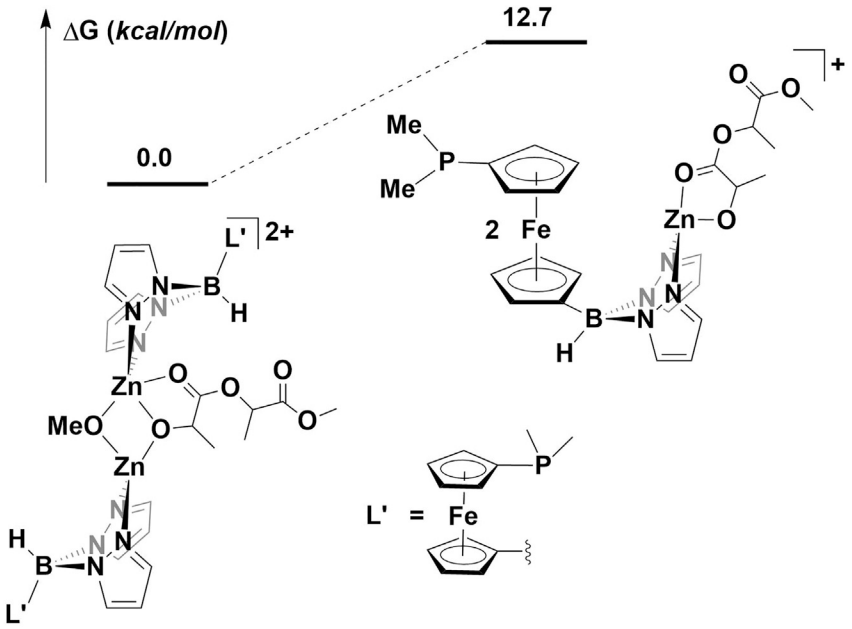

Figure 6. Optimized Structures of the Product Obtained after the First Lactide Ring-Opening Event Indicating that the Dimeric Species Is More Energetically Favored than the Monomeric Species

Conclusions

The zinc complexes supported by a ferrocene-chelating heteroscorpionate ligand showed reversible electron transfer events during cyclic voltammetry experiments. Consequently, their applicability toward redox-switchable catalysis in the ring-opening polymerization of cyclic esters and TMC was investigated. However, $[(fc^{P,B})Zn(\mu\text{-}OCH_2Ph)]_2[BAr^F]_2$ proved difficult to characterize due to its poor solubility and thermally sensitive nature. A combination of NMR and Mössbauer spectroscopies supported the existence of a paramagnetic species, but with the ferrocene iron remaining in a +2 oxidation state. A careful analysis of the electronic structure of the oxidized complex via a computational study concluded that the electron is removed from the phosphorus atom and not iron, as was originally expected.

Different polymerization rates for $[(fc^{P,B})Zn(\mu\text{-}OCH_2Ph)]_2$ and the corresponding oxidized complex, $[(fc^{P,B})Zn(\mu\text{-}OCH_2Ph)]_2[BAr^F]_2$, toward the same set of monomers were observed. The differences in the observed reactivity are attributed to the difference in charge distributions between the neutral and the cationic zinc species. More importantly, unlike in other redox-switchable systems reported by us, both oxidation states of the same pre-catalyst reacted with all the substrates investigated. This lack of selectivity is attributed to the absence of a zinc-phosphine interaction in both the reduced and oxidized states of the zinc benzoxide species and was probed via DFT calculations. However, the monomeric zinc phenoxide species, $(fc^{P,B})Zn(OPh)$, which retains the phosphine-zinc interaction in solution, was found inactive toward the ring-opening polymerization of LA and TMC. Based on the results of this investigation, we are currently developing a monomeric zinc alkoxide species bearing a ferrocene-chelating heteroscorpionate derivative, and are interested in studying its application toward the ring-opening polymerization of cyclic esters and carbonates.

METHODS

All methods can be found in the accompanying Transparent Methods supplemental file.

DATA AND SOFTWARE AVAILABILITY

The cif was deposited with CCDC, #1838242. The optimized coordinates are available as an excel spreadsheet (Data S1) and an xyz file (Data S2) as Supplemental Information.

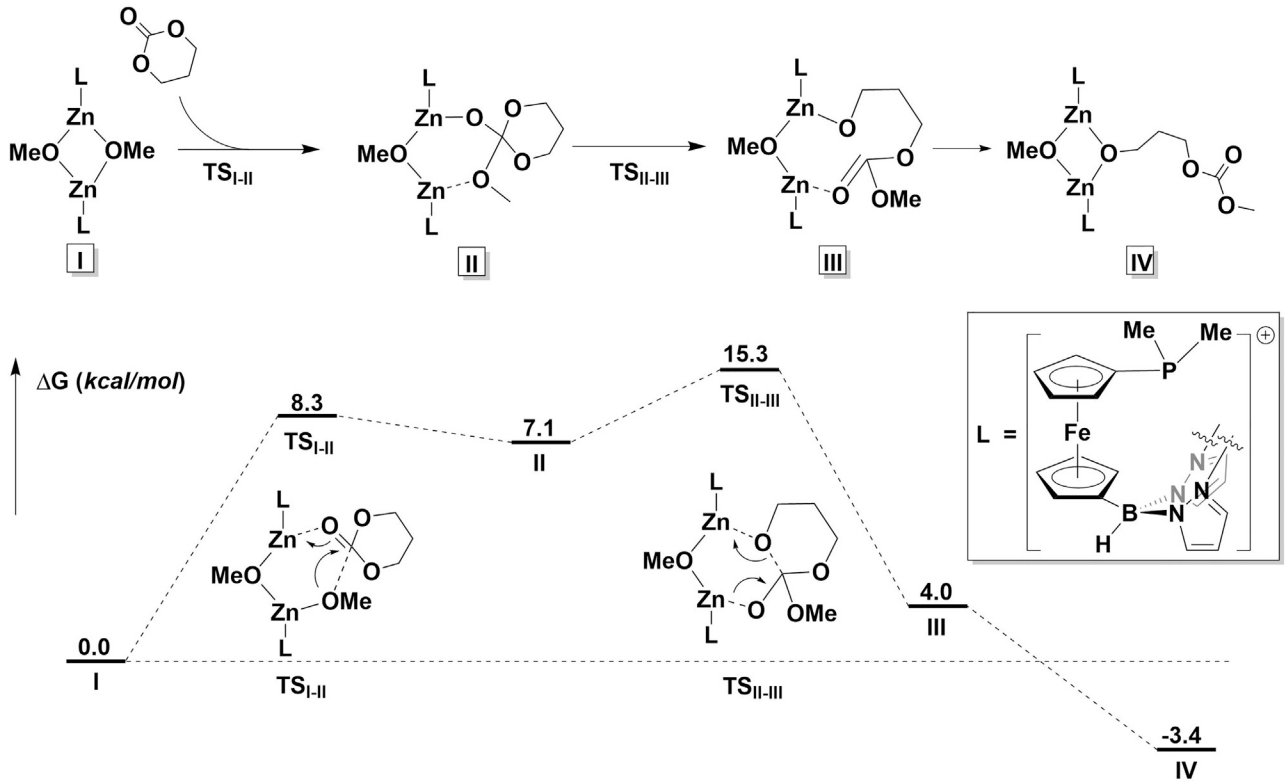

Figure 7. Energy Profile for the Ring-Opening Polymerization of TMC Catalyzed by the Oxidized Form of the Zinc Complex
See also Figure S53.

SUPPLEMENTAL INFORMATION

Supplemental Information includes Transparent Methods, 53 figures, 7 tables, and 2 data files and can be found with this article online at https://doi.org/10.1016/j.isci.2018.08.020.

ACKNOWLEDGMENTS

This work was supported by NSF, Grant 1362999 to P.L.D. and CHE-1048804 for NMR spectroscopy. D.N. acknowledges support by the NSF grant DMR/BSF-1611382. M.E.M. and K.M. acknowledge generous support from the Friedrich-Alexander-University Erlangen-Nürnberg (FAU). Part of the calculations were supported by the Extreme Science and Engineering Discovery Environment (XSEDE), which is supported by National Science Foundation grant number ACI-1053575, as the computational project TG-CHE160092. We thank Dr. Jonathan Brosmer for assistance with the elemental analysis experiments.

AUTHOR CONTRIBUTIONS

M.A. designed and conducted the synthetic and polymerization experiments and wrote the paper, V.V. performed the electronic structure calculations, J.W. performed the DFT calculations, M.E.M. performed the Mössbauer experiments, S.M.Q. performed the polymer characterization, K.M. designed the Mössbauer experiments, D.N. designed the electronic structure calculations, and P.L.D. designed the synthetic and polymerization experiments and wrote the paper.

DECLARATION OF INTERESTS

The authors declare no competing interests.

Received: April 18, 2018
Revised: June 21, 2018
Accepted: August 21, 2018
Published: September 28, 2018

REFERENCES

Abubekerov, M., and Diaconescu, P.L. (2015). Synthesis and characterization of ferrocene-chelating heteroscorpionate complexes of nickel(II) and zinc(II). Inorg. Chem. *54*, 1778–1784.

Abubekerov, M., Khan, S.I., and Diaconescu, P.L. (2017). Ferrocene-bis(phosphinimine) nickel(II) and palladium(II) alkyl complexes: influence of the Fe–M (M = Ni and Pd) interaction on redox activity and olefin coordination. Organometallics *36*, 4394–4402.

Abubekerov, M., Shepard, S.M., and Diaconescu, P.L. (2016). Switchable polymerization of norbornene derivatives by a ferrocene-palladium(II) heteroscorpionate complex. Eur. J. Inorg. Chem. *2016*, 2634–2640.

Abubekerov, M., Wei, J., Swartz, K.R., Xie, Z., Pei, Q., and Diaconescu, P.L. (2018). Preparation of multiblock copolymers via step-wise addition of l-lactide and trimethylene carbonate. Chem. Sci. *9*, 2168–2178.

Ajellal, N., Carpentier, J.-F., Guillaume, C., Guillaume, S.M., Helou, M., Poirier, V., Sarazin, Y., and Trifonov, A. (2010). Metal-catalyzed immortal ring-opening polymerization of lactones, lactides and cyclic carbonates. Dalton Trans. *39*, 8363–8376.

Allgeier, A.M., and Mirkin, C.A. (1998). Ligand design for electrochemically controlling stoichiometric and catalytic reactivity of transition metals. Angew. Chem. Int. Ed. *37*, 894–908.

Alonso-Moreno, C., Garcés, A., Sánchez-Barba, L.F., Fajardo, M., Fernández-Baeza, J., Otero, A., Lara-Sánchez, A., Antiñolo, A., Broomfield, L., López-Solera, M.I., and Rodríguez, A.M. (2008). Discrete heteroscorpionate lithium and zinc alkyl complexes. synthesis, structural studies, and ROP of cyclic esters. Organometallics *27*, 1310–1321.

Arbaoui, A., and Redshaw, C. (2010). Metal catalysts for ε-caprolactone polymerisation. Polym. Chem. *1*, 801–826.

Bakewell, C., Fateh-Iravani, G., Beh, D.W., Myers, D., Tabthong, S., Hormnirun, P., White, A.J.P., Long, N., and Williams, C.K. (2015). Comparing a series of 8-quinolinolato complexes of aluminium, titanium and zinc as initiators for the ring-opening polymerization of rac-lactide. Dalton Trans. *44*, 12326–12337.

Broderick, E.M., Guo, N., Vogel, C.S., Xu, C., Sutter, J., Miller, J.T., Meyer, K., Mehrkhodavandi, P., and Diaconescu, P.L. (2011a). Redox control of a ring-opening polymerization catalyst. J. Am. Chem. Soc. *133*, 9278–9281.

Broderick, E.M., Guo, N., Wu, T., Vogel, C.S., Xu, C., Sutter, J., Miller, J.T., Meyer, K., Cantat, T., and Diaconescu, P.L. (2011b). Redox control of a polymerization catalyst by changing the oxidation state of the metal center. Chem. Commun. *47*, 9897–9899.

Broderick, E.M., Thuy-Boun, P.S., Guo, N., Vogel, C.S., Sutter, J., Miller, J.T., Meyer, K., and Diaconescu, P.L. (2011c). Synthesis and characterization of cerium and yttrium alkoxide complexes supported by ferrocene-based chelating ligands. Inorg. Chem. *50*, 2870–2877.

Brosmer, J.L., and Diaconescu, P.L. (2015). Yttrium-Alkyl complexes supported by a ferrocene-based phosphinimine ligand. Organometallics *34*, 2567–2572.

Chisholm, M.H., Eilerts, N.W., Huffman, J.C., Iyer, S.S., Pacold, M., and Phomphrai, K. (2000). Molecular design of single-site metal alkoxide catalyst precursors for ring-opening polymerization reactions leading to polyoxygenates. 1. Polylactide formation by achiral and chiral Magnesium and Zinc Alkoxides, (η^3-L)MOR, where L = Trispyrazolyl- and Trisindazolylborate ligands. J. Am. Chem. Soc. *122*, 11845–11854.

Cococcioni, M., and de Gironcoli, S. (2005). Linear response approach to the calculation of the effective interaction parameters in the $\mathrm{LDA}+\mathrm{U}$ method. Phys. Rev. B *71*, 035105.

Cohen, A.J., Mori-Sánchez, P., and Yang, W. (2008). Insights into current limitations of density functional theory. Science *321*, 792–794.

D'Auria, I., Lamberti, M., Mazzeo, M., Milione, S., Roviello, G., and Pellecchia, C. (2012). Coordination chemistry and reactivity of zinc complexes supported by a phosphido pincer ligand. Chem. Eur. J. *18*, 2349–2360.

Dechy-Cabaret, O., Martin-Vaca, B., and Bourissou, D. (2004). Controlled ring-opening polymerization of lactide and glycolide. Chem. Rev. *104*, 6147–6176.

Durfey, D.A., Kirss, R.U., Frommen, C., and Reiff, W.M. (2004). Reactions of alkyl- and aryl(ferrocenyl)phosphines with 2,3-dichloro-5,6-dicyano-1,4-benzoquinone. Inorg. Chim. Acta *357*, 311–315.

Evans, D.F. (1959). 400. The determination of the paramagnetic susceptibility of substances in solution by nuclear magnetic resonance. J. Chem. Soc. 2003–2005.

Fliedel, C., Rosa, V., Alves, F.M., Martins, A.M., Aviles, T., and Dagorne, S. (2015). P,O-Phosphinophenolate zinc(ii) species: synthesis, structure and use in the ring-opening polymerization (ROP) of lactide, e-caprolactone and trimethylene carbonate. Dalton Trans. *44*, 12376–12387.

Frisch, M.J. (2010). Gaussian 09 (Revision D.01) (Gaussian Inc).

Garcés, A., Sánchez-Barba, L.F., Alonso-Moreno, C., Fajardo, M., Fernández-Baeza, J., Otero, A., Lara-Sánchez, A., López-Solera, I., and Rodríguez, A.M. (2010). Hybrid scorpionate/cyclopentadienyl magnesium and zinc complexes: synthesis, coordination chemistry, and ring-opening polymerization studies on cyclic esters. Inorg. Chem. *49*, 2859–2871.

Gowda, R.R., and Chakraborty, D. (2010). Zinc acetate as a catalyst for the bulk ring opening polymerization of cyclic esters and lactide. J. Mol. Catal. A Chem. *333*, 167–172.

Guillaume, S.M., and Carpentier, J.-F. (2012). Recent advances in metallo/organo-catalyzed immortal ring-opening polymerization of cyclic carbonates. Catal. Sci. Technol. *2*, 898–906.

Helou, M., Miserque, O., Brusson, J.-M., Carpentier, J.-F., and Guillaume, S.M. (2008). Ultraproductive, zinc-mediated, immortal ring-opening polymerization of trimethylene carbonate. Chem. Eur. J. *14*, 8772–8775.

Helou, M., Miserque, O., Brusson, J.-M., Carpentier, J.-F., and Guillaume, S.M. (2009). Highly effective and green catalytic approach toward α,ω-dihydroxy-telechelic poly(trimethylenecarbonate). Macromol. Rapid Commun. *30*, 2128–2135.

Helou, M., Miserque, O., Brusson, J.-M., Carpentier, J.-F., and Guillaume, S.M. (2010). Metal triflates as highly stable and active catalysts for the "immortal" ring-opening polymerization of trimethylene carbonate. ChemCatChem *2*, 306–313.

Higgins, T.B., and Mirkin, C.A. (1995). Model compounds for polymeric redox-switchable hemilabile ligands. Inorg. Chim. Acta *240*, 347–353.

Himmetoglu, B., Floris, A., De Gironcoli, S., and Cococcioni, M. (2014). Hubbard-corrected DFT energy functionals: the LDA+U description of correlated systems. Int. J. Quantum Chem. *114*, 14–49.

Honrado, M., Otero, A., Fernández-Baeza, J., Sánchez-Barba, L.F., Garcés, A., Lara-Sánchez, A., and Rodríguez, A.M. (2016). Copolymerization of cyclic esters controlled by chiral NNO-scorpionate zinc initiators. Organometallics *35*, 189–197.

Huang, Y., Wang, W., Lin, C.-C., Blake, M.P., Clark, L., Schwarz, A.D., and Mountford, P. (2013). Potassium, zinc, and magnesium complexes of a bulky OOO-tridentate bis(phenolate) ligand: synthesis, structures, and studies of cyclic ester polymerisation. Dalton Trans. *42*, 9313–9324.

Kulik, H.J. (2015). Perspective: Treating electron over-delocalization with the DFT+U method. J. Chem. Phys. *142*, 240901.

Kümmel, S., and Kronik, L. (2008). Orbital-dependent density functionals: theory and applications. Rev. Mod. Phys. *80*, 3–60.

Lian, B., Thomas, C.M., Casagrande, O.L., Lehmann, C.W., Roisnel, T., and Carpentier, J.-F. (2007). Aluminum and zinc complexes based on an amino-bis(pyrazolyl) ligand: synthesis, structures, and use in MMA and lactide polymerization. Inorg. Chem. *46*, 328–340.

Liang, L.-C., Lee, W.-Y., Tsai, T.-L., Hsu, Y.-L., and Lee, T.-Y. (2010). Amido phosphine complexes of zinc: synthesis, structure, and catalytic ring-opening polymerization of e-caprolactone. Dalton Trans. *39*, 8748–8758.

Lowe, M.Y., Shu, S., Quan, S.M., and Diaconescu, P.L. (2017). Investigation of redox switchable titanium and zirconium catalysts for the ring opening polymerization of cyclic esters and epoxides. Inorg. Chem. Front. *4*, 1798–1805.

Mou, Z., Liu, B., Wang, M., Xie, H., Li, P., Li, L., Li, S., and Cui, D. (2014). Isoselective ring-opening polymerization of rac-lactide initiated by achiral heteroscorpionate zwitterionic zinc complexes. Chem. Commun. *50*, 11411–11414.

Nair, L.S., and Laurencin, C.T. (2007). Biodegradable polymers as biomaterials. Prog. Polym. Sci. *32*, 762–798.

O'Keefe, B.J., Hillmyer, M.A., and Tolman, W.B. (2001). Polymerization of lactide and related cyclic esters by discrete metal complexes. J. Chem. Soc. Dalton Trans. 2215–2224.

Oerlemans, C., Bult, W., Bos, M., Storm, G., Nijsen, J.F.W., and Hennink, W.E. (2010). Polymeric micelles in anticancer therapy: targeting, imaging and triggered release. Pharm. Res. *27*, 2569–2589.

Perdew, J.P., Burke, K., and Ernzerhof, M. (1996). Generalized gradient approximation made simple. Phys. Rev. Lett. *77*, 3865–3868.

Perdew, J.P., and Zunger, A. (1981). Self-interaction correction to density-functional approximations for many-electron systems. Phys. Rev. B *23*, 5048–5079.

Place, E.S., George, J.H., Williams, C.K., and Stevens, M.M. (2009). Synthetic polymer scaffolds for tissue engineering. Chem. Soc. Rev. *38*, 1139–1151.

Platel, R.H., Hodgson, L.M., and Williams, C.K. (2008). Biocompatible initiators for lactide polymerization. Polym. Rev. *48*, 11–63.

Quan, S.M., and Diaconescu, P.L. (2015). High activity of an indium alkoxide complex toward ring opening polymerization of cyclic esters. Chem. Commun. *51*, 9643–9646.

Quan, S.M., Wang, X., Zhang, R., and Diaconescu, P.L. (2016). Redox switchable copolymerization of cyclic esters and epoxides by a zirconium complex. Macromolecules *49*, 6768–6778.

Quan, S.M., Wei, J., and Diaconescu, P.L. (2017). Mechanistic studies of redox-switchable copolymerization of lactide and cyclohexene oxide by a zirconium complex. Organometallics *36*, 4451–4457.

Ruzette, A.-V., and Leibler, L. (2005). Block copolymers in tomorrow's plastics. Nat. Mater. *4*, 19–31.

Sassano, C.A., and Mirkin, C.A. (1995). Degenerate exchange reactions: a novel and general way to determine the thermodynamic perturbations on transition metal complexes that result from ligand oxidation. J. Am. Chem. Soc. *117*, 11379–11380.

Schofield, A.D., Barros, M.L., Cushion, M.G., Schwarz, A.D., and Mountford, P. (2009). Sodium, magnesium and zinc complexes of mono(phenolate) heteroscorpionate ligands. Dalton Trans. 85–96.

Shepard, S.M., and Diaconescu, P.L. (2016). Redox-switchable hydroelementation of a cobalt complex supported by a ferrocene-based ligand. Organometallics *35*, 2446–2453.

Singewald, E.T., Mirkin, C.A., and Stern, C.L. (1995). A redox-switchable hemilabile ligand: electrochemical control of the coordination environment of a RhI complex. Angew. Chem. Int. Ed. *34*, 1624–1627.

Slone, C.S., Mirkin, C.A., Yap, G.P.A., Guzei, I.A., and Rheingold, A.L. (1997). Oxidation-state-dependent reactivity and catalytic properties of a Rh(I) complex formed from a redox-switchable hemilabile ligand. J. Am. Chem. Soc. *119*, 10743–10753.

Suriano, F., Coulembier, O., Hedrick, J.L., and Dubois, P. (2011). Functionalized cyclic carbonates: from synthesis and metal-free catalyzed ring-opening polymerization to applications. Polym. Chem. *2*, 528–533.

Tian, H., Tang, Z., Zhuang, X., Chen, X., and Jing, X. (2012). Biodegradable synthetic polymers: preparation, functionalization and biomedical application. Prog. Polym. Sci. *37*, 237–280.

Towns, J., Cockerill, T., Dahan, M., Foster, I., Gaither, K., Grimshaw, A., Hazlewood, V., Lathrop, S., Lifka, D., Peterson, G.D., et al. (2014). XSEDE: accelerating scientific discovery. Comput. Sci. Eng. *16*, 62–74.

Ulery, B.D., Nair, L.S., and Laurencin, C.T. (2011). Biomedical applications of biodegradable polymers. J. Polym. Sci. B Polym. Phys. *49*, 832–864.

Upton, B.M., Gipson, R.M., Duhovic, S., Lydon, B.R., Matsumoto, N.M., Maynard, H.D., and Diaconescu, P.L. (2014). Synthesis of ferrocene-functionalized monomers for biodegradable polymer formation. Inorg. Chem. Front. *1*, 271–277.

Verschoor-Kirss, M., Kreisz, J., Feighery, W., Reiff, W.M., Frommen, C.M., and Kirss, R.U. (2009). Synthesis and chemical oxidation of 3-ferrocenylpyrrole and ferrocenyl-substituted triazoles: iron versus ligand based oxidation. J. Organomet. Chem. *694*, 3262–3269.

Verschoor-Kirss, M.J., Hendricks, O., Verschoor, C.M., Conry, R., and Kirss, R.U. (2016). Chemical oxidation of ferrocenyl(phenyl)phosphines and ferrocenyl(phenyl)phosphine chalcogenides. Inorg. Chim. Acta *450*, 30–38.

Vert, M. (2005). Aliphatic polyesters: great degradable polymers that cannot do everything. Biomacromolecules *6*, 538–546.

Vivas, M., Mejías, N., and Contreras, J. (2003). Ring-opening polymerization of lactones initiated by diphenylzinc–coinitiator systems. Polym. Int. *52*, 1005–1009.

Vroman, I., and Tighzert, L. (2009). Biodegradable polymers. Materials *2*, 307.

Wang, X., Brosmer, J.L., Thevenon, A., and Diaconescu, P.L. (2015). Highly active yttrium catalysts for the ring-opening polymerization of ε-caprolactone and δ-valerolactone. Organometallics *34*, 4700–4706.

Wang, X., Thevenon, A., Brosmer, J.L., Yu, I., Khan, S.I., Mehrkhodavandi, P., and Diaconescu, P.L. (2014). Redox control of group 4 metal ring-opening polymerization activity toward l-lactide and ε-caprolactone. J. Am. Chem. Soc. *136*, 11264–11267.

Weinberger, D.A., Higgins, T.B., Mirkin, C.A., Stern, C.L., Liable-Sands, L.M., and Rheingold, A.L. (2001). Terthienyl and poly-terthienyl ligands as redox-switchable hemilabile ligands for oxidation-state-dependent molecular uptake and release. J. Am. Chem. Soc. *123*, 2503–2516.

Wheaton, C.A., Hayes, P.G., and Ireland, B.J. (2009). Complexes of Mg, Ca and Zn as homogeneous catalysts for lactide polymerization. Dalton Trans. 4832–4846.

Williams, C.K., Breyfogle, L.E., Choi, S.K., Nam, W., Young, V.G., Hillmyer, M.A., and Tolman, W.B. (2003). A highly active zinc catalyst for the controlled polymerization of lactide. J. Am. Chem. Soc. *125*, 11350–11359.

Wu, J., Yu, T.-L., Chen, C.-T., and Lin, C.-C. (2006). Recent developments in main group metal complexes catalyzed/initiated polymerization of lactides and related cyclic esters. Coord. Chem. Rev. *250*, 602–626.

Yang, L., Powell, D.R., and Houser, R.P. (2007). Structural variation in copper(i) complexes with pyridylmethylamide ligands: structural analysis with a new four-coordinate geometry index, [small tau]4. Dalton Trans. 955–964.

ISCI, Volume 7

Supplemental Information

Exploring Oxidation State-Dependent Selectivity in Polymerization of Cyclic Esters and Carbonates with Zinc(II) Complexes

Mark Abubekerov, Vojtěch Vlček, Junnian Wei, Matthias E. Miehlich, Stephanie M. Quan, Karsten Meyer, Daniel Neuhauser, and Paula L. Diaconescu

Table of Contents

Transparent Methods

General considerations. All reactions were performed using standard Schlenk techniques or in an MBraun drybox (<1 ppm O_2/H_2O), unless noted otherwise. All glassware, cannulas, and Celite were stored in an oven at > 425 K before being brought into the drybox. Solvents were purified using a two-column solid-state purification system by the method of Grubbs (Pangborn et al., 1996) and transferred to the glovebox without exposure to air. NMR solvents were obtained from Cambridge Isotope Laboratories, degassed, and stored over activated molecular sieves prior to use. NMR spectra were recorded at ambient temperature on Bruker AV-300, AV-400, AV-500, and DRX-500 spectrometers, unless otherwise noted. Proton and carbon chemical shifts are given relative to residual solvent peaks. Phosphorus, boron, and fluorine chemical shifts are given relative to external standards, H_3PO_4, $Et_2O{\cdot}BF_3$, and 1% Freon-113 in C_6D_6, respectively. Trimethoxybenzene was purchased from Sigma Aldrich and recrystallized from diethyl ether prior to use. L-lactide was purchased from TCI and recrystallized from THF prior to use. Liquid monomers were distilled over CaH_2 and brought into the box without exposure to air. Trimethylene carbonate (Matsuo et al., 1998), $[^{Ac}Fc][BAr^F]$ (Dhar et al., 2016), $(fc^{P,B})ZnCl{\cdot}(C_7H_8)$ (Abubekerov and Diaconescu, 2015), and $[(fc^{P,B})Zn(\mu\text{-}OCH_2Ph)]_2$ (Abubekerov et al., 2018) were prepared using literature procedures, and, unless otherwise noted, all reagents were acquired from commercial sources and used as received. Elemental analysis of $[(fc^{P,B})Zn(OCH_2Ph)]_2[BAr^F]_2$ was carried out by Midwest Microlab, LLC, Indianapolis, IN. Elemental analysis of $(fc^{P,B})Zn(OPh)$ was performed on an Exeter Analytical, Inc. CE-440 Elemental Analyzer. Molar masses of the polymers were determined by a MALS using a Shimazu Prominence-i LC 2030C 3D equipped with an autosampler, two MZ Analysentechnik MZ-Gel SDplus LS 5 μm, 300 × 8 mm linear columns, a Wyatt DAWN HELEOS-II, and a Wyatt Optilab T-rEX. The column temperature was

set at 40 °C. A flow rate of 0.70 mL/min was used, and samples were dissolved in chloroform. The number average molar mass and dispersity were found using the known concentration of the sample in chloroform with the assumption of 100% mass recovery to calculate d*n*/d*c* from the RI signal. Zero-field ^{57}Fe Mössbauer data were recorded on a WissEl spectrometer (MRG-500) at 77 K with alternating constant acceleration. ^{57}Co/Rh was used as the radiation source. The minimum experimental line width was 0.21 mm s^{-1} (full width at half-height). The temperature of the samples was controlled by an MBBC-HE0106 MÖSSBAUER He/N_2 cryostat within an accuracy of ±0.3 K. Isomer shifts were determined relative to α-iron at 298 K. Analysis and simulation of the data was done using the software "mcal" and "mf" written by E. Bill (Max Planck Institute for Chemical Energy Conversion, Mülheim an der Ruhr). All measurements were conducted with solid-state samples. The obtained solid was filled into PTFE (polytetrafluoroethylene) capsules in the glove box and placed in liquid nitrogen directly after being discharged from the glovebox. Handling and mounting of the samples were performed under liquid nitrogen. EPR spectra were recorded on a JEOL continuous wave spectrometer JES-FA200 equipped with an X-band Gunn oscillator bridge, a cylindrical mode cavity, and a helium cryostat. The samples were freshly dissolved in the respective solvent in an air-tight quartz EPR tube under nitrogen in the glovebox. The solution in the tube was frozen in liquid nitrogen upon exiting the glovebox and kept frozen until measured. Analysis and simulation of the data was done using the software "eview" and "esim" written by E. Bill (MPI for Chemical Energy Conversion, Mülheim an der Ruhr).

[(fc^{P,B})Zn(OCH$_2$Ph)]$_2$[BAr^F]$_2$. To solid [^{Ac}Fc][BAr^F] (67.8 mg, 0.062 mmol) was added [(fc^{P,B})Zn(μ-OCH$_2$Ph)]$_2$•(THF)$_2$ (55.8 mg, 0.034 mmol) in 4 mL of toluene/trifluorotoluene (1:1 vol %). The reaction mixture was stirred for 30 min at ambient temperature. The toluene solution

was decanted and the remaining oily red solids were washed with 2 × 2 mL of toluene. The product was isolated as a red solid after an hour under reduced pressure (77.8 mg, 78.0%). ^{1}H NMR (THF-d_8, 500 MHz, 298 K): δ (ppm) 2.24 (s), 2.39 (s), 4.40 (s), 4.43 (s), 4.63 (s), 4.66 (s), 6.07 (s), 7.09 (t), 7.14 (s), 7.28 (t), 7.58 (s), 7.71 (m), 7.79 (s), 8.95 (br s), 10.64 (br s). ^{11}B NMR (THF-d_8, 161 MHz, 298 K): δ (ppm) -5.9 (s), -7.8 (br s, $\Delta\nu_{1/2}$ = 289.2 Hz). ^{19}F NMR (THF-d_8, 376 MHz, 298 K): δ (ppm) -63.5 (s). Anal. Calcd: [($fc^{P,B}$)Zn(OCH_2Ph)][BAr^F] ($C_{71}H_{52}B_2F_{24}FeN_4OPZn$) C, 53.07; H, 3.26; N, 3.49. Found: C, 53.17; H, 3.32; N, 3.54.

($fc^{P,B}$)Zn(OPh). To ($fc^{P,B}$)ZnCl·(C_7H_8) (121.1 mg, 0.158 mmol) in 4 mL of methylene chloride was added solid NaOPh (27.6 mg, 0.238 mmol) and the suspension stirred for 1 h at ambient temperature. The reaction mixture was filtered through Celite and volatile substances were removed under reduced pressure. The remaining oily solids were dissolved in 2 mL of diethyl ether and stored at -35 °C for several hours. Decanting of the solution and washing with cold diethyl ether yielded the product as orange crystals (101.4 mg, 79.8%). X-ray quality crystals were obtained from diethyl ether at -35 °C. Crystals of ($fc^{P,B}$)Zn(OPh) always contain a molecule of diethyl ether per molecule of compound as supported by NMR data. ^{1}H NMR (C_6D_6, 500 MHz, 298 K): δ (ppm) 2.21 (s, 6H, C*H*$_3$), 2.27 (s, 6H, C*H*$_3$), 3.53 (q, 2H, Cp-*H*), 3.93(t, 2H, Cp-*H*), 4.00 (t, 2H, Cp-*H*), 4.04 (t, 2H, Cp-*H*), 4.70 (br s, 1H, B*H*), 5.69 (s, 2H, C*H*), 6.68 (m, 1H, *p*-Ph), 6.89 (m, 2H, *m*-Ph), 7.02 (m, 6H, *m*-Ph, *p*-Ph), 7.15 (m, 2H, *o*-Ph), 7.98 (m, 4H, *o*-Ph). ^{13}C NMR (C_6D_6, 126 MHz, 298 K): δ (ppm) 13.3 (s, *C*H$_3$), 14.0 (s, *C*H$_3$), 68.1 (d, Cp-*C*), 68.2 (s, Cp-*C*), 69.6 (s, Cp-*C*), 72.2 (d, Cp-*C*), 72.6 (s, Cp-*C*), 75.1 (s, Cp-*C*), 106.8 (s, *C*H), 115.4 (s, aromatic), 119.4 (s, aromatic), 129.3 (d, aromatic), 130.2 (s, aromatic), 131.2 (d, aromatic), 131.4 (d, aromatic), 134.5 (d, aromatic), 147.9 (s, *C*CH$_3$), 150.1 (s, *C*CH$_3$), 168.0 (d, aromatic). ^{31}P{^{1}H} NMR (C_6D_6, 203 MHz, 298 K): δ (ppm) -15.5 (s). ^{11}B NMR (C_6D_6, 161 MHz, 298 K): δ (ppm) -7.0 (br s, $\Delta\nu_{1/2}$ =

343.7 Hz). Anal. Calcd: ($fc^{P,B}$)Zn(OPh)·(Et_2O) ($C_{42}H_{48}BFeN_4O_2PZn$) C, 62.75; H, 6.02; N, 6.97. Found: C, 61.83; H, 5.81; N, 6.75.

NMR Scale Polymerizations. To a small vial, [($fc^{P,B}$)Zn(μ-OCH_2Ph)]$_2$ (2.5 μmol), an external standard, hexamethylbenzene (0.025 mmol), the monomer (0.5 mmol), and 0.5 mL of C_6D_6 were added. The contents of the vial were stirred and the homogeneous solution was transferred to a J. Young NMR tube equipped with a Teflon valve. The NMR tube was sealed, taken out of the box and placed in an oil bath. The polymerization was monitored by ^{1}H NMR spectroscopy until the conversion stopped or reached completion. The contents of the NMR tube were diluted with 0.5 mL of dichloromethane and poured into 10 mL of methanol to yield white solids. The product was collected on a glass frit, washed with additional 5 mL of methanol and kept under reduced pressure until it reached a consistent weight. For the control experiments, [^{Ac}Fc][BAr^F] (5 μmol) was used instead of [($fc^{P,B}$)Zn(μ-OCH_2Ph)]$_2$ under similar conditions as above (Figures S14-S17).

Electrochemical studies. Cyclic voltammetry studies were carried out in a 20 mL scintillation vial with electrodes fixed in position by a rubber stopper, in a 0.10 M tetrabutylammonium hexafluorophosphate solution in THF. A glassy carbon working electrode (planar circular area = 0.071 cm^2), a platinum reference electrode (planar circular area = 0.031 cm^2), and a silver-wire pseudo-reference electrode were purchased from CH Instruments. Before each cyclic voltammogram was recorded, the working and auxiliary electrodes were polished with an aqueous suspension of 0.05 μm alumina on a Microcloth polishing pad. Cyclic voltammograms were acquired with a CH Instruments CHI630D potentiostat and recorded with CH Instruments software (version 13.04) with data processing on Origin 9.2. All potentials are given with respect to the ferrocene-ferrocenium couple.

X-ray crystallography. X-ray quality crystals were obtained from various concentrated solutions placed in a -35 °C freezer in the glove box unless otherwise specified. Inside the glove box, the crystals were coated with oil (STP Oil Treatment) on a microscope slide, which was brought outside the glove box. The X-ray data collections were carried out on a Bruker SMART 1000 single crystal X-ray diffractometer using MoK_{α} radiation and a SMART APEX CCD detector. The data was reduced by SAINTPLUS and an empirical absorption correction was applied using the package SADABS. The structure was solved and refined using SHELXTL (Brucker 1998, SMART, SAINT, XPREP, AND SHELXTL, Brucker AXS Inc., Madison, Wiscosin, USA). Tables with atomic coordinates and equivalent isotropic displacement parameters, with all the distances and angles, and with anisotropic displacement parameters are listed in the cif.

DFT calculations. All calculations were carried out with the GAUSSIAN 09 program package. Geometry optimizations were performed with B3LYP (Becke, 1993a, Lee et al., 1988, Becke, 1993b). The LANL2DZ basis set (Hay and Wadt, 1985, Roy et al., 2008, Ehlers et al., 1993) with ECP was used for Zn and Fe, and the 6-31G(d) basis set (Ditchfield et al., 1971, Hehre et al., 1972, Hariharan and Pople, 1973) was used for other atoms. Frequency analysis was conducted at the same level of theory to verify that the stationary points are minima or saddle points. The single point energies and solvent effects in benzene were computed with PBE1PBE (Perdew et al., 1996) / SDD-6-311+G(d,p) basis sets (Dolg et al., 1987) by using the PCM solvation model (Scalmani and Frisch, 2010). The D3 version of Grimme's dispersion was applied for the dispersion correction (Grimme et al., 2010). All enthalpies and the Gibbs free energies are given in Hartree.

Electronic structure calculations. The electronic structure of the system was investigated with the Quantum Espresso software package (Paolo et al., 2009) by using the geometry optimized with

Gaussian 09 (see “DFT calculations” paragraph). For the exchange-correlation, a PBE generalized gradient approximation was used. This approach was combined with a U parameter obtained with the approach of Cococcioni & de Gironcoli (Cococcioni and de Gironcoli, 2005). Projected augmented wave pseudopotentials were used for all atoms. The kinetic energy cutoffs were 50 and 400 Ry for the planewave and density expansions, respectively. The total energy was converged to 0.05 Ry and the eigenvalues to 0.01 eV.

NMR Spectra

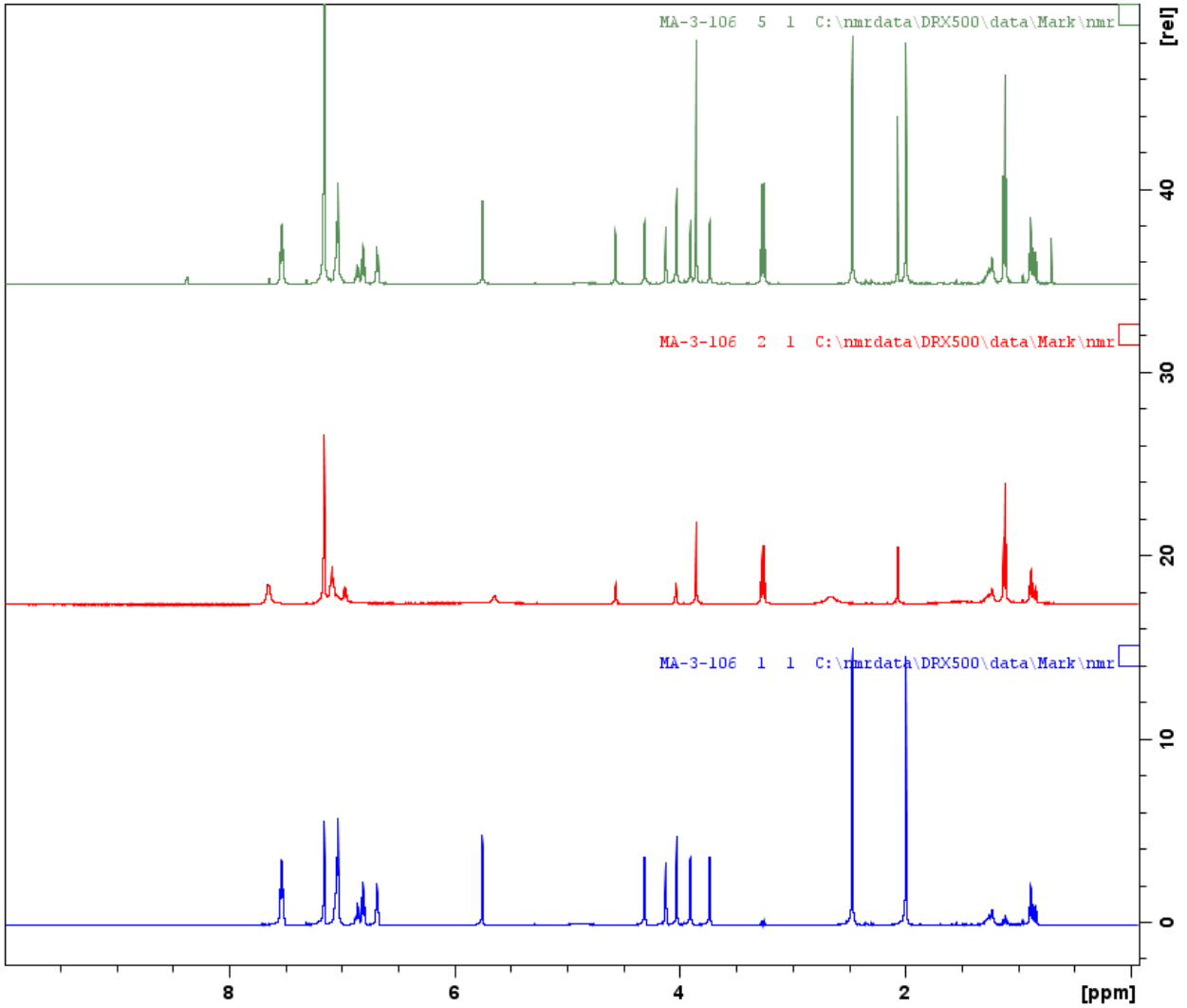

Figure S1. ^{1}H NMR spectra (C_6D_6, 500 MHz, 298 K) of $[(fc^{P,B})Zn(\mu\text{-}OCH_2Ph)]_2$ (bottom), $[(fc^{P,B})Zn(\mu\text{-}OCH_2Ph)]_2$ + $[^{Ac}Fc][BAr^F]$ (middle), $[(fc^{P,B})Zn(\mu\text{-}OCH_2Ph)]_2$ + $[^{Ac}Fc][BAr^F]$ + Cp_2Co (top); related to Equation 1.

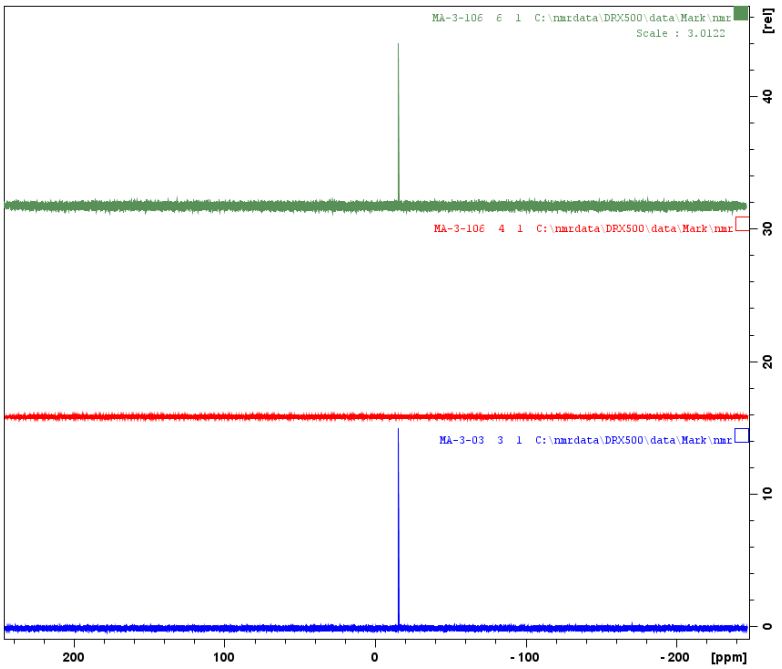

Figure S2. $^{31}P\{^{1}H\}$ NMR spectra (C_6D_6, 202 MHz, 298 K) of $[(fc^{P,B})Zn(\mu\text{-}OCH_2Ph)]_2$ (bottom), $[(fc^{P,B})Zn(\mu\text{-}OCH_2Ph)]_2$ + $[^{Ac}Fc][BAr^F]$ (middle), $[(fc^{P,B})Zn(\mu\text{-}OCH_2Ph)]_2$ + $[^{Ac}Fc][BAr^F]$ + Cp_2Co (top); related to Equation 1.

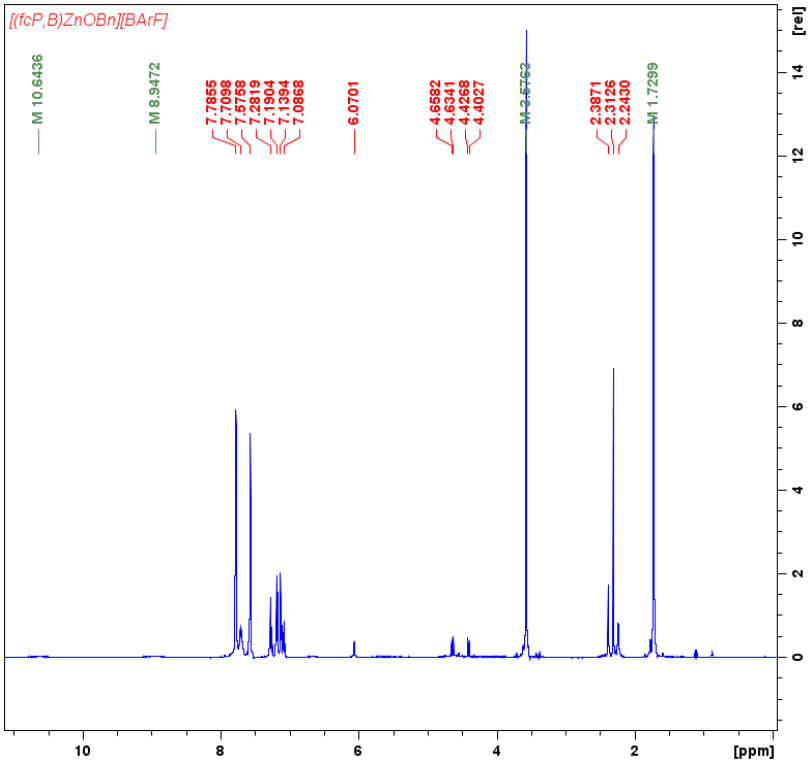

Figure S3. ^{1}H NMR spectrum (THF-d_8, 500 MHz, 298 K) of $[(fc^{P,B})Zn(\mu\text{-}OCH_2Ph)]_2[BAr^F]_2$: δ (ppm) 2.24 (s), 2.39 (s), 4.40 (s), 4.43 (s), 4.63 (s), 4.66 (s), 6.07 (s), 7.09 (t), 7.14 (s), 7.28 (t), 7.58 (s), 7.71 (m), 7.79 (s), 8.95 (br s), 10.64 (br s). Peaks at 2.31 ppm, 7.10 ppm and 7.19 ppm are attributed to residual toluene; related to Equation 1.

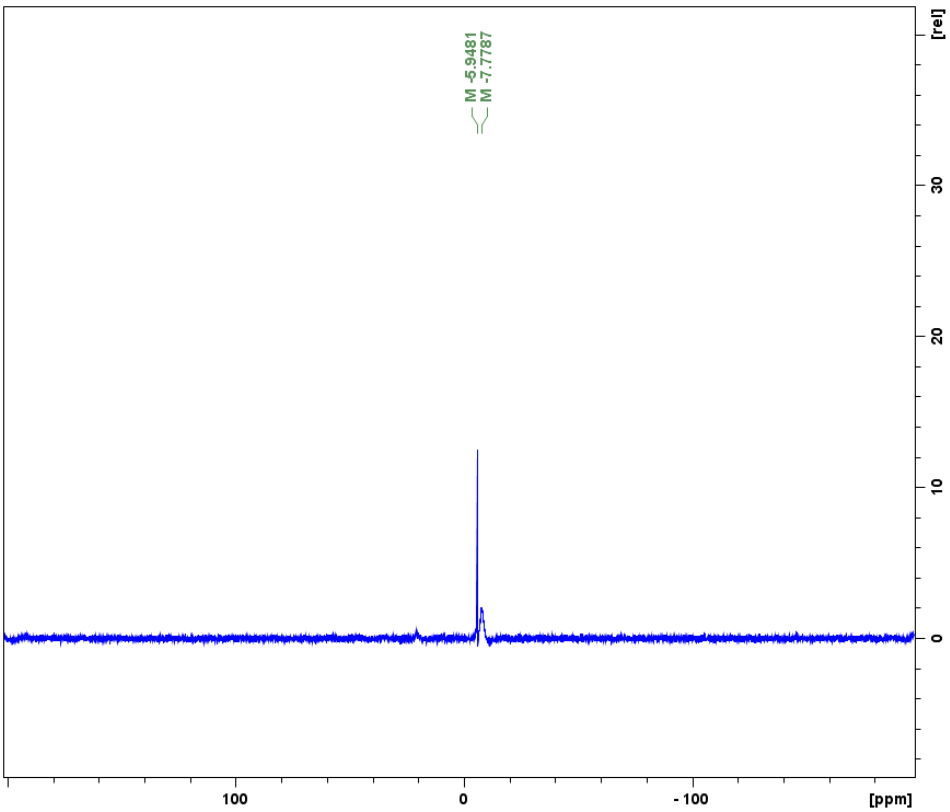

Figure S4. ^{11}B NMR spectrum (THF-d_8, 161 MHz, 298 K) of $[(fc^{P,B})Zn(\mu\text{-}OCH_2Ph)]_2[BAr^F]_2$: δ (ppm) -5.9 (s), -7.8 (br s); related to Equation 1.

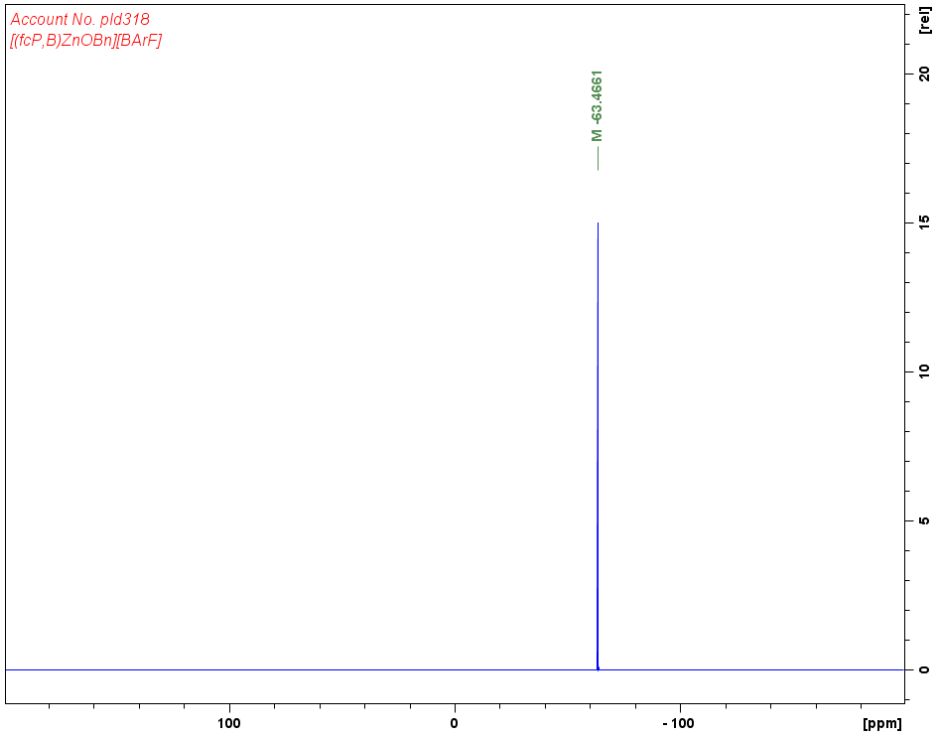

Figure S5. ^{19}F NMR spectrum (THF-d_8, 376 MHz, 298 K) of $[(fc^{P,B})Zn(\mu\text{-}OCH_2Ph)]_2[BAr^F]_2$: δ (ppm) -63.5 (s); related to Equation 1.

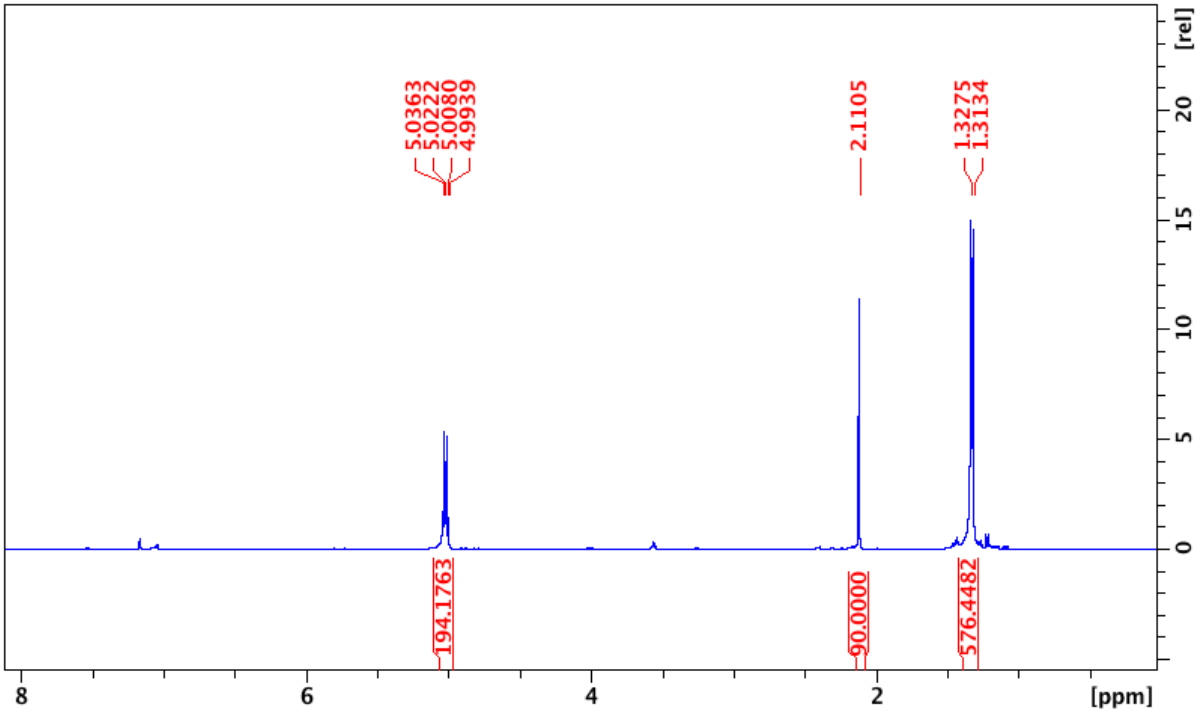

Figure S6. ^{1}H NMR spectrum (C_6D_6, 500 MHz, 298 K) of L-lactide (LA) polymerization. The standard is hexamethylbenzene (HMB). Compound [(fc^{P,B})Zn(μ-OCH$_2$Ph)]$_2$: HMB : LA ratio is 1:10:194. δ (ppm) 1.32 (d, 6H, CHC*H*$_3$ PLA), 2.11 (s, 18H, C*H*$_3$ HMB), 5.01 (q, 2H, C*H*CH$_3$ PLA); related to Table 1, entry 1.

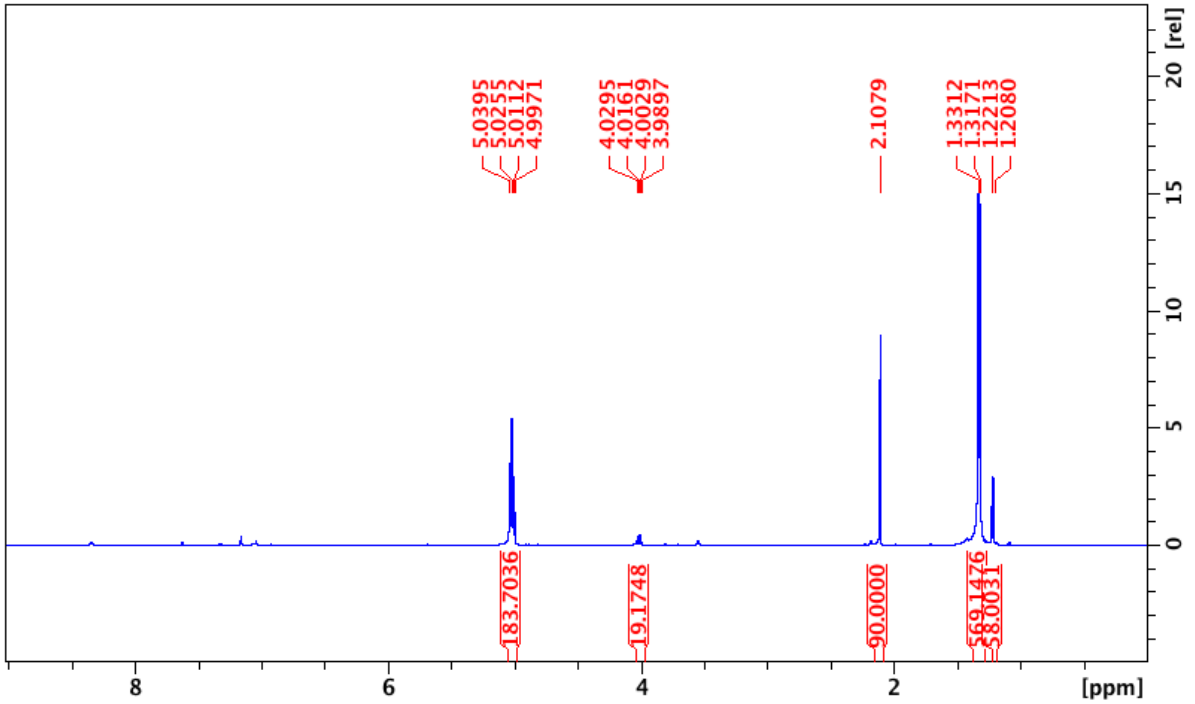

Figure S7. ^{1}H NMR spectrum (C_6D_6, 500 MHz, 298 K) of L-lactide (LA) polymerization. The standard is hexamethylbenzene (HMB). Compound [(fc^{P,B})Zn(μ-OCH$_2$Ph)]$_2$[BAr^{F}]$_2$: HMB : LA ratio is 1:10:184. δ (ppm) 1.21 (d, 6H, CHC*H*$_3$ LA), 1.32 (d, 6H, CHC*H*$_3$ PLA), 2.11 (s, 18H, C*H*$_3$ HMB), 4.01 (q, 2H, C*H*CH$_3$ LA), 5.01 (q, 2H, C*H*CH$_3$ PLA); related to Table 1, entry 2.

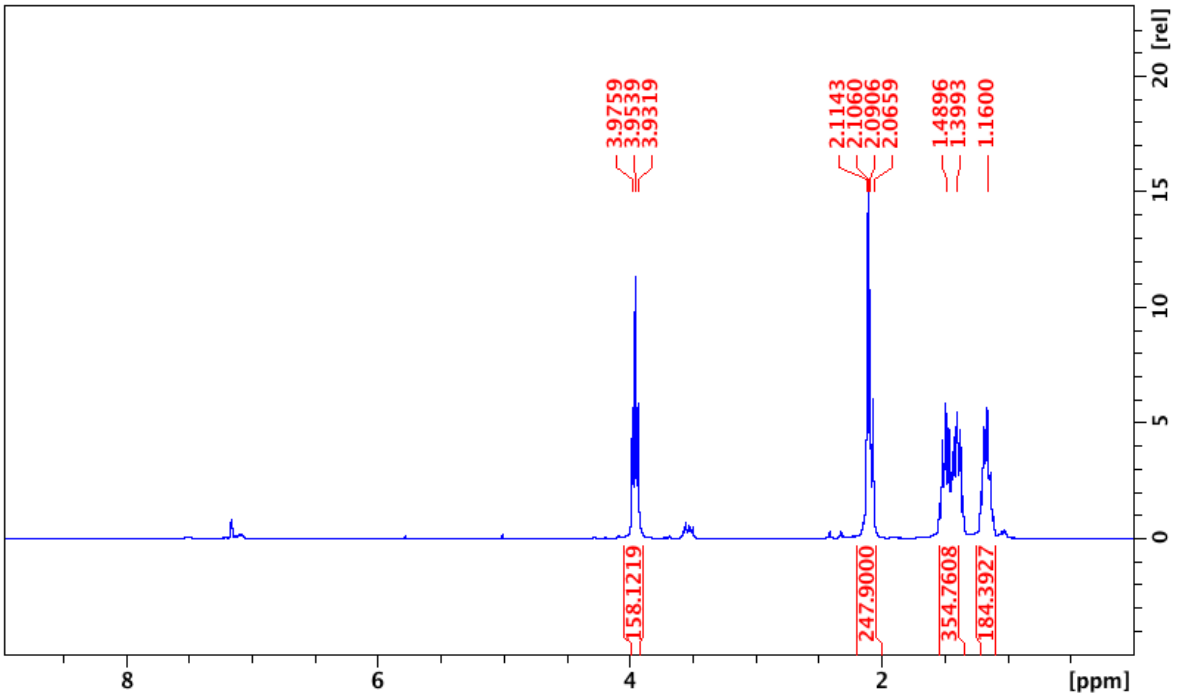

Figure S8. ^{1}H NMR spectrum (C_6D_6, 300 MHz, 298 K) of ε-caprolactone (CL) polymerization. The standard is hexamethylbenzene (HMB). Compound $[(fc^{P,B})Zn(\mu\text{-}OCH_2Ph)]_2$: HMB : CL ratio is 1:10:158. δ (ppm) 1.0–1.6 (6H, C*H*$_2$ PCL), 2.09 (t, 2H, C*H*$_2$ PCL), 2.11 (s, 18H, C*H*$_3$ HMB), 3.95 (t, 2H, C*H*$_2$ PCL); related to Table 1, entry 3.

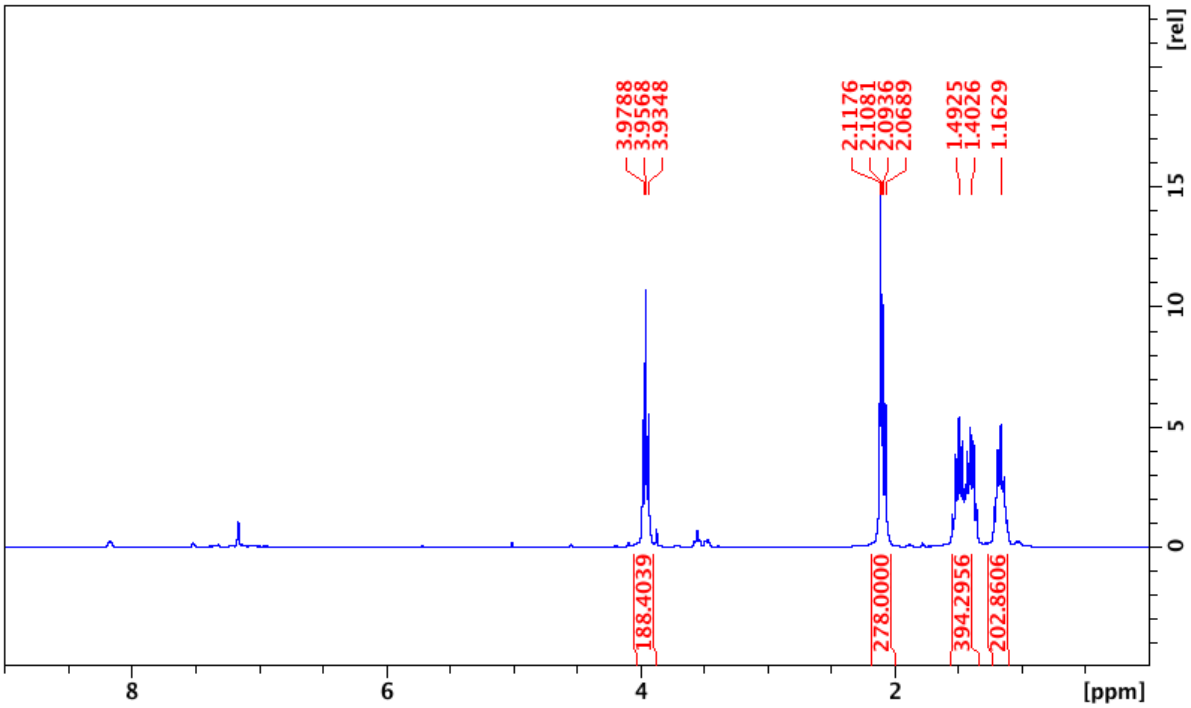

Figure S9. ^{1}H NMR spectrum (C_6D_6, 300 MHz, 298 K) of ε-caprolactone (CL) polymerization. The standard is hexamethylbenzene (HMB). Compound $[(fc^{P,B})Zn(\mu\text{-}OCH_2Ph)]_2[BAr^F]_2$: HMB : CL ratio is 1:10:188. δ (ppm) 1.0–1.6 (6H, C*H*$_2$ PCL), 2.09 (t, 2H, C*H*$_2$ PCL), 2.11 (s, 18H, C*H*$_3$ HMB), 3.95 (t, 2H, C*H*$_2$ PCL); related to Table 1, entry 4.

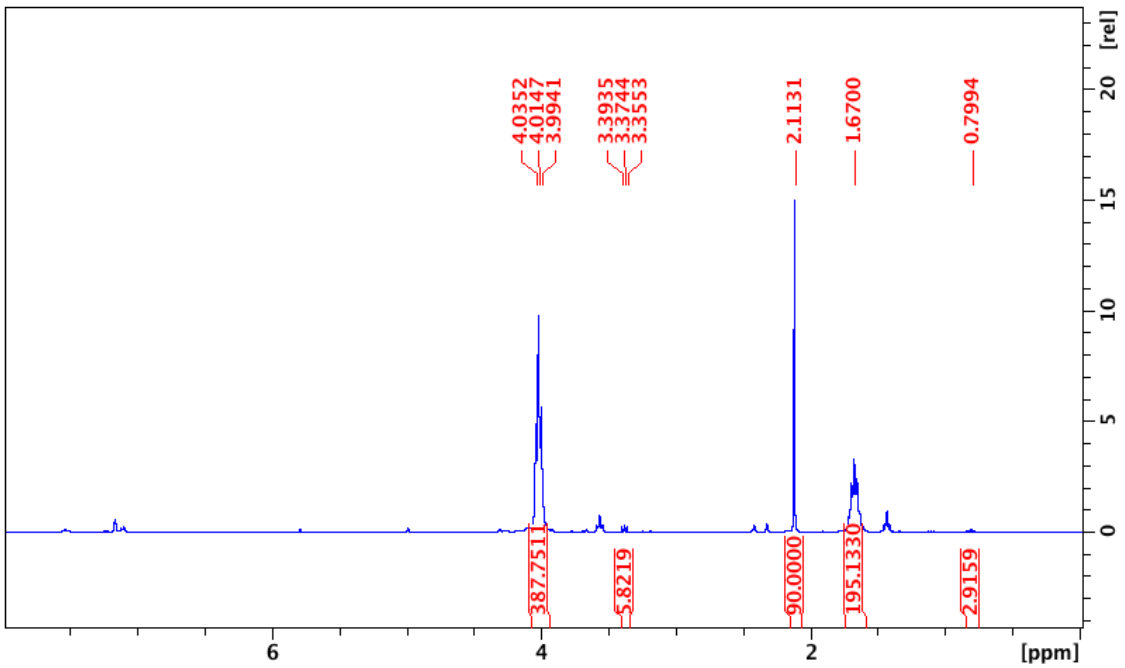

Figure S10. ^{1}H NMR spectrum (C_6D_6, 500 MHz, 298 K) of trimethylene carbonate (TMC) polymerization. The standard is hexamethylbenzene (HMB). Compound [($fc^{P,B}$)Zn(μ-OCH_2Ph)]$_2$: HMB : TMC ratio is 1:10:194. δ (ppm) 0.80 (t, 2H, C*H*$_2$ TMC), 1.67 (t, 2H, C*H*$_2$ PTMC), 2.11 (s, 18H, C*H*$_3$ HMB), 3.37 (t, 4H, C*H*$_2$ TMC), 4.01 (t, 4H, C*H*$_2$ PTMC); related to Table 1, entry 5.

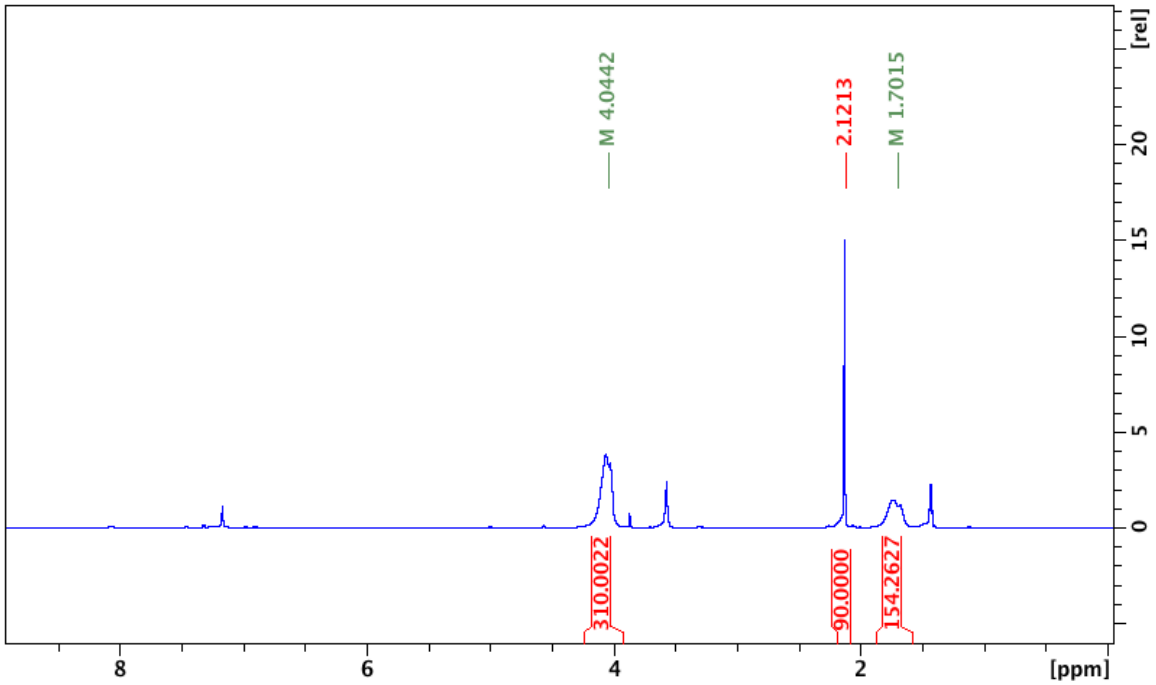

Figure S11. ^{1}H NMR spectrum (C_6D_6, 500 MHz, 298 K) of trimethylene carbonate (TMC) polymerization. The standard is hexamethylbenzene (HMB). Compound [($fc^{P,B}$)Zn(μ-OCH_2Ph)]$_2$[BAr^F]$_2$: HMB : TMC ratio is 1:10:156. δ (ppm) 1.70 (br s, 2H, C*H*$_2$ PTMC), 2.12 (s, 18H, C*H*$_3$ HMB), 4.00 (br s, 4H, C*H*$_2$ PTMC); related to Table 1, entry 6.

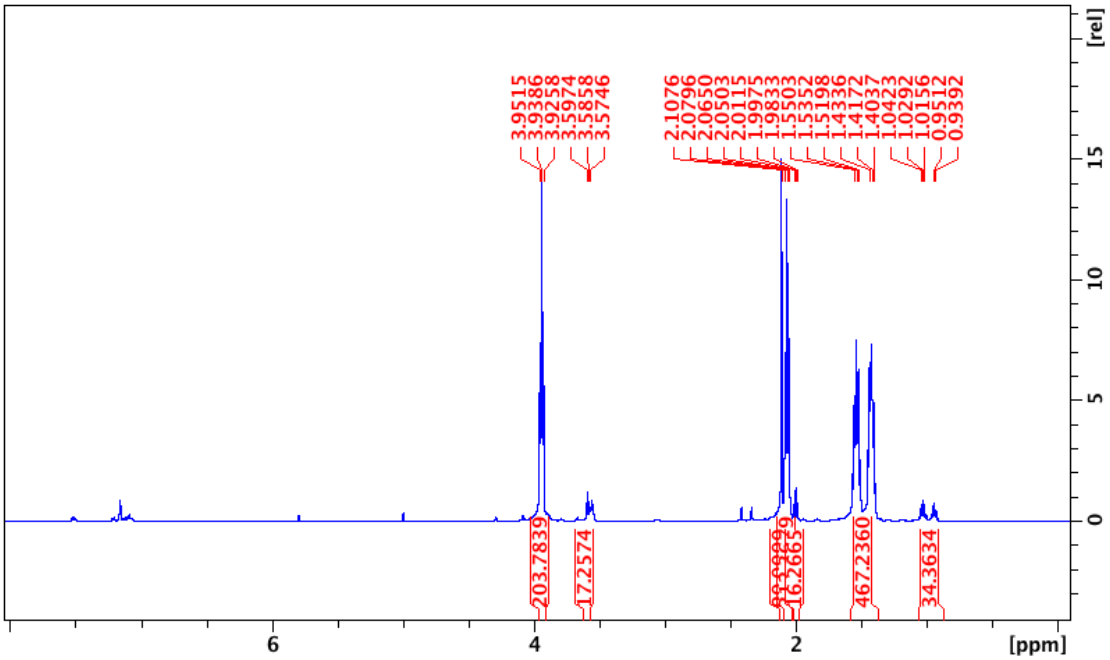

Figure S12. ^{1}H NMR spectrum (C_6D_6, 500 MHz, 298 K) of δ-valerolactone (VL) polymerization. The standard is hexamethylbenzene (HMB). Compound [(fc^{P,B})Zn(μ-OCH$_2$Ph)]$_2$: HMB : VL ratio is 1:10:204. δ (ppm) 0.95 (m, 2H, C*H*$_2$ VL), 1.03 (m, 2H, C*H*$_2$ VL), 1.42 (m, 2H, C*H*$_2$ PVL), 1.54 (m, 2H, C*H*$_2$ PVL), 2.00 (t, 2H, C*H*$_2$ VL), 2.07 (t, 2H, C*H*$_2$ PVL), 2.11 (s, 18H, C*H*$_3$ HMB), 3.59 (t, 2H, C*H*$_2$ VL), 3.94 (t, 2H, C*H*$_2$ PVL); related to Table 1, entry 7.

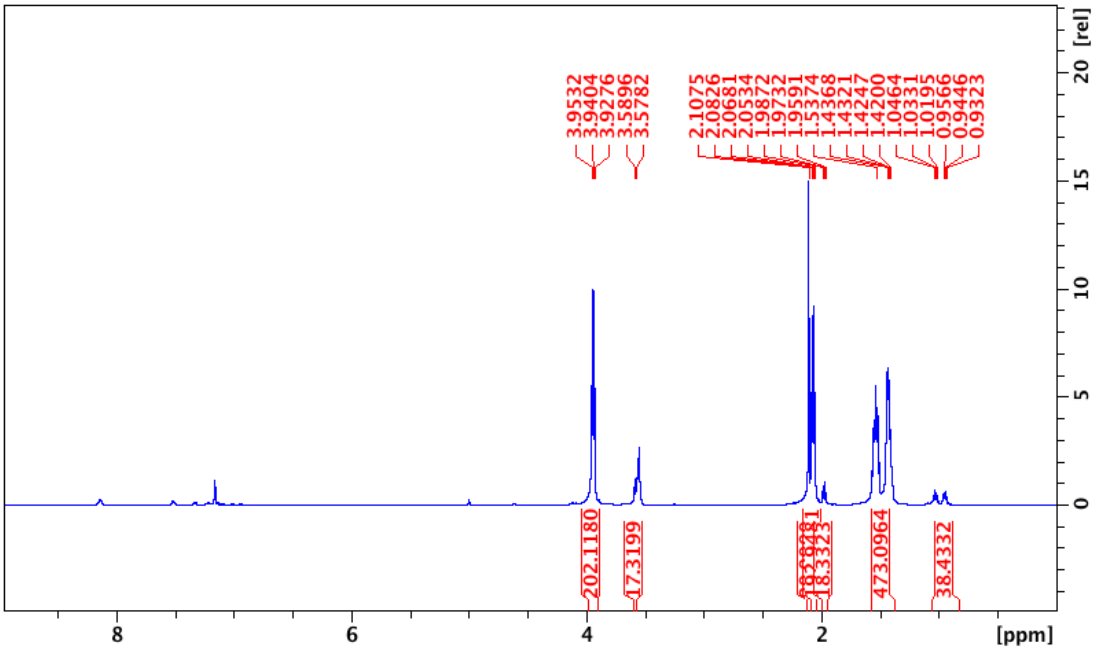

Figure S13. ^{1}H NMR spectrum (C_6D_6, 500 MHz, 298 K) of δ-valerolactone (VL) polymerization. The standard is hexamethylbenzene (HMB). Compound [(fc^{P,B})Zn(μ-OCH$_2$Ph)]$_2$[BAr^{F}]$_2$: HMB : VL ratio is 1:10:202. δ (ppm) 0.95 (m, 2H, C*H*$_2$ VL), 1.03 (m, 2H, C*H*$_2$ VL), 1.42 (m, 2H, C*H*$_2$ PVL), 1.54 (m, 2H, C*H*$_2$ PVL), 2.00 (t, 2H, C*H*$_2$ VL), 2.07 (t, 2H, C*H*$_2$ PVL), 2.11 (s, 18H, C*H*$_3$ HMB), 3.59 (t, 2H, C*H*$_2$ VL), 3.94 (t, 2H, C*H*$_2$ PVL); related to Table 1, entry 8.

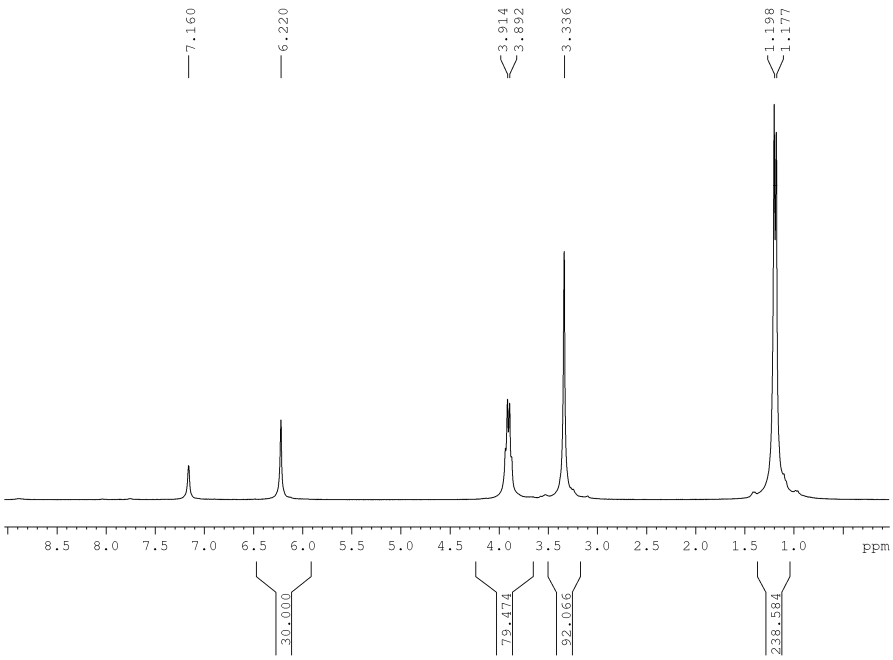

Figure S14. Control experiment of 40 equivalents of L-lactide (LA) with 5 equivalents of [^{Ac}Fc][BAr^{F}] at 70 °C for 3 h; related to Table 1.

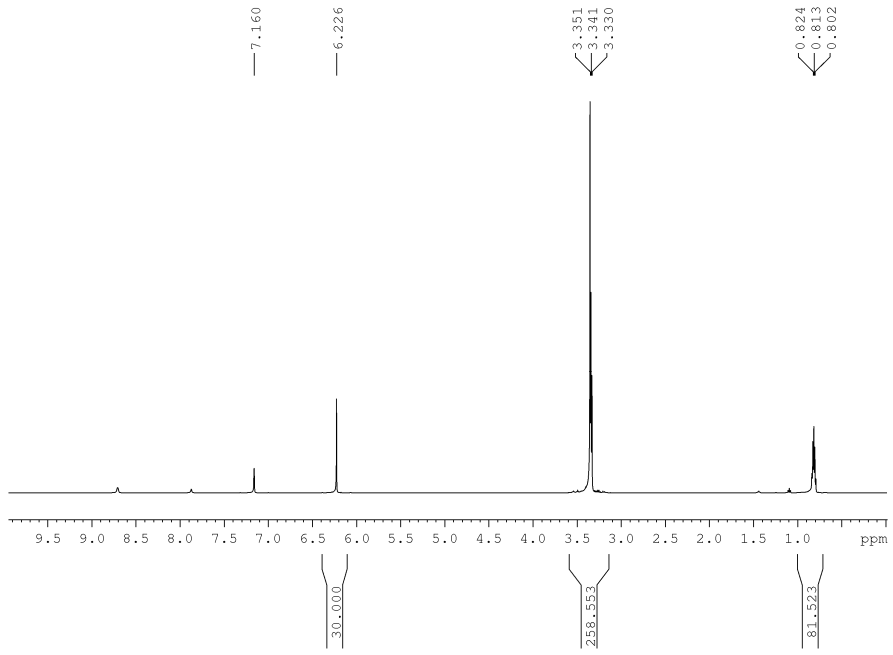

Figure S15. Control experiment of 40 equivalents of trimethylene carbonate (TMC) with 5 equivalents of [^{Ac}Fc][BAr^{F}] at ambient temperature for 2 h; related to Table 1.

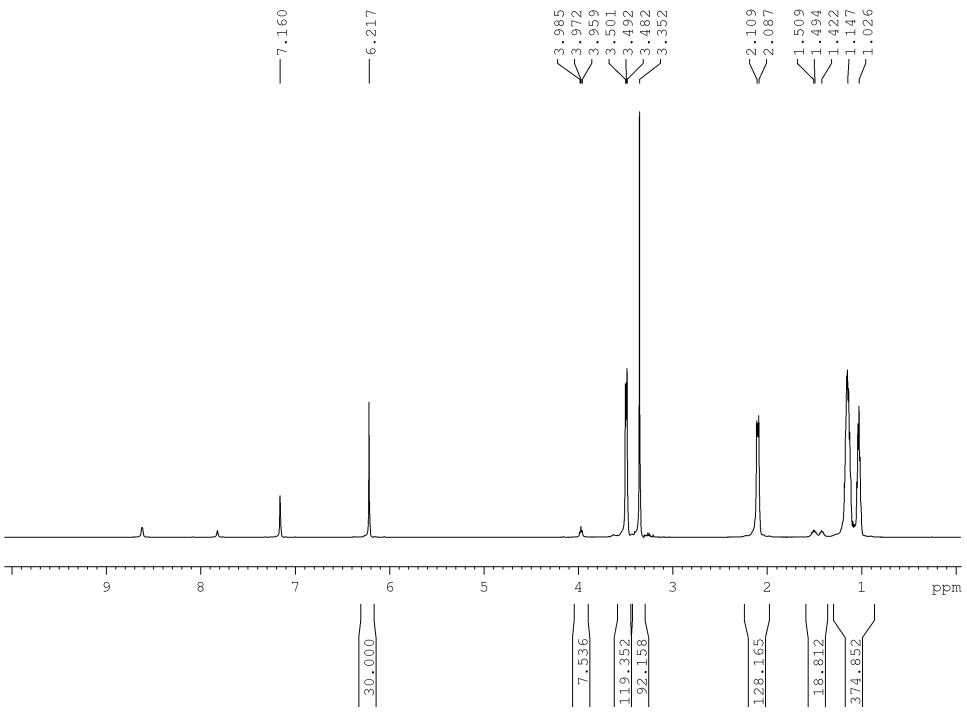

Figure S16. Control experiment of 64 equivalents of ε-caprolactone (CL) with 5 equivalents of [^{Ac}Fc][BAr^{F}] at 70°C for 1 h; related to Table 1.

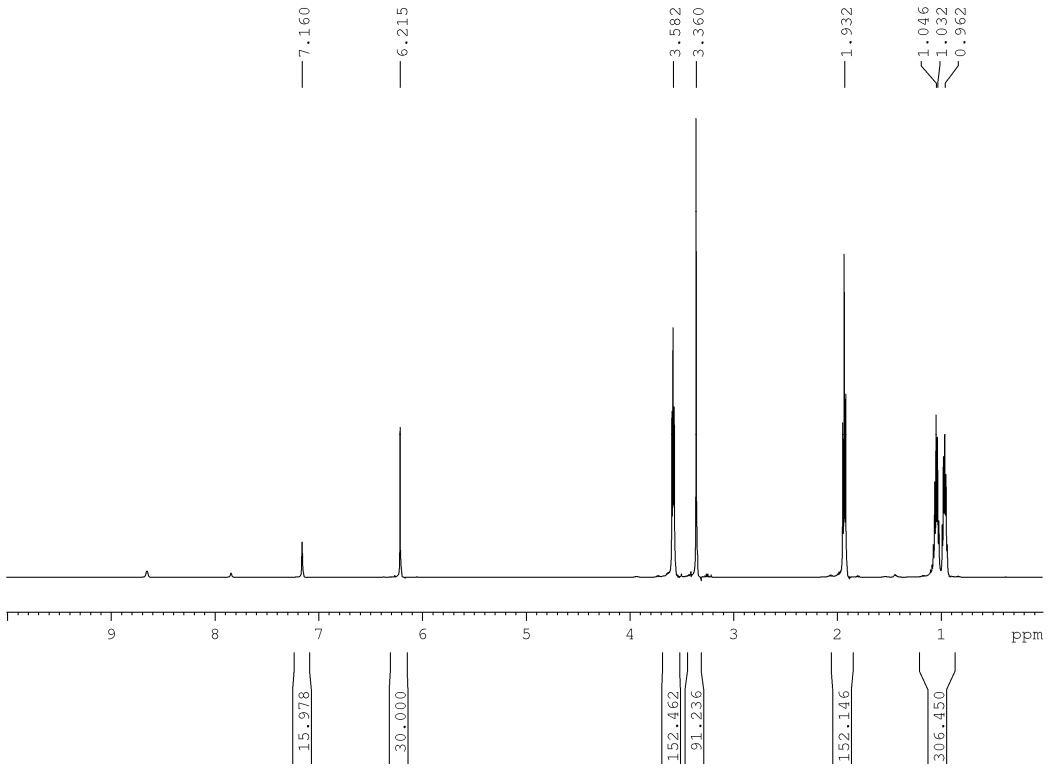

Figure S17. Control experiment of 76 equivalents of δ-valerolactone (VL) with 5 equivalents of [^{Ac}Fc][BAr^{F}] at ambient temperature for 2 h; related to Table 1.

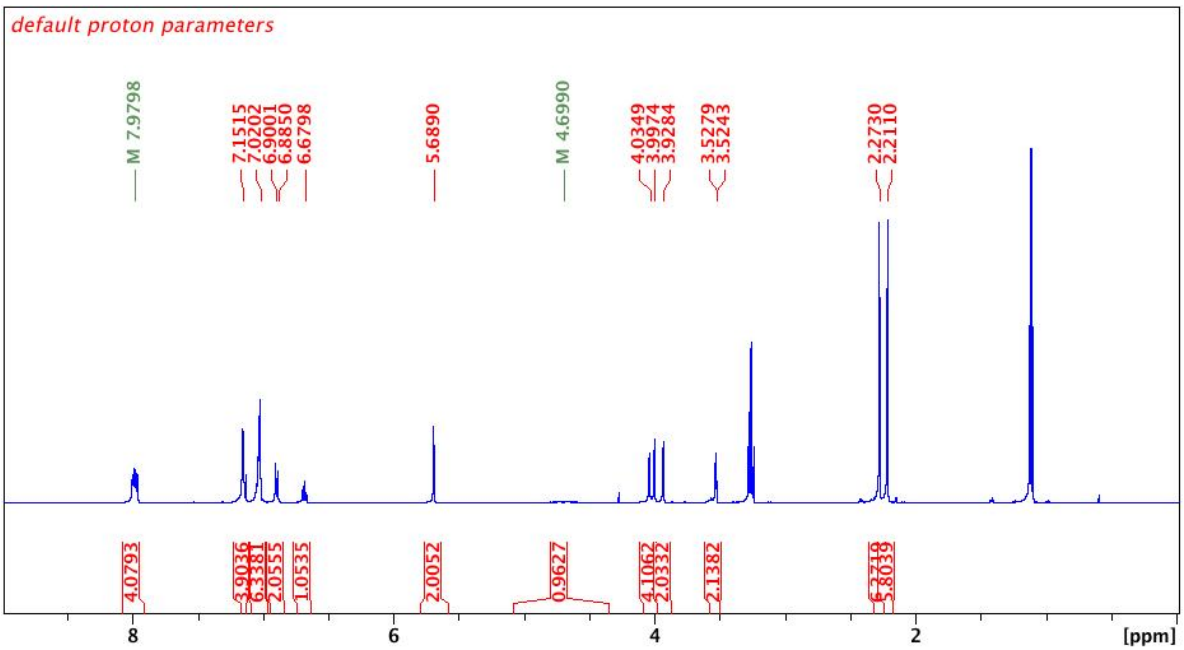

Figure S18. ^{1}H NMR spectrum (C_6D_6, 500 MHz, 298 K) of ($fc^{P,B}$)Zn(OPh): δ (ppm) 2.21 (s, 6H, C*H*$_3$), 2.27 (s, 6H, C*H*$_3$), 3.53 (q, 2H, Cp-*H*), 3.93(t, 2H, Cp-*H*), 4.00 (t, 2H, Cp-*H*), 4.04 (t, 2H, Cp-*H*), 4.70 (br s, 1H, B*H*), 5.69 (s, 2H, C*H*), 6.68 (m, 1H, *p*-Ph), 6.89 (m, 2H, *m*-Ph), 7.02 (m, 6H, *m*-Ph, *p*-Ph), 7.15 (m, 2H, *o*-Ph), 7.98 (m, 4H, *o*-Ph). The peaks at 1.11 and 3.53 are attributed to co-crystallized diethyl ether; related to Equation 2.

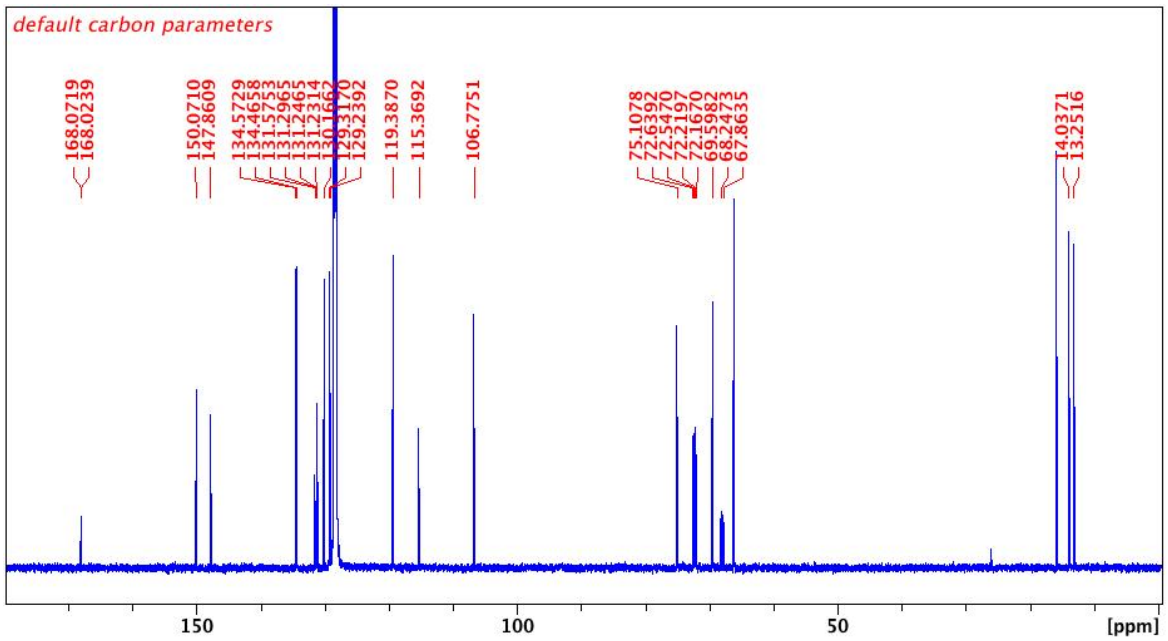

Figure S19. ^{13}C NMR spectrum (C_6D_6, 126 MHz, 298 K) of ($fc^{P,B}$)Zn(OPh): δ (ppm) 13.3 (s, *C*H$_3$), 14.0 (s, *C*H$_3$), 68.1 (d, Cp-*C*), 68.2 (s, Cp-*C*), 69.6 (s, Cp-*C*), 72.2 (d, Cp-*C*), 72.6 (s, Cp-*C*), 75.1 (s, Cp-*C*), 106.8 (s, *C*H), 115.4 (s, aromatic), 119.4 (s, aromatic), 129.3 (d, aromatic), 130.2 (s, aromatic), 131.2 (d, aromatic), 131.4 (d, aromatic), 134.5 (d, aromatic), 147.9 (s, *C*CH$_3$), 150.1 (s, *C*CH$_3$), 168.0 (d, aromatic). The peaks at 15.9 and 66.3 are attributed to co-crystallized diethyl ether; related to Equation 2.

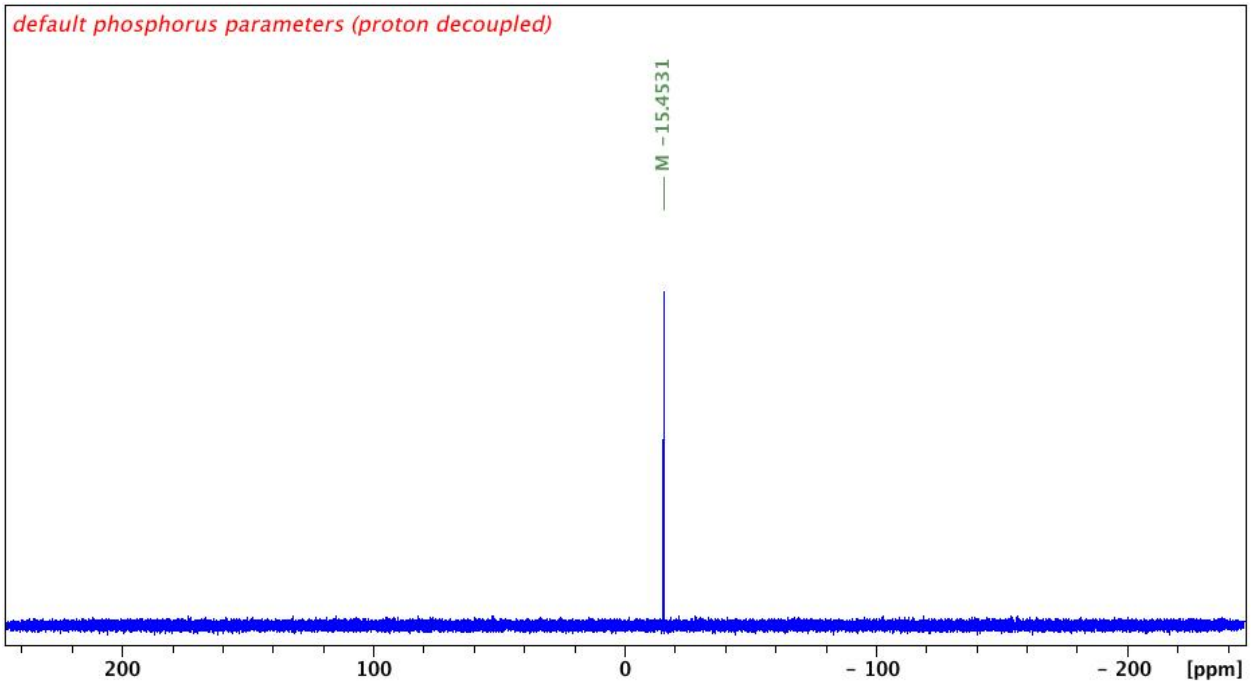

Figure S20. $^{31}P\{^{1}H\}$ NMR spectrum (C_6D_6, 203 MHz, 298 K) of ($fc^{P,B}$)Zn(OPh): δ (ppm) -15.5 (s); related to Equation 2.

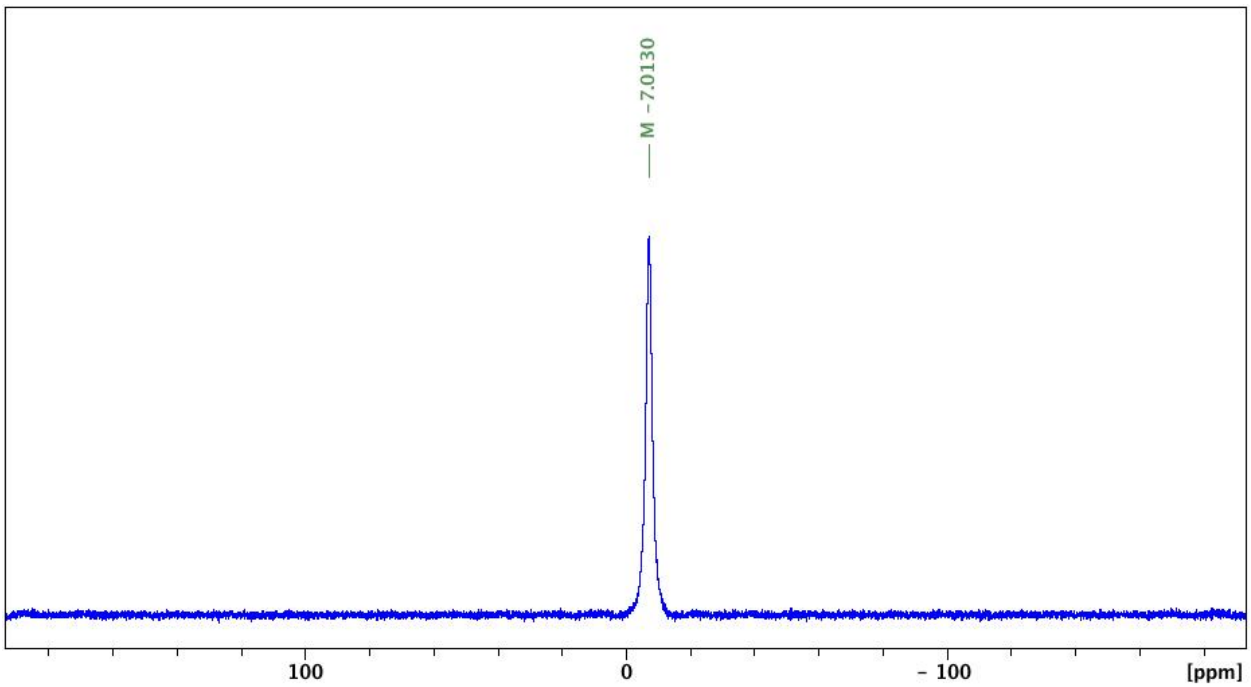

Figure S21. ^{11}B NMR spectrum (C_6D_6, 161 MHz, 298 K) of ($fc^{P,B}$)Zn(OPh): δ (ppm) -7.0 (br s); related to Equation 2.

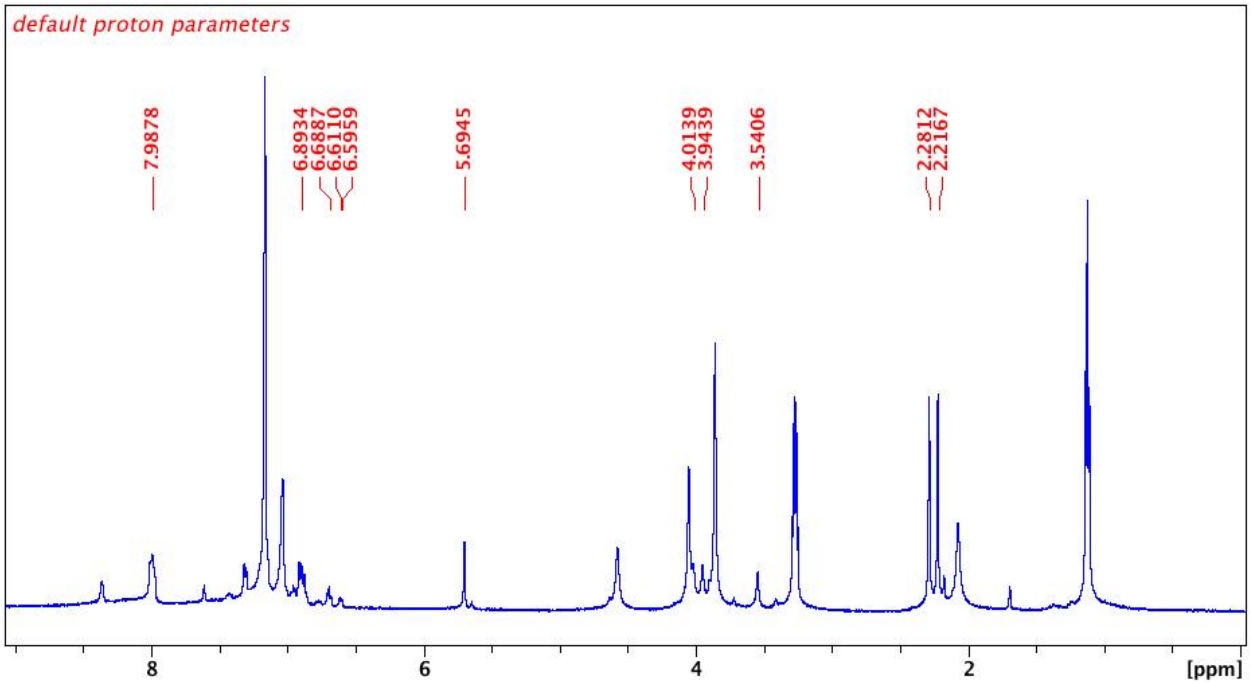

Figure S22. ^{1}H NMR spectrum (C_6D_6, 500 MHz, 298 K) of ($fc^{P,B}$)Zn(OPh) + [^{Ac}Fc][BAr^{F}]; related to Equation 2.

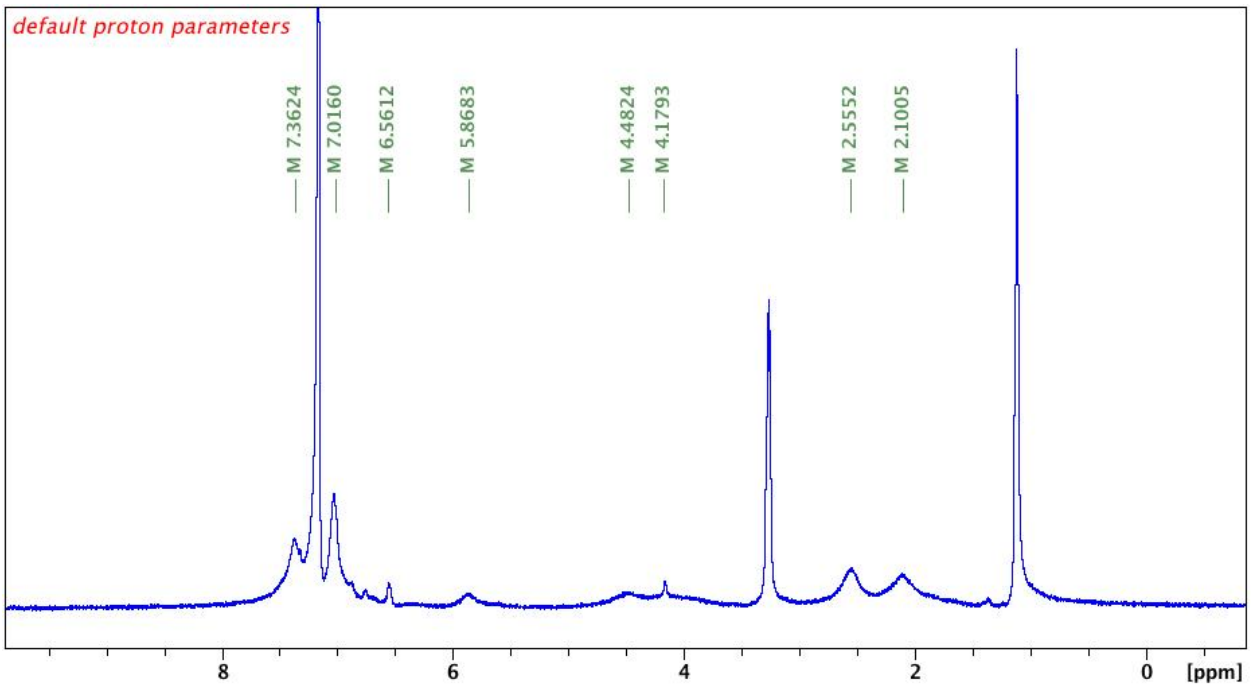

Figure S23. ^{1}H NMR spectrum (C_6D_6, 500 MHz, 298 K) of ($fc^{P,B}$)Zn(OPh) + $AgBF_4$; related to Equation 2.

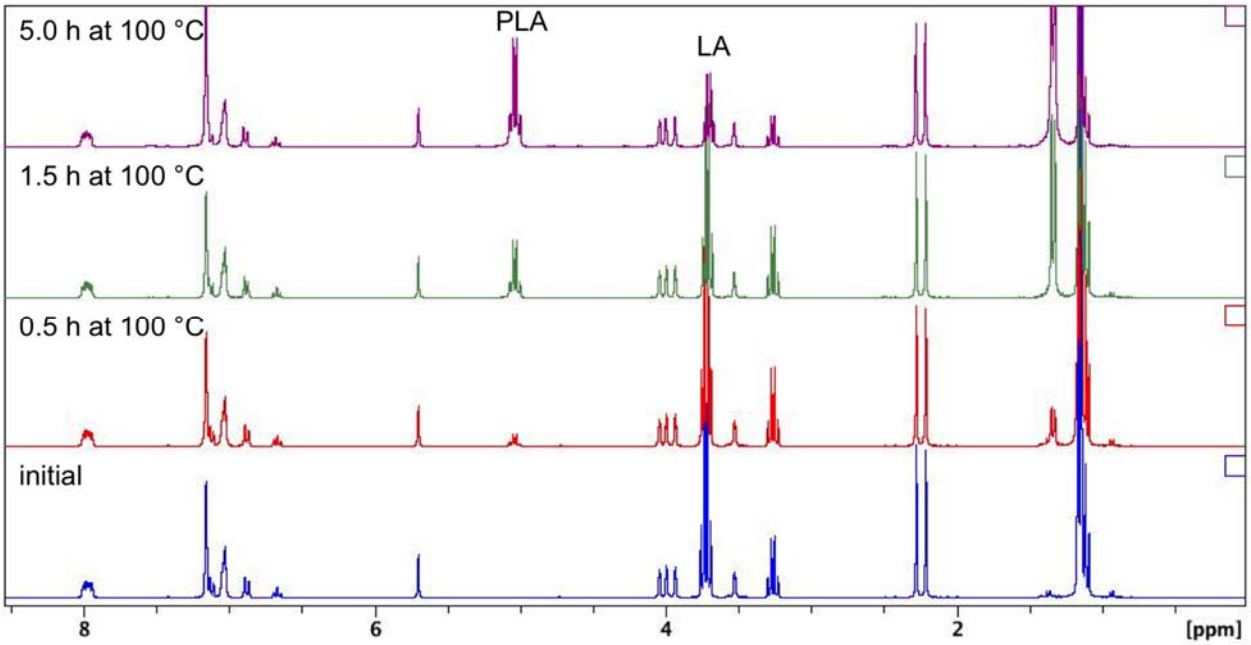

Figure S24. ^{1}H NMR spectra (C_6D_6, 500 MHz, 298 K) of L-lactide polymerization (10 equivalents) in the presence of ($fc^{P,B}$)Zn(OPh); related to Table 1.

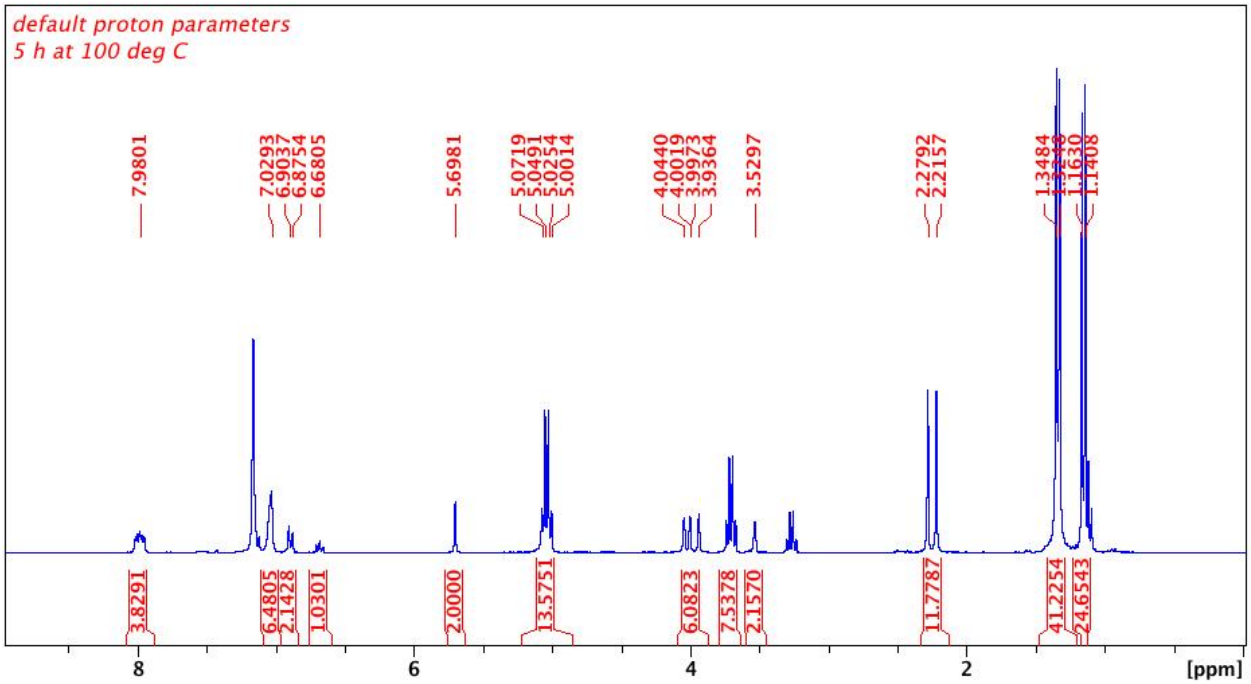

Figure S25. ^{1}H NMR spectrum (C_6D_6, 500 MHz, 298 K) of L-lactide polymerization (10 equivalents) in the presence of ($fc^{P,B}$)Zn(OPh) after 5 h at 100 °C; related to Table 1.

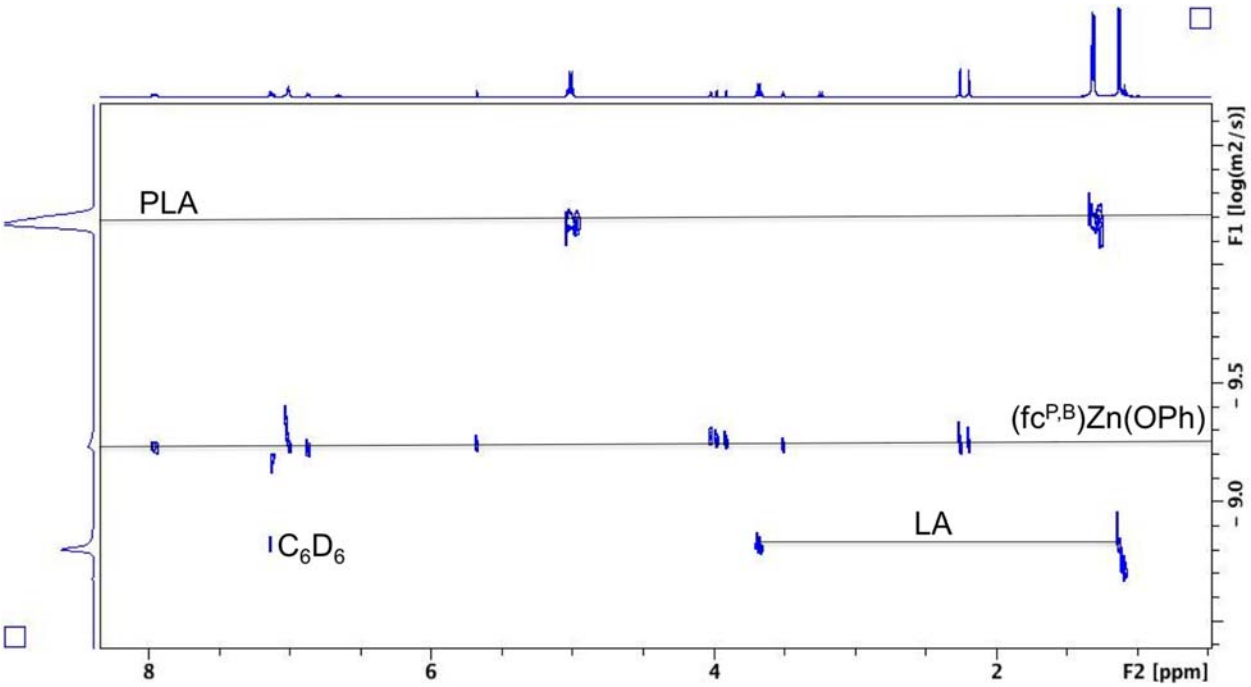

Figure S26. ^{1}H DOSY NMR spectrum (C_6D_6, 500 MHz, 298 K) of L-lactide polymerization (10 equivalents) in the presence of ($fc^{P,B}$)Zn(OPh) after 5 h at 100 °C; related to Table 1.

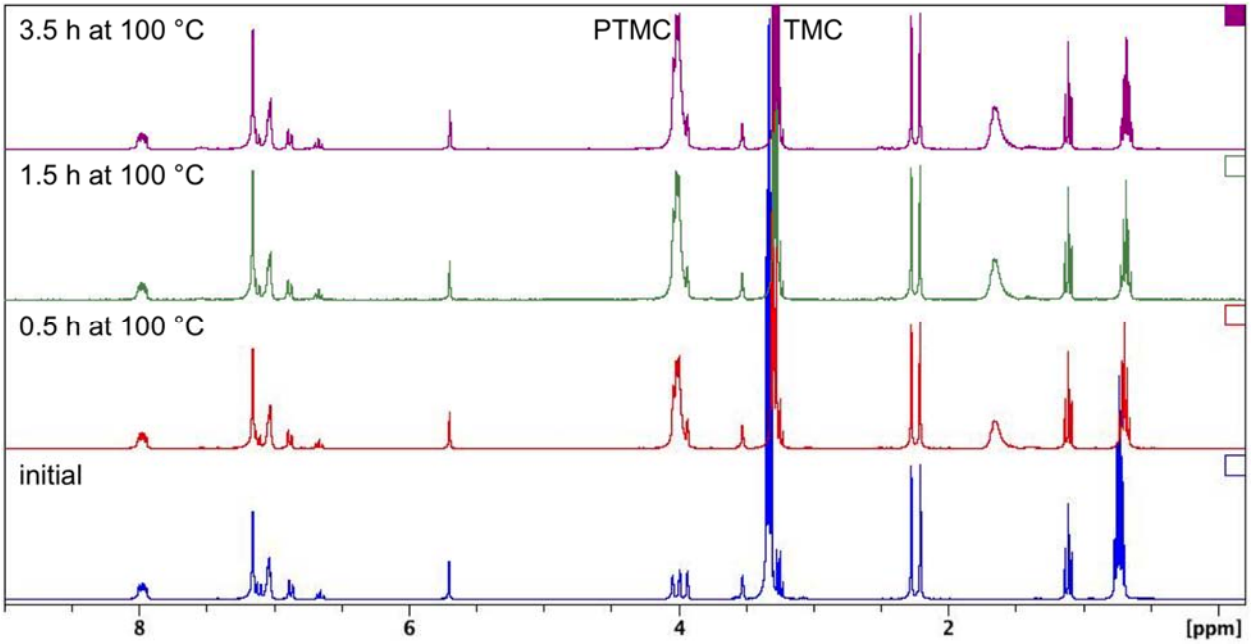

Figure S27. ^{1}H NMR spectra (C_6D_6, 500 MHz, 298 K) of trimethylene carbonate polymerization (13 equivalents) in the presence of ($fc^{P,B}$)Zn(OPh); related to Table 1.

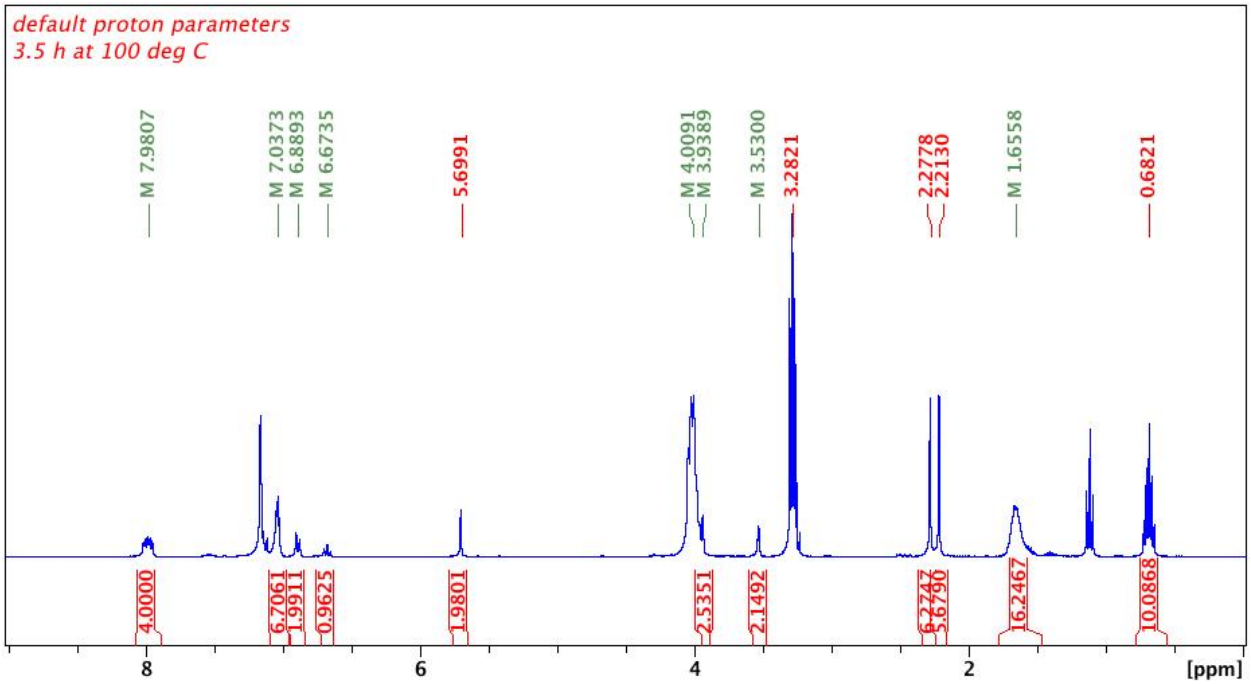

Figure S28. ^{1}H NMR spectrum (C_6D_6, 500 MHz, 298 K) of trimethylene carbonate polymerization (13 equivalents) in the presence of ($fc^{P,B}$)Zn(OPh) after 3.5 h at 100 °C; related to Table 1.

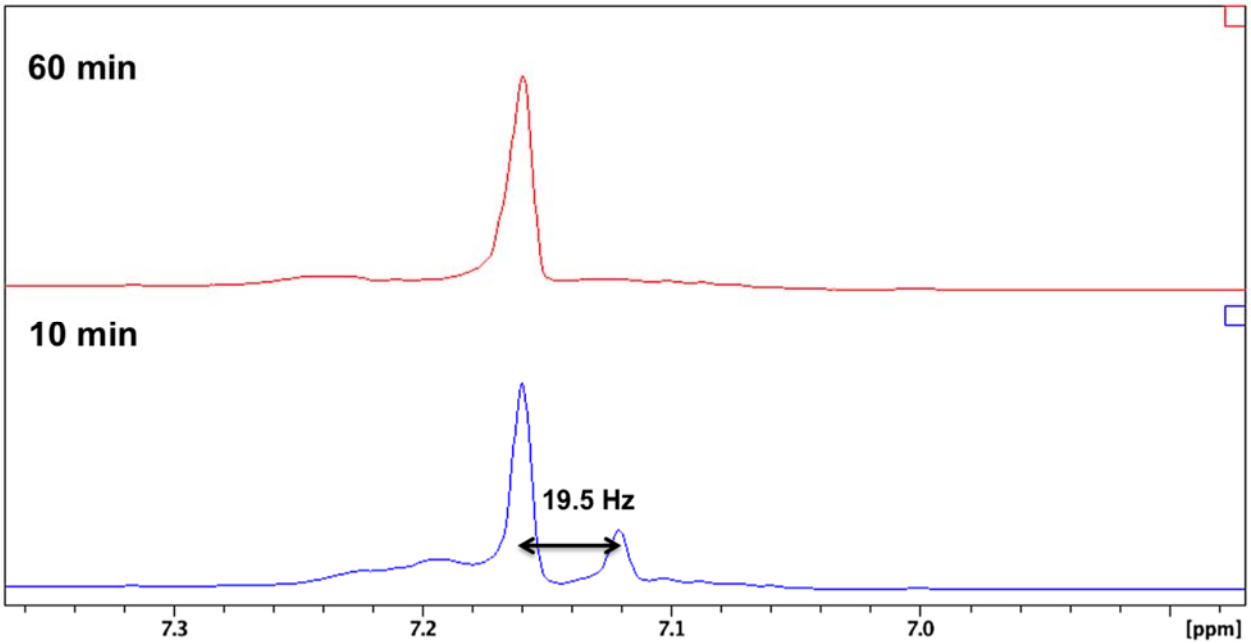

Figure S29. Solution state magnetic susceptibility (C_6D_6, 500 MHz, 298 K) of [($fc^{P,B}$)Zn(μ-OCH_2Ph)]$_2$[BAr^F]$_2$ in the presence of 60 equivalents of trimethylene carbonate. The separation between the solvent peak containing the metal complex and the solvent in the insert is displayed; related to Table 1.

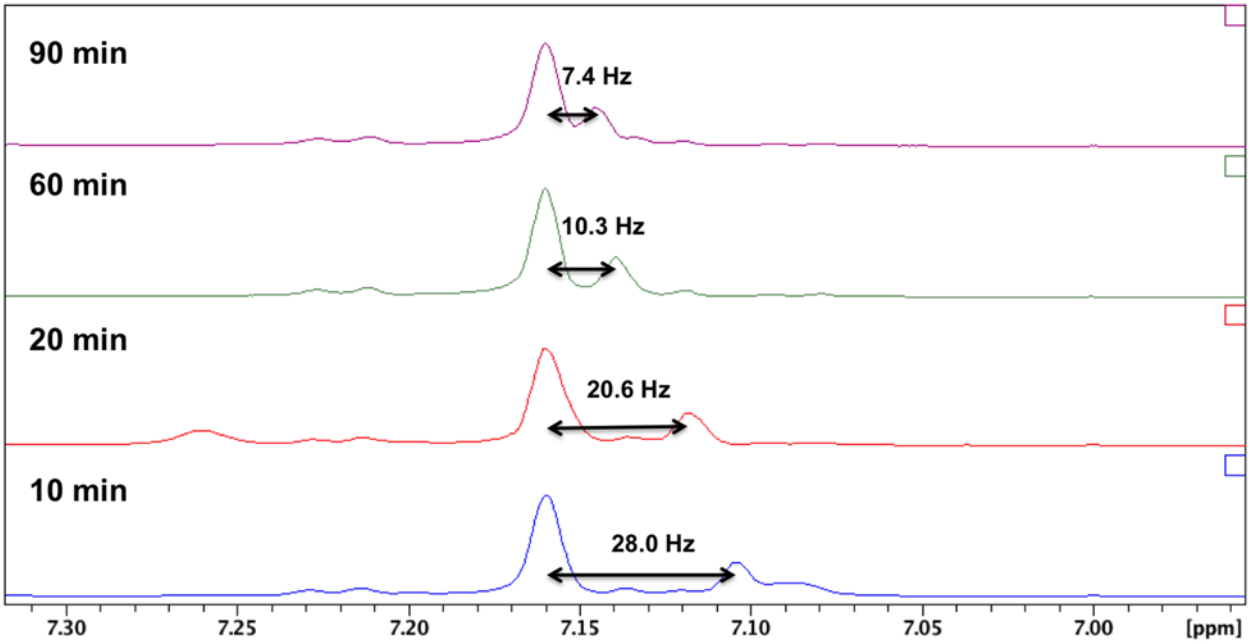

Figure S30. Solution state magnetic susceptibility (C_6D_6, 500 MHz, 298 K) of [(fc^{P,B})Zn(μ-OCH$_2$Ph)]$_2$[BAr^F]$_2$ in the presence of 136 equivalents of δ-valerolactone. The separations between the solvent peak containing the metal complex and the solvent in the insert are displayed; related to Table 1.

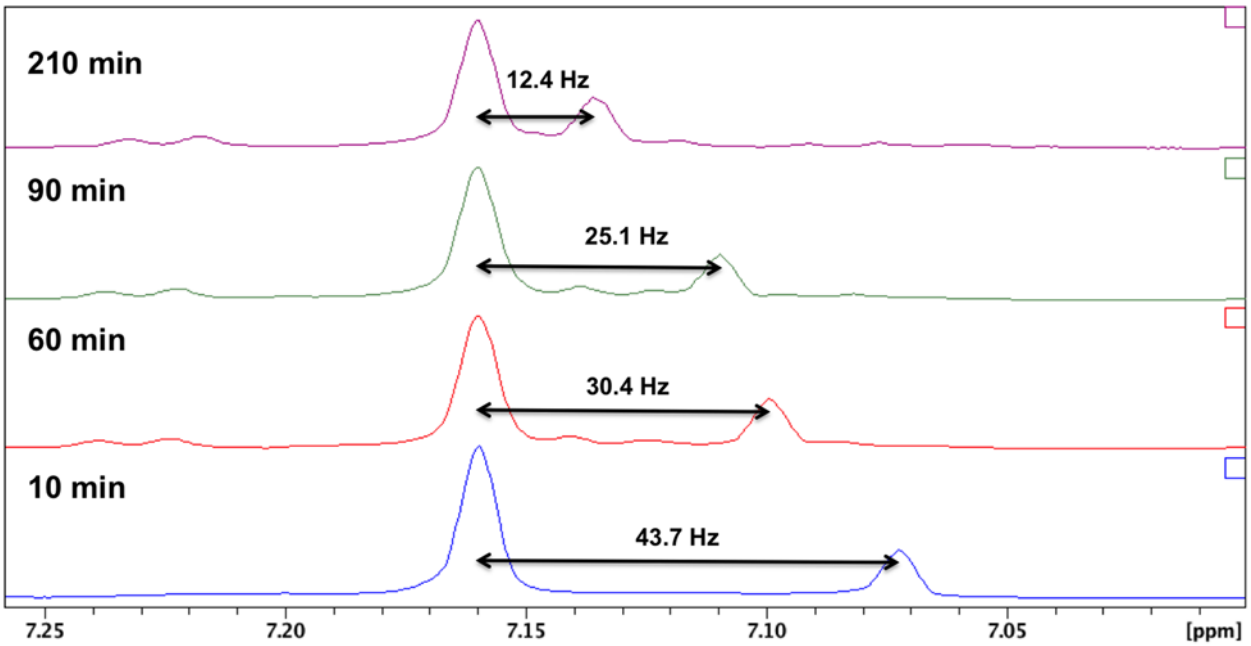

Figure S31. Solution state magnetic susceptibility (C_6D_6, 500 MHz, 298 K) of [(fc^{P,B})Zn(μ-OCH$_2$Ph)]$_2$[BAr^F]$_2$ in the presence of 95 equivalents of ε-caprolactone. The separations between the solvent peak containing the metal complex and the solvent in the insert are displayed; related to Table 1.

Cyclic Voltammetry Data

Calculating i_{pc}/i_{pa}:

$$\frac{i_{pc}}{i_{pa}} = \frac{(i_{pc})_0}{i_{pa}} + 0.485\frac{(i_{sp})_0}{i_{pa}} + 0.086$$

The ratio of the peak currents, i_{pc}/i_{pa}, was determined by the equation above, because the actual baseline for measuring i_{pc} could not be determined in most cases. This was calculated from (a) the uncorrected cathodic peak current, $(i_{pc})_0$, with respect to the zero current baseline and (b) the current at the switching potential $(i_{sp})_0$.

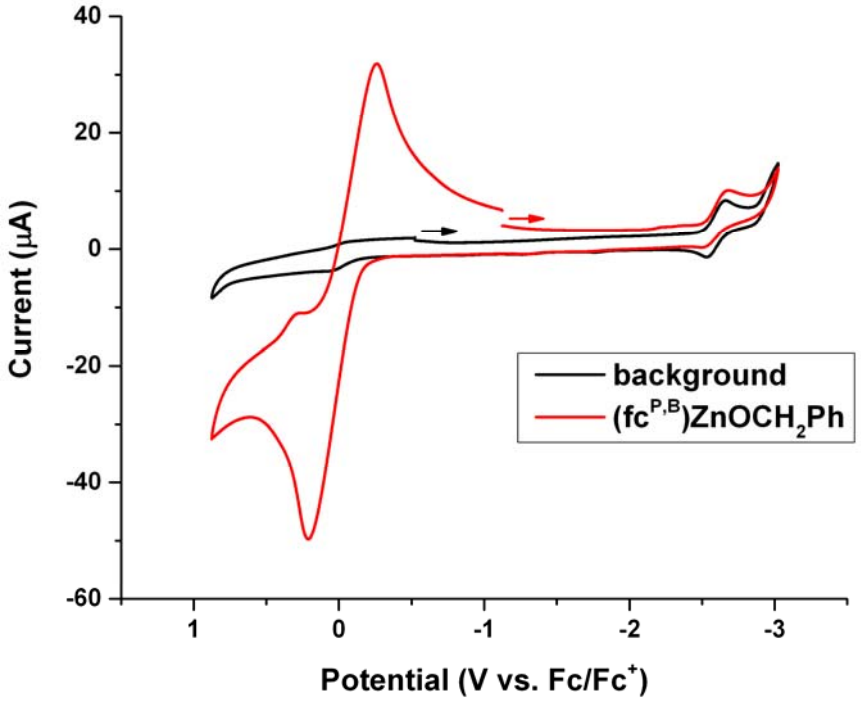

Figure S32. Cyclic voltammograms recorded with a glassy carbon electrode at 100 mV/s in THF, 0.10 M [TBA][PF_6] containing (a) no [($fc^{P,B}$)Zn(μ-OCH_2Ph)]$_2$, (b) 2.5 mM [($fc^{P,B}$)Zn(μ-OCH_2Ph)]$_2$; related to Equation 1.

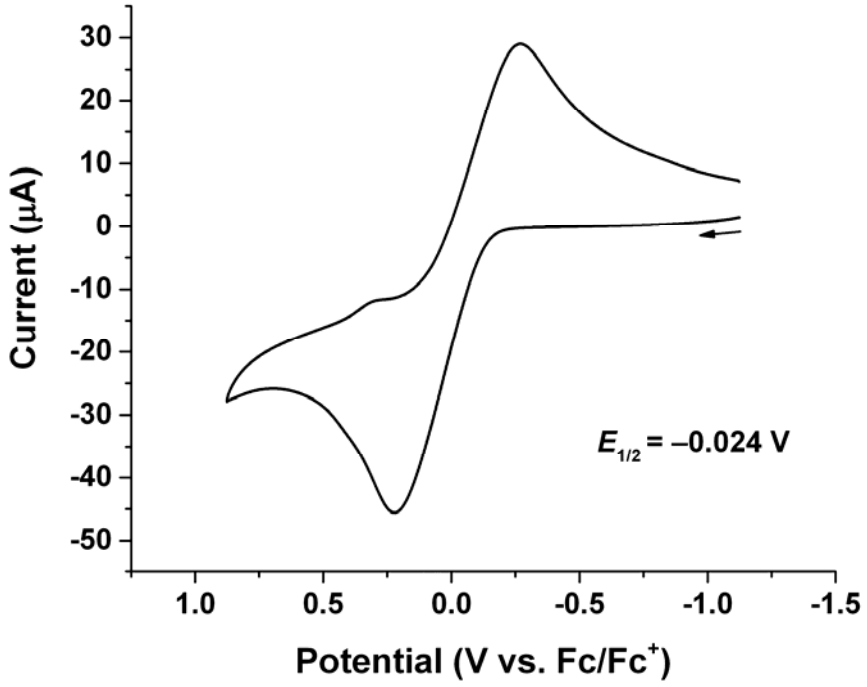

Figure S33. Cyclic voltammogram recorded with a glassy carbon electrode at 100 mV/s in THF, 0.10 M [TBA][PF_6] containing 2.5 mM [($fc^{P,B}$)Zn(μ-OCH_2Ph)]$_2$. $E_{1/2}$ = -0.024 V, i_{pa}/i_{pc} = 1.02; related to Equation 1.

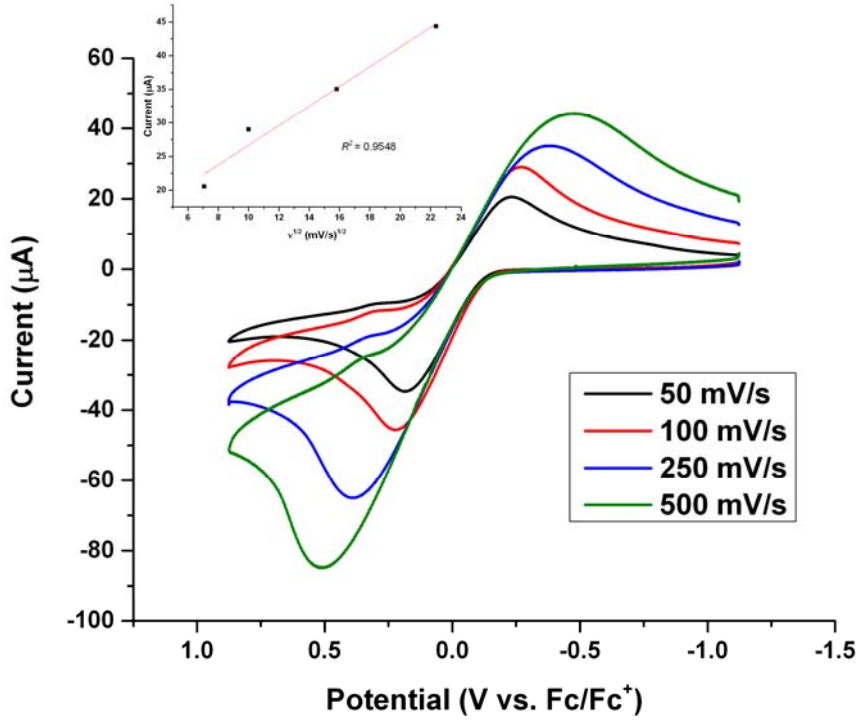

Figure S34. Cyclic voltammograms recorded with a glassy carbon electrode at 50, 100, 250, and 500 mV/s in THF, 0.10 M [TBA][PF_6] containing 2.5 mM [($fc^{P,B}$)Zn(μ-OCH_2Ph)]$_2$; related to Equation 1.

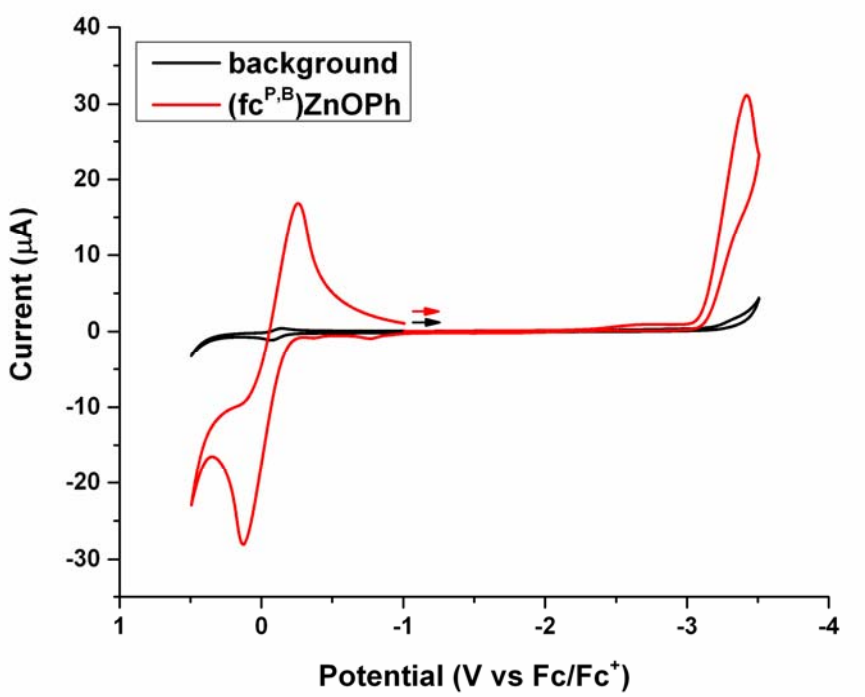

Figure S35. Cyclic voltammograms recorded with a glassy carbon electrode at 100 mV/s in THF, 0.10 M [TBA][PF_6] containing (a) no ($fc^{P,B}$)Zn(OPh), (b) 5.0 mM ($fc^{P,B}$)Zn(OPh); related to Equation 2.

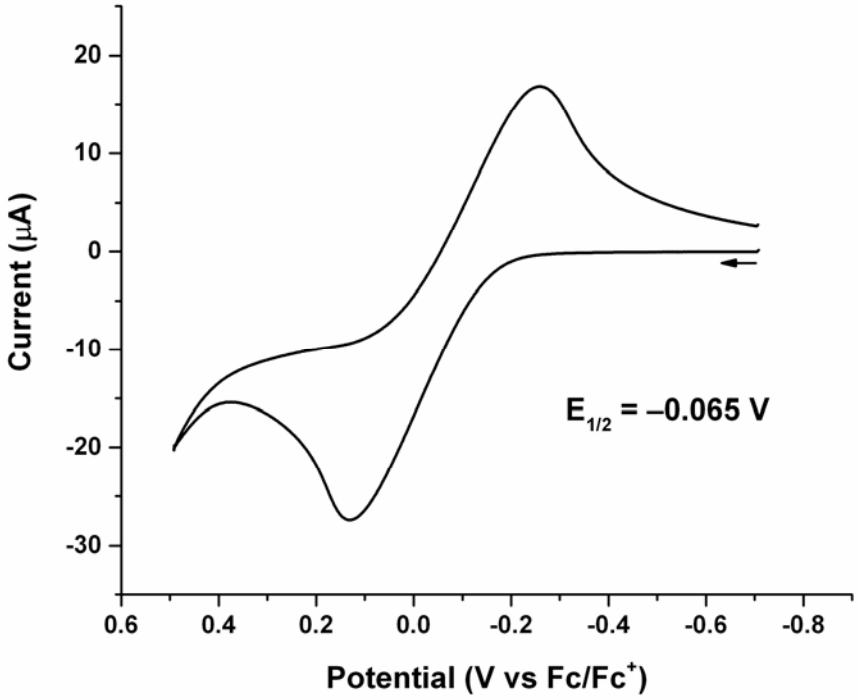

Figure S36. Cyclic voltammogram recorded with a glassy carbon electrode at 100 mV/s in THF, 0.10 M [TBA][PF_6] containing 5.0 mM ($fc^{P,B}$)Zn(OPh). $E_{1/2}$ = -0.065 V, i_{pa}/i_{pc} = 1.06; related to Equation 2.

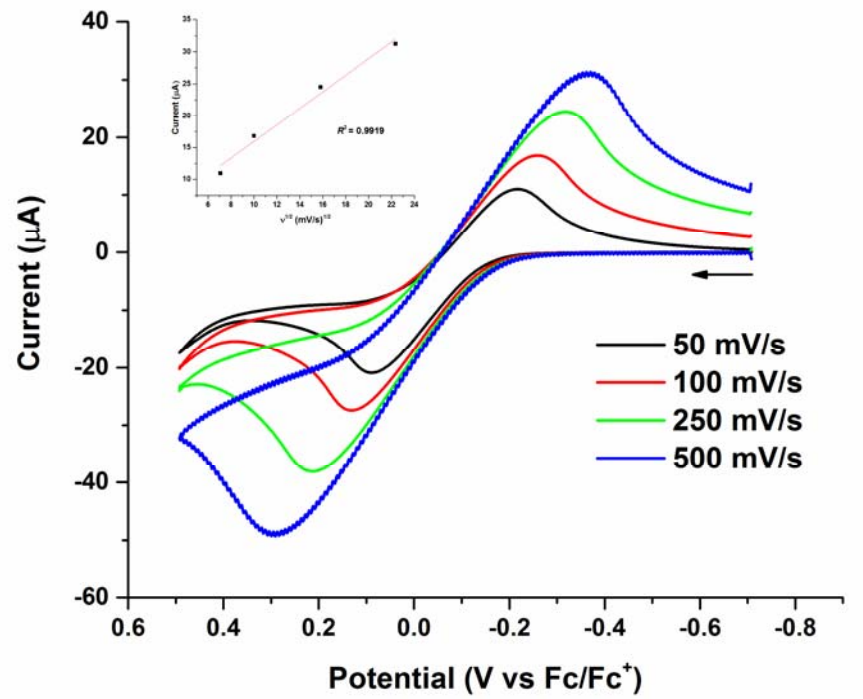

Figure S37. Cyclic voltammograms recorded with a glassy carbon electrode at 50, 100, 250, and 500 mV/s in THF, 0.10 M [TBA][PF_6] containing 5.0 mM ($fc^{P,B}$)Zn(OPh); related to Equation 2.

X-ray Crystallographic Data

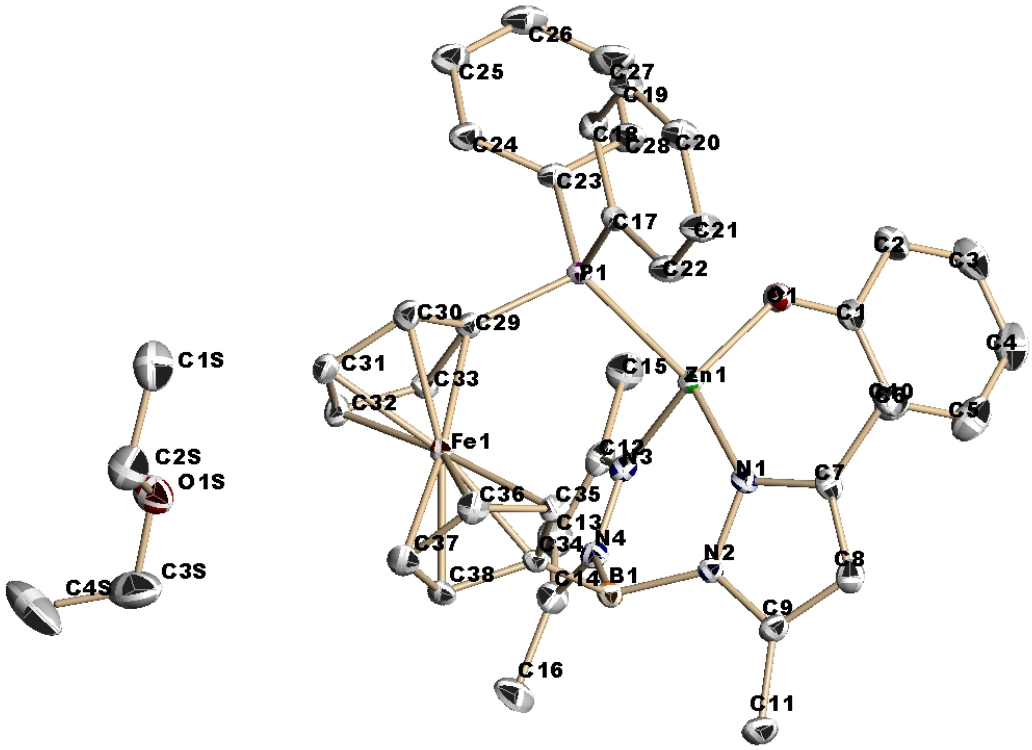

Figure S38. Molecular structure drawing of ($fc^{P,B}$)Zn(OPh) with thermal ellipsoids at 50% probability; hydrogen atoms are omitted for clarity; related to Figure 4.

Crystal data for $C_{42}H_{48}BFeN_4O_2PZn$; $M_r = 803.84$; Monoclinic; space group P21/n; $a = 12.2440(9)$ Å; $b = 14.1412(11)$ Å; $c = 22.6967(17)$ Å; $\alpha = 90°$; $\beta = 94.557(1)°$; $\gamma = 90°$; $V = 3917.4(5)$ Å^3; $Z = 4$; $T = 100(2)$ K; $\lambda = 0.71073$ Å; $\mu = 1.064$ mm^{-1}; $d_{calc} = 1.363$ g·cm^{-3}; 50393 reflections collected; 9606 unique ($R_{int} = 0.0324$); giving $R_1 = 0.0508$, $wR_2 = 0.0924$ for all 9606 data. Residual electron density (e$^-$·Å^{-3}) max/min: 0.63/-0.58.

Size Exclusion Chromatography

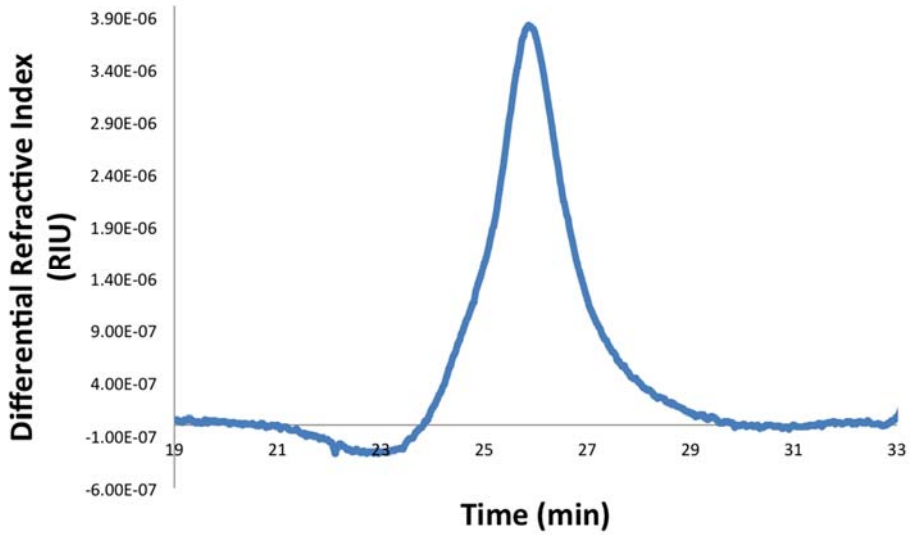

Figure S39. Polymerization of 194 equivalents of L-lactide by compound [(fc^{P,B})Zn(μ-OCH$_2$Ph)]$_2$; M_n = 13,800; $Đ$ = 1.14; related to Table 1, entry 1.

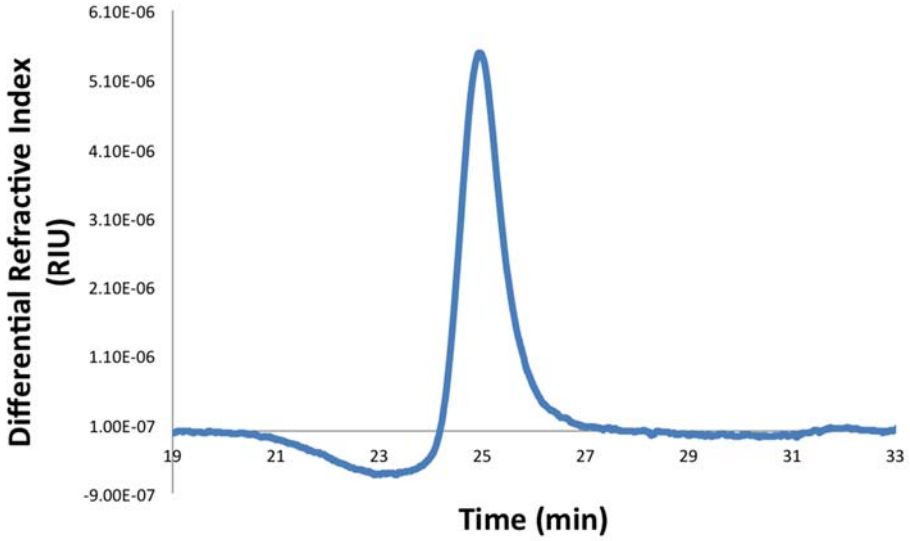

Figure S40. Polymerization of 184 equivalents of L-lactide by compound [(fc^{P,B})Zn(μ-OCH$_2$Ph)]$_2$[BAr^F]$_2$; M_n = 13,500; $Đ$ = 1.03; related to Table 1, entry 2.

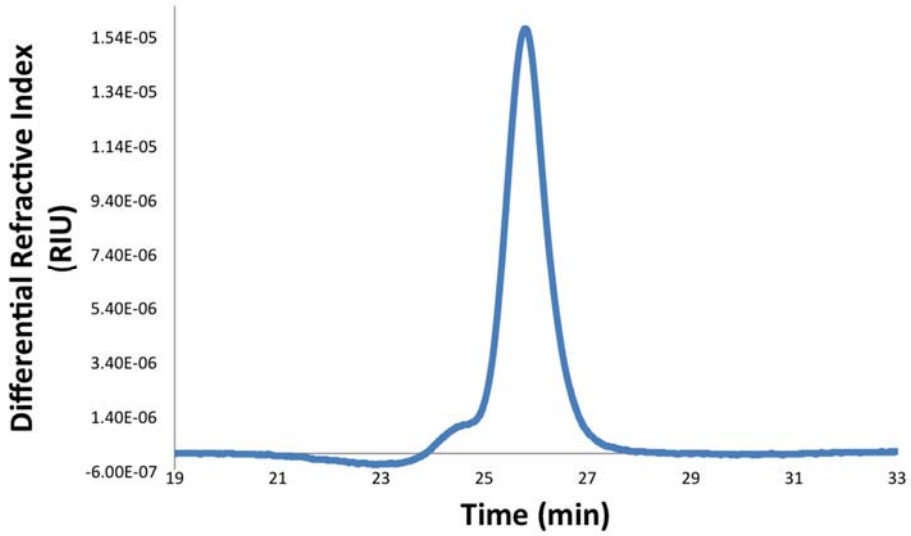

Figure S41. Polymerization of 158 equivalents of ε-caprolactone by compound [(fc^{P,B})Zn(μ-OCH$_2$Ph)]$_2$; M_n = 8,900; $Đ$ = 1.09; related to Table 1, entry 3.

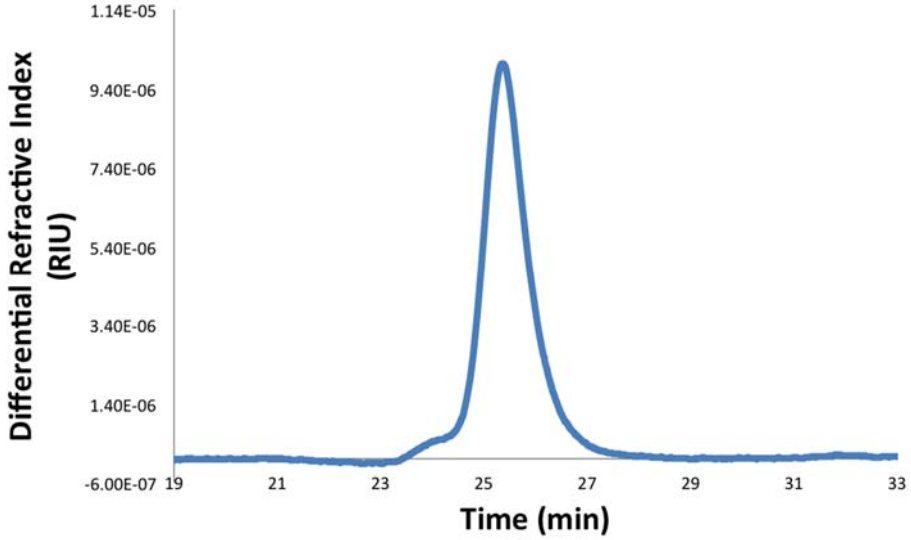

Figure S42. Polymerization of 188 equivalents of ε-caprolactone by compound [(fc^{P,B})Zn(μ-OCH$_2$Ph)]$_2$[BAr^F]$_2$; M_n = 10,500; $Đ$ = 1.08; related to Table 1, entry 4.

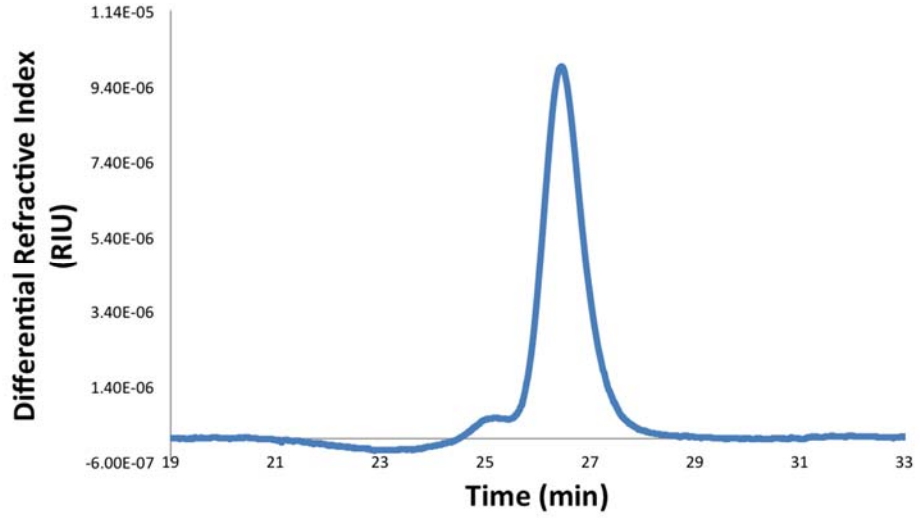

Figure S43. Polymerization of 194 equivalents of trimethylene carbonate by compound $[(fc^{P,B})Zn(\mu\text{-}OCH_2Ph)]_2$; M_n = 10,000; $Đ$ = 1.14; related to Table 1, entry 5.

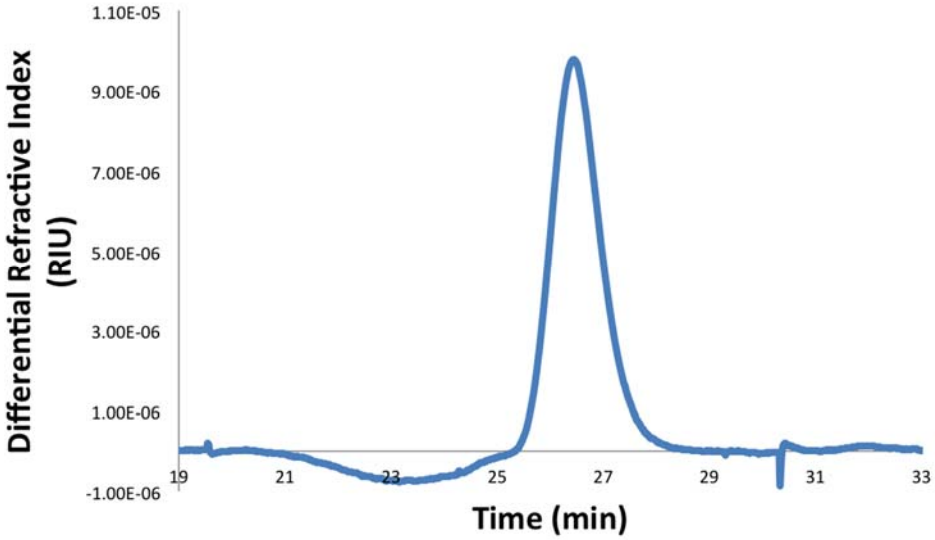

Figure S44. Polymerization of 156 equivalents of trimethylene carbonate by compound $[(fc^{P,B})Zn(\mu\text{-}OCH_2Ph)]_2[BAr^F]_2$; M_n = 8,100; $Đ$ = 1.02; related to Table 1, entry 6.

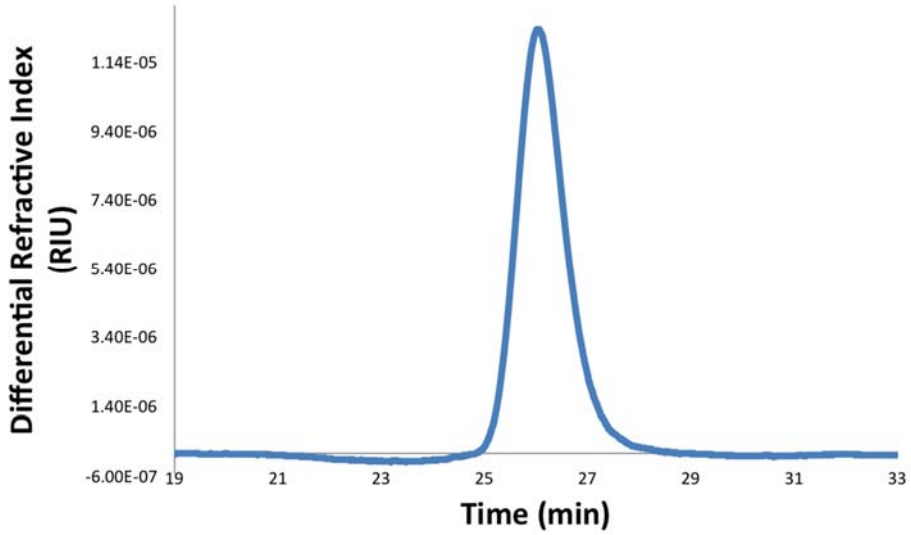

Figure S45. Polymerization of 204 equivalents of δ-valerolactone by compound [(fc^{P,B})Zn(μ-OCH$_2$Ph)]$_2$; M_n = 10,400; $Đ$ = 1.01; related to Table 1, entry 7.

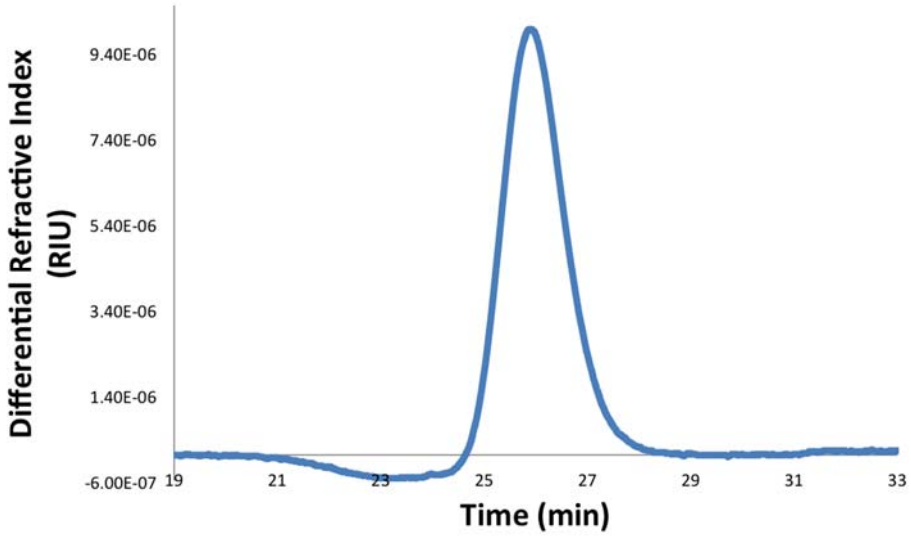

Figure S46. Polymerization of 202 equivalents of δ-valerolactone by compound [(fc^{P,B})Zn(μ-OCH$_2$Ph)]$_2$[BAr^F]$_2$; M_n = 10,500; $Đ$ = 1.04; related to Table 1, entry 8.

Conversion Studies

Table S1. Molar mass versus conversion study of L-lactide in the presence of $[(fc^{P,B})Zn(OCH_2Ph)]_2[BAr^F]_2$; related to Table 1.

Time (min)	Conversion (%)	M_n (NMR)	M_n (SEC)	*Đ*
35	25	10,500	11,800	1.05
55	36	14,300	15,500	1.08
75	43	17,100	18,600	1.06
95	49	19,700	20,900	1.11
115	55	22,600	22,800	1.05

Conditions: benzene as a solvent (1.5 mL) and hexamethylbenzene as an internal standard. The experiment was performed at 70 °C.

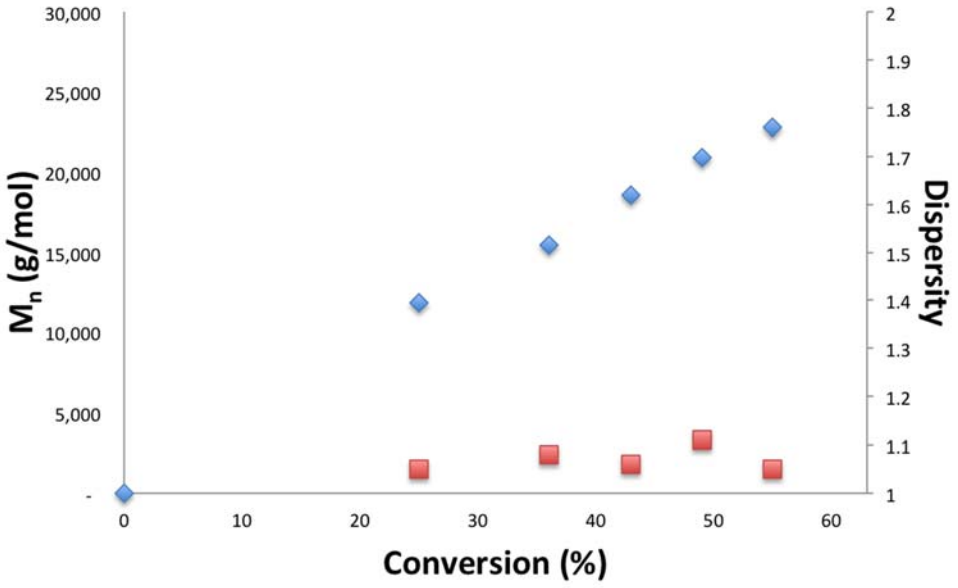

Figure S47. Conversion of L-lactide versus M_n in the presence of $[(fc^{P,B})Zn(OCH_2Ph)]_2[BAr^F]_2$; related to Table 1.

Table S2. Molar mass versus conversion study of trimethylene carbonate in the presence of $[(fc^{P,B})Zn(OCH_2Ph)]_2[BAr^F]_2$; related to Table 1.

Time (min)	Conversion (%)	M_n (NMR)	M_n (SEC)	*Đ*
2	20	3,500	3,100	1.09
3	35	5,900	5,800	1.01
4	41	7,000	7,100	1.02
5	43	7,300	7,600	1.04
6	48	8,200	8,800	1.00
7	68	12,100	12,200	1.02

Conditions: benzene as a solvent (1.5 mL) and hexamethylbenzene as an internal standard. The experiment was performed at ambient temperature.

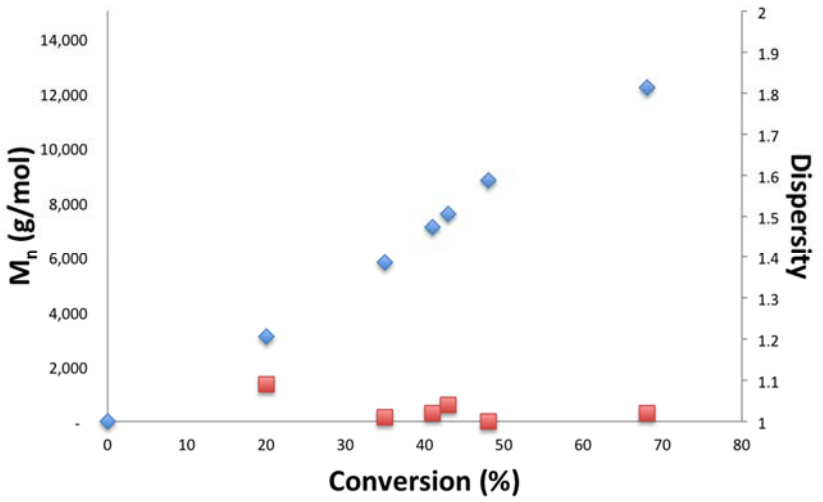

Figure S48. Conversion of trimethylene carbonate versus M_n in the presence of $[(fc^{P,B})Zn(OCH_2Ph)]_2[BAr^F]_2$; related to Table 1.

Table S3. Molar mass versus conversion study of δ-valerolactone in the presence of $[(fc^{P,B})Zn(OCH_2Ph)]_2$; related to Table 1.

Time (min)	Conversion (%)	M_n (NMR)	M_n (SEC)	*Đ*
10	21	6,000	5,800	1.03
15	30	8,000	7,400	1.01
25	48	13,000	11,800	1.04
30	58	15,800	14,100	1.03
35	65	17,900	15,900	1.04
40	71	18,800	16,900	1.04

Conditions: benzene as a solvent (1.5 mL) and hexamethylbenzene as an internal standard. The experiment was performed at ambient temperature.

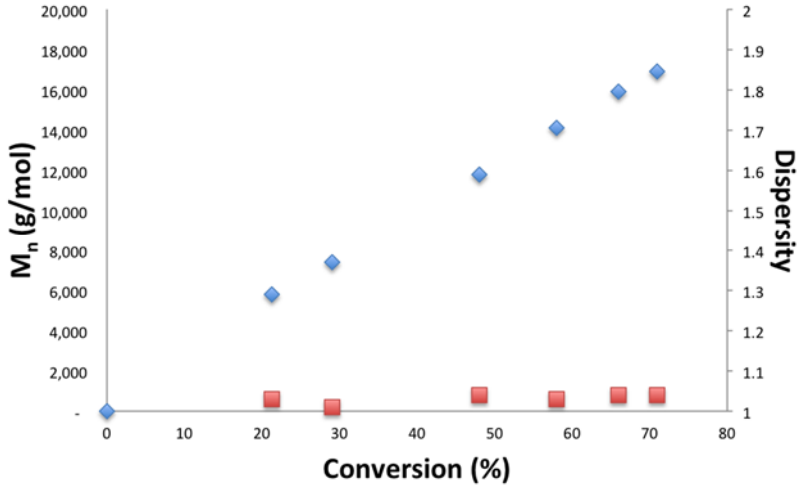

Figure S49. Conversion of δ-valerolactone versus M_n in the presence of $[(fc^{P,B})Zn(OCH_2Ph)]_2$; related to Table 1.

Table S4. Molar mass versus conversion study of δ-valerolactone in the presence of [(fc^{P,B})Zn(OCH$_2$Ph)]$_2$[BAr^F]$_2$; related to Table 1.

Time (min)	Conversion (%)	M_n (NMR)	M_n (SEC)	*Đ*
2	27	8,300	8,900	1.1
4	36	10,900	11,900	1.04
6	40	12,100	13,200	1.04
8	44	13,500	14,700	1.04
10	49	15,000	16,300	1.02
12	56	16,700	17,700	1.03
14	61	17,800	18,500	1.02

Conditions: benzene as a solvent (1.5 mL) and hexamethylbenzene as an internal standard. The experiment was performed at ambient temperature.

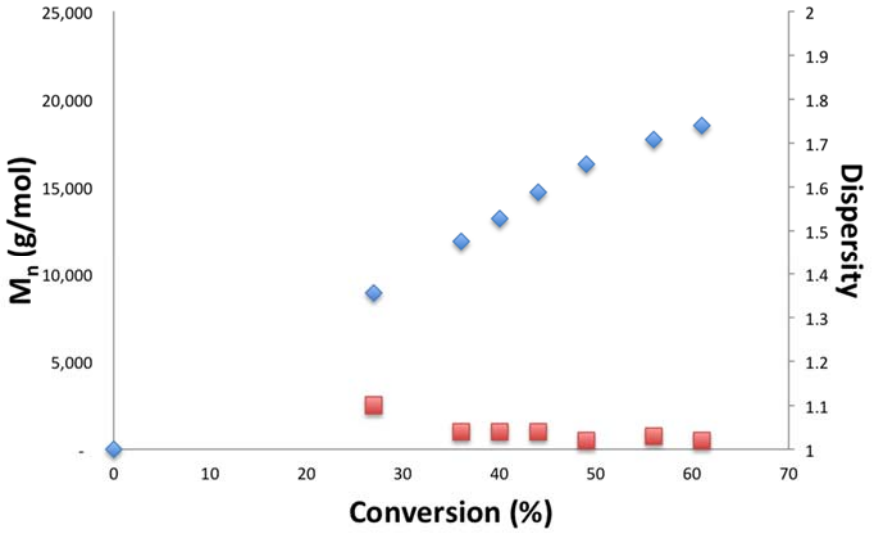

Figure S50. Conversion of δ-valerolactone versus M_n in the presence of [(fc^{P,B})Zn(OCH$_2$Ph)]$_2$[BAr^F]$_2$; related to Table 1.

Table S5. Molar mass versus conversion study of ε-caprolactone in the presence of [(fc^{P,B})Zn(OCH$_2$Ph)]$_2$; related to Table 1.

Time (min)	Conversion (%)	M_n (NMR)	M_n (SEC)	*Đ*
60	15	5,100	5,100	1.01
120	25	8,900	8,300	1.02
180	32	11,300	10,100	1.01
240	43	15,100	14,000	1.01
300	52	18,100	16,400	1.01
360	57	19,800	18,100	1.01

Conditions: benzene as a solvent (1.5 mL) and hexamethylbenzene as an internal standard. The experiment was performed at ambient temperature.

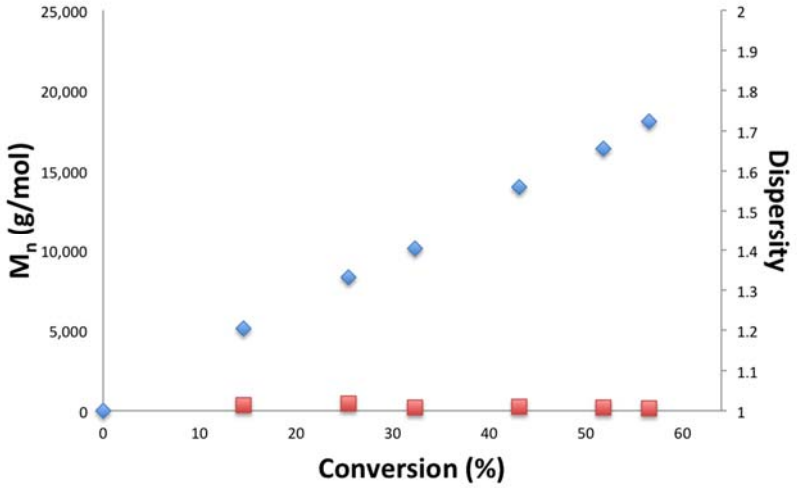

Figure S51. Conversion of ε-caprolactone versus M_n in the presence of $[(fc^{P,B})Zn(OCH_2Ph)]_2$; related to Table 1.

Table S6. Molar mass versus conversion study of ε-caprolactone in the presence of $[(fc^{P,B})Zn(OCH_2Ph)]_2[BAr^F]_2$; related to Table 1.

Time (min)	Conversion (%)	M_n (NMR)	M_n (SEC)	*Đ*
60	17	6,000	5,700	1.06
120	30	10,500	9,300	1.09
180	46	16,100	16,200	1.03
240	57	19,900	20,000	1.04
300	68	23,800	23,800	1.02
360	75	26,200	26,300	1.02

Conditions: benzene as a solvent (1.5 mL) and hexamethylbenzene as an internal standard. The experiment was performed at ambient temperature.

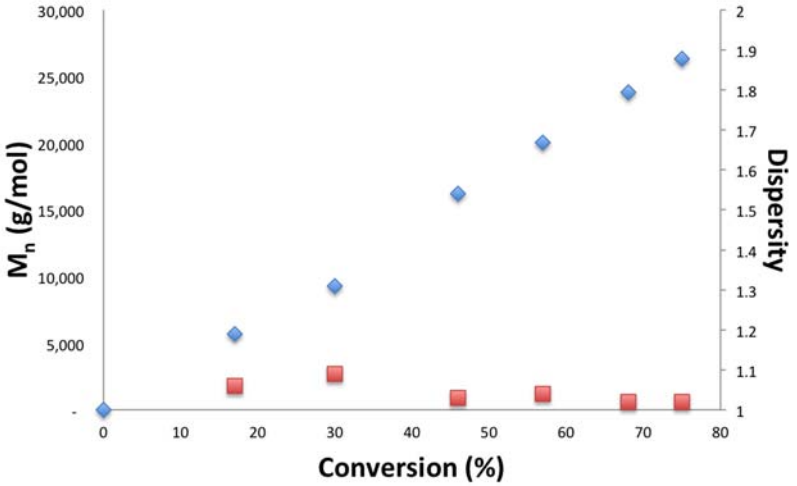

Figure S52. Conversion of ε-caprolactone versus M_n in the presence of $[(fc^{P,B})Zn(OCH_2Ph)]_2[BAr^F]_2$; related to Table 1.

DFT Calculations (Frisch, 2010)

Table S7. **Energies, enthalpies, and free energies of the structures calculated at the PBE1PBE/SDD, 6-311+G(d,p) (PCM, GD3, benzene)//B3LYP/LANL2DZ, 6-31G(d) level;** related to Figures 5-7.

Structures	ΔH	ΔG	G	E with corrections	new G with corrections
Cat-monomer-1	0.43718	0.345	-1587.434324	-1748.702933	-1748.357933
Cat-monomer-2	0.437257	0.344178	-1587.424939	-1748.716437	-1748.372259
After-insertion-LA-dimer	1.031576	0.837546	-3709.203046	-4031.463474	-4030.625928
After-insertion-LA-monomer	0.591316	0.470926	-2121.704113	-2282.701359	-2282.230433
I	0.875768	0.706086	-3174.908168	-3497.482632	-3496.776546
TSI-II	0.989208	0.807349	-3556.520989	-3878.906822	-3878.099473
II	0.99036	0.805784	-3556.557152	-3878.90713	-3878.101346
TSII-III	0.989663	0.808934	-3556.548578	-3878.897142	-3878.088208
III	0.990874	0.803592	-3556.564162	-3878.909919	-3878.106327
IV	0.991638	0.802899	-3556.575983	-3878.920882	-3878.117983
TMC	0.111273	0.074079	-381.634182	-381.4101659	-381.3360869
Lactide	0.151554	0.105907	-534.250539	-533.935059	-533.829152

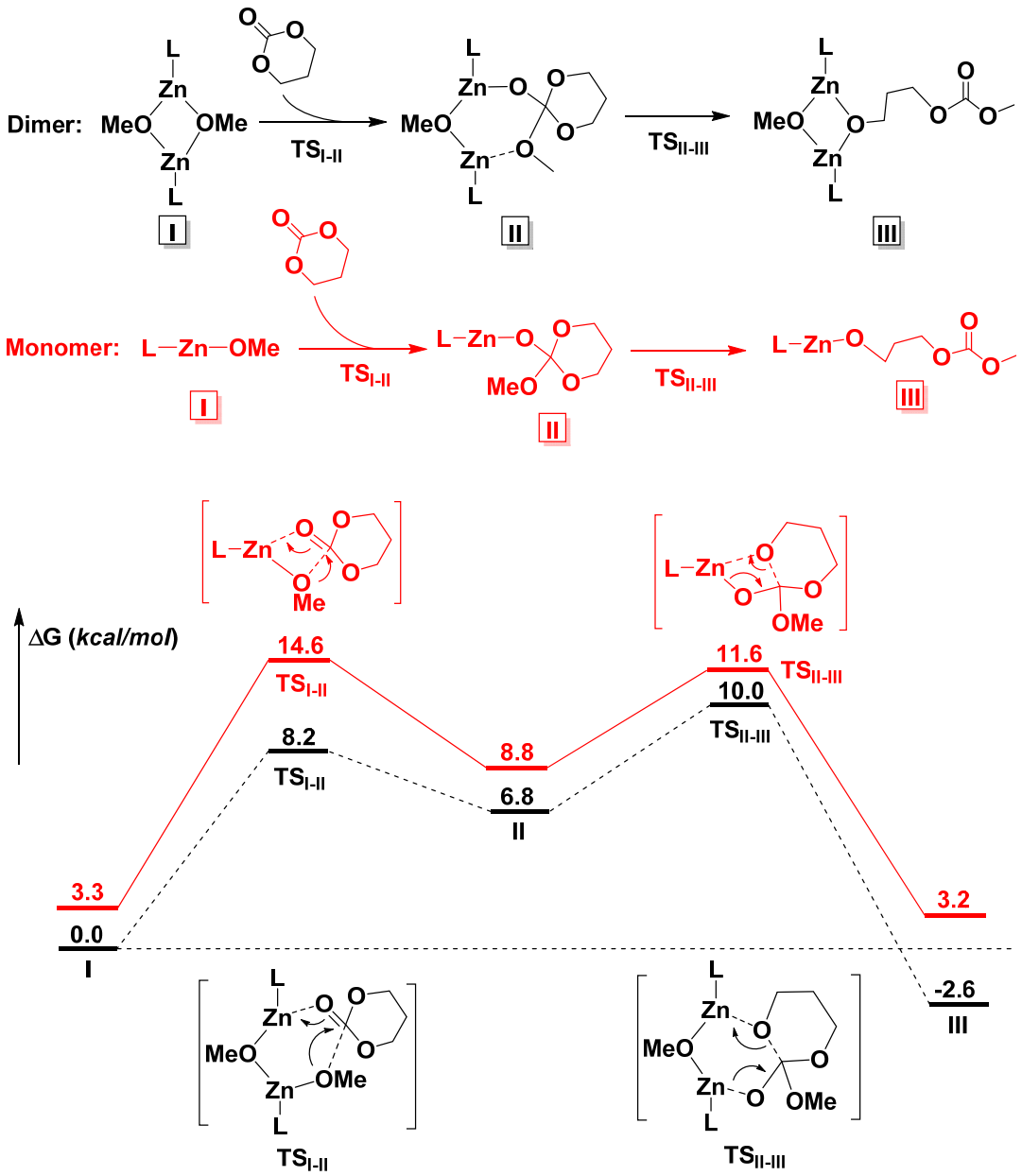

Figure S53. Comparison of the initiation steps of TMC polymerization catalyzed by a monomeric (red) or dimeric (black) form of the zinc complex; figure adapted from (Abubekerov et al., 2018); related to Figure 7.

References

ABUBEKEROV, M. & DIACONESCU, P. L. 2015. Synthesis and Characterization of Ferrocene-Chelating Heteroscorpionate Complexes of Nickel(II) and Zinc(II). *Inorg. Chem.,* 54**,** 1778–1784.

ABUBEKEROV, M., WEI, J., SWARTZ, K. R., XIE, Z., PEI, Q. & DIACONESCU, P. L. 2018. Preparation of multiblock copolymers via step-wise addition of l-lactide and trimethylene carbonate. *Chem. Sci.,* 9**,** 2168-2178.

BECKE, A. D. 1993a. Density-functional thermochemistry. III. The role of exact exchange. *J. Chem. Phys.,* 98**,** 5648-5652.

BECKE, A. D. 1993b. A new mixing of Hartree–Fock and local density-functional theories. *J. Chem. Phys.,* 98**,** 1372-1377.

COCOCCIONI, M. & DE GIRONCOLI, S. 2005. Linear response approach to the calculation of the effective interaction parameters in the $\mathrm{LDA}+\mathrm{U}$ method. *Phys. Rev. B,* 71**,** 035105.

DHAR, D., YEE, G. M., SPAETH, A. D., BOYCE, D. W., ZHANG, H., DERELI, B., CRAMER, C. J. & TOLMAN, W. B. 2016. Perturbing the Copper(III)–Hydroxide Unit through Ligand Structural Variation. *J. Am. Chem. Soc.,* 138**,** 356-368.

DITCHFIELD, R., HEHRE, W. J. & POPLE, J. A. 1971. Self-Consistent Molecular-Orbital Methods. IX. An Extended Gaussian-Type Basis for Molecular-Orbital Studies of Organic Molecules. *J. Chem. Phys.,* 54**,** 724-728.

DOLG, M., WEDIG, U., STOLL, H. & PREUSS, H. 1987. Energy-adjusted abinitio pseudopotentials for the first row transition elements. *J. Chem. Phys.,* 86**,** 866-872.

EHLERS, A. W., BÖHME, M., DAPPRICH, S., GOBBI, A., HÖLLWARTH, A., JONAS, V., KÖHLER, K. F., STEGMANN, R., VELDKAMP, A. & FRENKING, G. 1993. A set of f-polarization functions for pseudo-potential basis sets of the transition metals Sc · Cu, Y · Ag and La · Au. *Chem. Phys. Lett.,* 208**,** 111-114.

FRISCH, M. J. T., G. W.; SCHLEGEL, H. B.; SCUSERIA, G. E.; ROBB, M. A.; CHEESEMAN, J. R.; SCALMANI, G.; BARONE, V.; MENNUCCI, B.; PETERSSON, G. A.; NAKATSUJI, H.; CARICATO, M.; LI, X.; HRATCHIAN, H.P.; IZMAYLOV, A. F.; BLOINO, J.; ZHENG, G.; SONNENBERG, J. L.; HADA, M.; EHARA, M.; TOYOTA, K.; FUKUDA, R.; HASEGAWA, J.; ISHIDA, M.; NAKAJIMA, T.; HONDA, Y.; KITAO, O.; NAKAI, H.; VREVEN, T.; MONTGOMERY, JR., J. A.; PERALTA, J. E.; OGLIARO, F.; BEARPARK, M.; HEYD, J. J.; BROTHERS, E.; KUDIN, K. N.; STAROVEROV, V. N.; KOBAYASHI, R.; NORMAND, J.; RAGHAVACHARI, K.; RENDELL, A.; BURANT, J. C.; IYENGAR, S. S.; TOMASI, J.; COSSI, M.; REGA, N.; MILLAM, N. J.; KLENE, M.; KNOX, J. E.; CROSS, J. B.; BAKKEN, V.; ADAMO, C.; JARAMILLO, J.; GOMPERTS, R.; STRATMANN, R. E.; YAZYEV, O.; AUSTIN, A. J.; CAMMI, R.; POMELLI, C.; OCHTERSKI, J. W.; MARTIN, R. L.; MOROKUMA, K.; ZAKRZEWSKI, V. G.; VOTH, G. A.; SALVADOR, P.; DANNENBERG, J. J.; DAPPRICH, S.; DANIELS, A. D.; FARKAS, Ö.; FORESMAN, J. B.; ORTIZ, J. V.; CIOSLOWSKI, J.; FOX, D. J. 2010. Gaussian 09. Wallingford, CT: Gaussian Inc.

GRIMME, S., ANTONY, J., EHRLICH, S. & KRIEG, H. 2010. A consistent and accurate ab initio parametrization of density functional dispersion correction (DFT-D) for the 94 elements H-Pu. *J. Chem. Phys.,* 132**,** 154104.

HARIHARAN, P. C. & POPLE, J. A. 1973. The influence of polarization functions on molecular orbital hydrogenation energies. *Theor. Chim. Acta,* 28**,** 213-222.

HAY, P. J. & WADT, W. R. 1985. Ab initio effective core potentials for molecular calculations. Potentials for K to Au including the outermost core orbitals. *J. Chem. Phys.,* 82**,** 299-310.

HEHRE, W. J., DITCHFIELD, R. & POPLE, J. A. 1972. Self-Consistent Molecular Orbital Methods. XII. Further Extensions of Gaussian—Type Basis Sets for Use in Molecular Orbital Studies of Organic Molecules. *J. Chem. Phys.,* 56**,** 2257-2261.

LEE, C., YANG, W. & PARR, R. G. 1988. Development of the Colle-Salvetti correlation-energy formula into a functional of the electron density. *Phys. Rev. B,* 37**,** 785.

MATSUO, J., AOKI, K., SANDA, F. & ENDO, T. 1998. Substituent Effect on the Anionic Equilibrium Polymerization of Six-Membered Cyclic Carbonates. *Macromolecules,* 31**,** 4432-4438.

PANGBORN, A. B., GIARDELLO, M. A., GRUBBS, R. H., ROSEN, R. K. & TIMMERS, F. J. 1996. Safe and Convenient Procedure for Solvent Purification. *Organometallics,* 15**,** 1518-1520.

PAOLO, G., STEFANO, B., NICOLA, B., MATTEO, C., ROBERTO, C., CARLO, C., DAVIDE, C., GUIDO, L. C., MATTEO, C., ISMAILA, D., ANDREA DAL, C., STEFANO DE, G., STEFANO, F., GUIDO, F., RALPH, G., UWE, G., CHRISTOS, G., ANTON, K., MICHELE, L., LAYLA, M.-S., NICOLA, M., FRANCESCO, M., RICCARDO, M., STEFANO, P., ALFREDO, P., LORENZO, P., CARLO, S., SANDRO, S., GABRIELE, S., ARI, P. S., ALEXANDER, S., PAOLO, U. & RENATA, M. W. 2009. QUANTUM ESPRESSO: a modular and open-source software project for quantum simulations of materials. *J. Phys. Condens. Matter,* 21**,** 395502.

PERDEW, J. P., BURKE, K. & ERNZERHOF, M. 1996. Generalized Gradient Approximation Made Simple. *Phys. Rev. Lett.,* 77**,** 3865-3868.

ROY, L. E., HAY, P. J. & MARTIN, R. L. 2008. Revised Basis Sets for the LANL Effective Core Potentials. *J. Chem. Theory Comput.,* 4**,** 1029-1031.

SCALMANI, G. & FRISCH, M. J. 2010. Continuous surface charge polarizable continuum models of solvation. I. General formalism. *J. Chem. Phys.,* 132**,** 114110.